Terahertz Time Domain Spectroscopy of Anisotropic Systems: techniques, analysis and applications

TERAHERTZ TIME DOMAIN SPECTROSCOPY OF ANISOTROPIC SYSTEMS: TECHNIQUES, ANALYSIS AND APPLICATIONS

BY

DEREK G. SAHOTA, B.A.Sc.

A THESIS

SUBMITTED TO THE DEPARTMENT OF ENGINEERING PHYSICS

AND THE SCHOOL OF GRADUATE STUDIES

OF MCMASTER UNIVERSITY

IN PARTIAL FULFILMENT OF THE REQUIREMENTS

FOR THE DEGREE OF

MASTER OF APPLIED SCIENCE

Master of Applied Science (2010) McMaster University

(Engineering Physics) Hamilton, Ontario, Canada

TITLE:	Terahertz Time Domain Spectroscopy of Anisotropic Systems: techniques, analysis and applications
AUTHOR:	Derek G. Sahota B.A.Sc. (Engineering Science) Simon Fraser University, Burnaby, Canada
SUPERVISOR:	Dr. Harold Haugen & Dr. John Preston
NUMBER OF PAGES:	xxv, 150

Abstract

The method of terahertz time domain spectroscopy (THz-TDS) allows determination of the broadband electromagnetic response of materials over a typical spectral region of 0.3 to 3 THz. Past work in this field has generally been dominated by the investigation of isotropic materials and the significant potential of using THz-TDS to study anisotropic materials has generally be under utilized. This work encompasses several stages on the path to develop THz-TDS for anisotropic material studies. First, the design, construction and optimization of a high sensitivity THz-TDS polarimetry setup is shown. The extinction ratio between electromagnetic field components in this setup is on the order of 10^5:1, over two orders of magnitude better than the typical 10^3:1 found in previous studies. Birefringent and dichroic polymer and crystalline materials are then studied to show the utility of the polarimetric system when compared to typical THz-TDS systems. To further the goal of developing broadband THz optics, a method for designing and constructing achromatic waveplates is discussed. Using this method, a proof of concept waveplate is fabricated and shown to induce an ellipticity of at least 0.75 over the THz bandwidth of 0.75 to 2.25 THz. Discussion then shifts to the field of gas spectroscopy using THz-TDS, and the THz absorption spectra of water, methanol, ethanol, isopropanol and acetone are measured. The measured water spectrum shows evidence for the formation of a tertramer of water molecules, which has a collective vibrational mode around 2.05 THz. The thesis concludes with a discussion of possibilities for measurements of circular dichroism using THz-TDS.

Acknowledgements

This thesis would not have been possible without the support of numerous people. Within the Photonics Research Lab, Dr. Henry Tiedje provided vital support and wrote numerous software programs that were crucial for completion of this work. Two fellow students working in the THz field, Eugene Hsu and Clare Armstrong also provided inspiration and assistance in numerous endeavours. Other graduate students in the PRL who contributed include Andrew Budz and Travis Crawford, whose detailed notes on the laser systems were very useful. Three undergraduate students also aided in fabrication of the gas cell and new detection electronics: Nick Jewell, Emilia Wilk and Zach Watling. Last, but not least, the assistance and guidance of my two supervisors, Dr. John Preston and Dr. Harold Haugen was indispensible.

Notation and abbreviations

BIMR	Brockhouse Institute for Materials Research
BWO	backward wave oscillator
CW	continuous wave
DFT	discrete Fourier transform
EM	electromagnetic radiation
FIR	far infrared radiation
HDPE	high density polyethylene
IR	infrared radiation
PRL	photonics research laboratory at McMaster University
THz-TDS	terahertz time domain spectroscopy
ZnTe	zinc telluride
α	the power absorption coefficient
c	the speed of light in free space
d	the thickness of a sample
E	the EM field amplitude
f	the repetition rate of a source
$\tilde{H}_m$	the measured transfer function
κ	the imaginary part of the index of refraction
λ	the wavelength of EM radiation
n	the real part of the index of refraction
ϕ	the polarization angle of a femtosecond pulse relative to Φ
Φ	the angle of the (001) axis of crystal
Q	the quality factor of a resonance or signal
θ	the polarization angle of the THz field relative to Φ
ω	the angular frequency of a particular source

Contents

List of Figures

Chapter 1

Introduction

Terahertz time domain spectroscopy (THz-TDS) is a maturing experimental method which allows for broadband analysis of the electromagnetic response of materials in the terahertz range. Radiation in the terahertz range, generally considered as the region of the EM spectrum from a few hundred gigahertz to several terahertz, has free space wavelength in the submillimeter range. Below this region, microwave measurements have generally been used to study materials, and above it regular infrared spectroscopy is widely used (Nuss and Orenstein, 1998). For much of the 20th century a gap existed in between these two experimental methods, due to the issues intrinsic to the generation mechanisms.

In the late 1980's the rise of ultrafast lasers enabled, for the first time, indirect access to generation and detection of radiation in the THz region through the method of THz-TDS. As a brief overview, in THz-TDS a tens to hundreds of femtosecond long optical pulse is used to generate and then detect a picosecond duration electromagnetic field which consists of radiation spanning the THz region. Since the initial development of THz-TDS, the technology has been applied to study a myriad of materials, from paper, plastics and polymers, to semiconductors, metals and superconductors (Koch, 2007; Schmuttenmaer, 2004).

The motivation for studying materials in the THz range goes well beyond

it being an "unexplored territory," there are engineering advantages and fundamental physics which make it advantageous to work in this regime. Many materials absorb weakly in the terahertz range, compared to the visible, so terahertz radiation can be used to image through such materials. One industrial use of THz range radiation has been for imaging through clothing for airport security purposes (Koch, 2007). When investigating conductive materials, THz-TDS provides a non-contact method to measure the DC conductivity and scattering rate of Drude metals independently in a single measurement. The mainstream method for conductivity measurements, a Hall-effect apparatus, requires the placement of electrodes on the materials surface and results in correlated measurements of the DC conductivity and scattering rate (Kamal *et al.*, 2006).

For use with biological samples, terahertz radiation is far lower in energy than x-rays and is non-ionizing, thus it has been investigated for clinical use in dentistry and in detection of various cancers (Koch, 2007). In addition to all these potentially useful measurements, THz-TDS can provide access to picosecond and femtosecond dynamics of materials systems after excitation by another source. Typically, the source used for excitation is an optical pump with femtosecond duration which allows the potential for studies of the dynamics of systems on the femtosecond time-scale.

A key difference between THz-TDS and most spectroscopy techniques is that it offers a measurement of the time domain profile of the electric field amplitude, rather than a measurement of the spectral power or equivalent. The measurement of the electric field allows direct extraction the real and imaginary components of the response through the use of a discrete Fourier transform (DFT). Intensity based frequency domain measurement techniques require that these components be extracted indirectly through the Kramers-Kronig relations. Unfortunately, the Kramers-Kronig relations require the assumption that the measurement has infinite bandwidth, which is physically unattainable and thus additional uncertainty is introduced into the estimates of the complex response.

The span of current THz-TDS experiments has generally been confined to

isotropic materials systems, in other words, systems where the dielectric constants can be described by a single complex scalar. Where anisotropic systems have been studied, the primary method has been to determine the two principal axes by rotating the sample and to then extract the dielectric constant as independent scalars along each axes. While the method of measurement along each principal axis is effective, additional benefit may be possible if a polarimetric approach is taken. In order to conduct polarimetric measurements, the method of THz-TDS must be expanded to allow determination of the electric field vector. In other words, both transverse components of the electric field must be measurable in a reliable and repeatable manner. This thesis focusses on issues related to the development of a polarimetric THz-TDS system and the application of this system to several test cases.

The key interest in developing a polarimetric system came from the possibility of measuring circular dichorism at THz frequencies. Theoretical studies have indicated that biological materials, such as proteins, should have significant circular dichorism in the THz range, but this effect has yet to be verified by any experimental measurements (Xu *et al.*, 2003, 2004). A polarimetric measurement system is one way of quantifying the presence of circular dichorism, as the variation in absorption coefficients of the two circular polarization states results in a net rotation of the electric field vector at any given frequency. Thus the development of a system where the high SNR of THz-TDS is used to give extreme sensitivity to small rotations of the electric field vector is a potential path for detection of this biologically and physically relevant effect.

This thesis begins in Chapter 2 by providing a background overview of the experimental setup required for THz-TDS, the physical principles that allow THz-TDS to be used to study materials, and the methods for extraction of materials parameters from THz-TDS datasets. Chapter 3 contains topics of the utmost important to conducting a repeatable THz-TDS experiment. Due to the pulsed nature of the laser system and the time-domain nature of the measurement, numerous issues are encountered in THz-TDS that are quite different from typical spectroscopy measurements. The creation, alignment and optimization of the polarimetric system for THz-TDS is discussed in detail.

Chapter 3 concludes with a description of a method for using polarimetric THz-TDS measurements to extract the birefringence of a sample.

Chapters 4 through 6 explore several different sets of experiments conducted using the developed THz-TDS polarimetric apparatus. In Chapter 4, birefringence and dichorism in polymer and crystalline systems are explored. In polymer systems, the birefringence can be readily changed through plastic deformation of the material, and several samples are deformed and analysed using THz-TDS. In Chapter 5, the property of birefringence is exploited to develop an achromatic waveplate for THz-TDS applications. This proof-of-concept waveplate performs well and indicates the potential utility of birefringent stacks of materials. Chapter 6 changes course from solid samples to investigate the gas phase. The work in this chapter was part of an phased approach towards detecting circular dichorism at THz frequencies. Several small molecules, including water and the three simplest alcohols are studied for their absorption spectra at varying vapour pressures. One particularly interesting result of these measurements was the potential detection of a collective vibrational mode of the water tetramer.

Chapter 2

Essential THz Background

The field of THz time domain spectroscopy (THz-TDS) has grown significantly since its inception in the late 1980's. This chapter aims to give an overview of the components and technologies which enable THz-TDS. While work to develop new THz sources is ongoing, Ti:sapphire femtosecond lasers are still the heart of the majority of experiments in the THz field. As such, it is prudent to discuss the most relevant aspects of Ti:sapphire pulsed laser systems before delving into the topics of generation and detection of THz radiation.

2.1 Pulsed Laser Systems

The Photonics Research Laboratory (PRL) has several laser systems capable of producing picosecond or shorter pulses. Two commercially produced systems, both from Spectra Physics Inc. are capable of producing non-amplified MHz repetition rate pulses, or kHz range amplified pulses with femtosecond duration. The work in this thesis primarily used the more modern of the systems, which is capable of generating mJ pulses with less than 100 fs duration. This section is only meant to serve as a rough overview of these laser systems and full details can be found in user's manuals for these devices.

A modern Ti:sapphire pulsed laser system actually requires several different laser systems, pulsed and CW, in order to generate femtosecond pulses. The PRL amplified laser system can be considered as being comprised of 4 main

components: the oscillator pump laser (Millennia V), the Ti:sapphire oscillator (Tsunami), the regenerative amplifier pump laser (Evolution X) and the regenerative amplifier (Spitfire). During the latter stages of the work comprising this thesis, the Evolution X pump laser was replaced by a new Empower series pump laser, which has similar characteristics, but is capable of much higher output power.

The Millennia V uses cw diode lasers operating at 809 nm to generate approximately 13 W of light to pump a Nd:YVO_4 crystal via fibre optic cables. The Nd:YVO_4 lases at 1064 nm, and this light is then frequency doubled using a lithium triborate crystal to achieve about 4.3 W of CW output at 532 nm (Spectra-Physics Lasers Inc., 1997).

The green light from the Millennia is then used to pump the Ti:sapphire crystal within the Tsunami oscillator. The Ti:sapphire based system is capable of light amplification over a wide range of wavelengths, from 690 nm to 1080 nm (Spectra-Physics Lasers Inc., 2000). It is well known, from the properties of the Fourier transform, that a wide bandwidth of light is required to get a short pulse (Hirlimann, 2005). In order to get a pulse of light, the various frequencies must have their phases match up correctly and the Tsunami cavity has been designed to ensure this occurs (Hirlimann, 2005). While the laser is capable of spontaneous mode-locking into short-pulsed operation, this process is assisted in the Tsunami by an acousto-optic modulator (Spectra-Physics Lasers Inc., 2000; Ducasse *et al.*, 2005). While the Tsunami should stay mode-locked once pulsed operation has begun, it has been found to be unstable over the very long periods of operation, more than 8-10 hours, which are generally required for THz experiments. As such, the acousto-optic modulator was generally left on for most experiments.

The oscillator has an intrinsic repetition rate of around 80 MHz, which is determined by the properties of the laser cavity (Hirlimann, 2005), and has an output of around 400 mW in 50 fs pulses that are linearly polarized (Spectra-Physics Lasers Inc., 2000). The seed pulse from the oscillator is then routed to the Spitfire regenerative amplifier, where polarization sensitive optics ensure that one pulse is let into the cavity every 1 ms, resulting in the 1 kHz repetition

rate (Spectra-Physics Lasers Inc., 2001). The Evolution X pump laser contains diode lasers which output approximately 60 W of light into a Nd:YLF rod, which lases at 1054 nm. As with the Millennia V, the cavity is frequency doubled resulting in 527 nm output light (Spectra-Physics Lasers Inc., 1999). The cavity is also Q-switched at the same rate as the desired repetition rate of the regenerative amplifier resulting in nanosecond range pulses.

Within the Spitfire system, a grating and large parabolic mirror are used to introduce a significant amount of dispersion by imaging the pulse onto the grating four times (Spectra-Physics Lasers Inc., 2001). The grating effectively stretches the pulse out increasing the path length that shorter wavelengths must travel, so a mismatch between different components occurs (Hirlimann, 2005). The stretched pulse then enters the amplification cavity where a Ti:sapphire crystal has already been pumped by the Evolution X. The pulse makes several hundred passes through the Ti:sapphire crystal, gaining intensity with each pass (Spectra-Physics Lasers Inc., 2001). Over the course of these passes, the pulse is amplified from the nJ range to the mJ range. If the pulse had not been stretched, there would be potential for non-linear interactions within the Ti:sapphire crystal which would distort the pulse. It is also possible that the peak intensity of the pulse would exceed the threshold for causing significant damage to the Ti:sapphire crystal.

Through the use of two Pockels cells, the user selects a pulse to switch out of the regenerative amplifier cavity. This pulse is then routed to a second grating where the dispersion in the opposite direction is introduced (shorter wavelength travel less distance) effectively compressing the pulse in the time domain (Spectra-Physics Lasers Inc., 2001). By adjusting the location of grating-mirror pair, the amount of total dispersion can be optimized to result the shortest possible pulse. This optimization is typically performed by monitoring second harmonic generation in a to determine the position which results in the maximum amount of 400 nm light. During THz experiments, the position would be further optimized to obtain to maximum THz output amplitude.

Due to the degradation of the compressor grating, the output pulse length

of the Spitfire has generally been limited to around 100 fs during the course of this work. The typical output power was 500 mW, resulting in a usable pulse energy of 500 μJ. Recent upgrades to the system have improved this output to 700-800 mW at around 60 fs. More details on these systems can be found within their respective Spectra Physics instructional manuals.

2.1.1 Future Perspectives for Femtosecond Sources

As described above, the current laser systems used in THz-TDS experiments are bulky, costly and have less than desirable stability. In addition to the many various avenues being investigated to design and fabricate CW THz sources, significant potential exists for the use of diode pumped fibre amplified pulsed laser systems instead of Ti:sapphire free space femtosecond lasers.

Utilization of fibre amplified lasers for THz experiments means a significant change in the wavelength of the output pulse, which has a very strong effect on the efficiency of THz generation. Moving to fibre amplifiers means a wavelength shift to at least a 1.05 μm, and potentially up to 1.5 μm. At 1.05 μm THz generation in the most common THz generation crystal, ZnTe, is highly inefficient due to a very small coherence length between the optical and THz pulse (Baker *et al.*, 2003). The use of InGaAs as generation and detection medium has been shown to resolve this coherence length issue (Baker *et al.*, 2003).

Using another electro-optic crystal, gallium phosphide, THz detection and generation has also been shown for a 1.05 μm fibre-amplifier system operating at 120 MHz repetition rate and 10 W average power (Chang *et al.*, 2004). While much work remains to be done in these areas, fibre amplifier sources can be significantly more compact, significantly cheaper, and potentially more reliable than Ti:sapphire systems. It is quite clear that if THz-TDS is ever to be used in the field, the current generation of Ti:sapphire systems must be replaced by a more compact and robust system. Fibre-amplifiers, such as those based on yttrium doping, may be one of the solutions to this problem.

2.2 THz Generation

The original research and development work that lead to modern THz-TDS was conducted primarily at two research groups lead by Dan Grischkowsky at IBM, and David Auston and Martin Nuss at Bell Labs (Schmuttenmaer, 2004). At the time their goal was to generate and detect and study ultrashort (sub-picosecond) transients in electrical transmission lines (Fattinger and Grischkowsky, 1989). The ability to study and characterize these transients was important, as materials advances were pushing electronic devices towards the subpicosecond regime, where the understanding of physical processes is more limited than at lower frequencies (Smith *et al.*, 1988).

The sources developed by these two research groups are generally referred to as Auston switches. These switches are are more appropriately referred to as photoconductive sources, as they rely upon induced photoconductivity in a normally insulating semiconductor to generate THz radiation. THz generation by both optical rectification and photoconductive sources is discussed in the following sections.

2.2.1 Photoconductive Sources

The Auston switch is a remarkably simple, but very effective generator of THz radiation. The switch consists of two electrodes attached to a transmission line whose termination is on a normally insulating piece of semiconducting material. The original materials used to make Auston switches were sapphire for substrates with radiation damaged silicon as the semiconductor and aluminum for the contacts and transmission line (Kübler, 2002). Recent advances have shown that specially grown low-temperature gallium arsenide (LT-GaAs) is superior to silicon for the photoconductive material, and GaAs is becoming far more widespread as a THz generation and detection medium (Bonvalet and Joffre, 2005). Typically the separation between the two transmission lines is on the order of tens of microns. The basic configuration, not to scale, of an Auston switch is shown in figure 2.1.

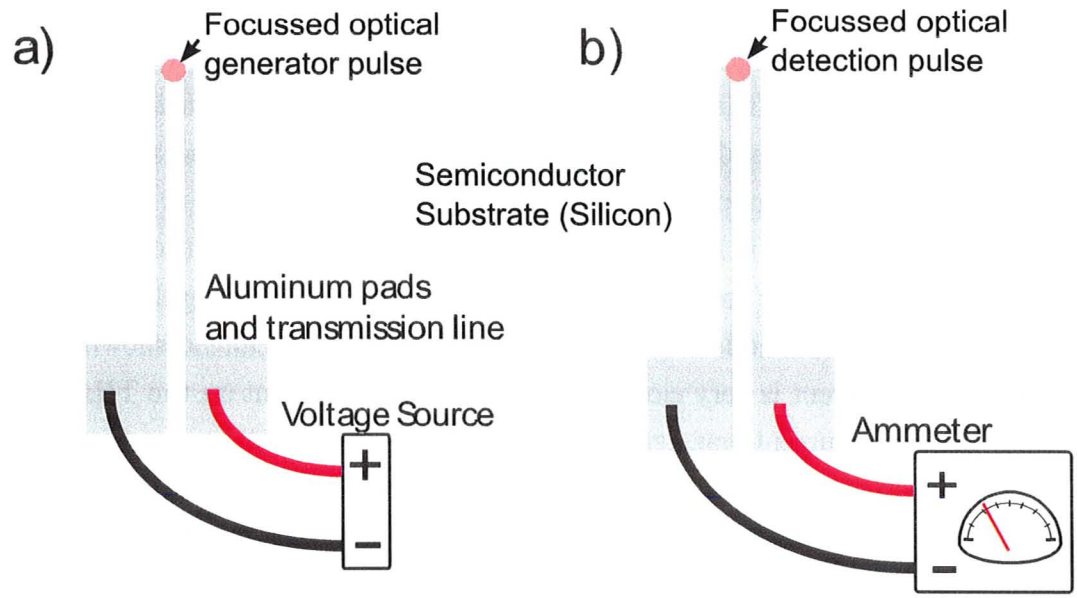

Figure 2.1: The basic setup of Auston switches for a) generation, where an external bias is applied and b) detection, where the current through the switch is measured.

To generate THz radiation, an Auston switch must be biased by an effectively DC voltage (relative to THz frequencies) in the range of tens of volts, creating an effective field on the order of of 5 kV/cm (Smith *et al.*, 1988). The near-IR femtosecond pulse is then aligned and focussed onto the surface of the semiconducting region. The arrival of the pulse, with photons of energy greater than the bandgap, results in generation of a significant amount of photocarriers. These carriers are then swept across the gap between the transmission lines due to the high field, creating a transient current density $\mathbf{J}(t)$ (van Exter and Grischkowsky, 1990).

From Maxwell's equations, it can be shown that the changing current results in a propagating electromagnetic field, $\mathbf{E}(t)$, such that $\mathbf{E}(t) \propto \partial\mathbf{J}(t)/\partial t$ (Griffiths, 1999). This changing field will radiate out into free space with the source semiconductor region almost being like a point source (Bonvalet and Joffre, 2005). In order to more effectively couple the THz radiation into a collimated beam for free space propagation, a hemispherical silicon lens is often attached to the backside of the antenna (Auston, 1993).

While sampling and detection of THz radiation is discussed later, it is prudent to note that an equivalent Auston switch can also be used for coherent detection of the THz field. As shown in figure 2.1b, if another near-IR pulse is focussed onto a second Auston switch along with the THz radiation, then carriers are again created in the semiconducting region (Smith *et al.*, 1988). In this case, the THz field itself accelerates the carriers across the transmission line gap, with the resulting current being measured by a highly sensitive ammeter. Through modelling, and numerical analysis it can be shown that the detected current is very close to being linearly dependent on the THz field when the photocurrent was generated (Duvillaret *et al.*, 2001).

The effectiveness of THz generation with photoconductive sources is highly dependent on the laser parameters as well as the materials parameters of the semiconductor. The most important material parameter is the recombination rate within the semiconductor (Duvillaret *et al.*, 2001). Normal recombination times in silicon and GaAs are on the order of nanoseconds to microseconds, and thus the current in the generator switch would effectively be constant once the carriers were photogenerated (Schmuttenmaer, 2004). However, a very short recombination time is desired in order to create a sharp current change that results in much larger THz field propagating in free space. It is this factor that necessitates the use of very specific semiconductors for THz generation, LT-GaAs and radiation damaged silicon have been specifically tuned to have recombination times that result in significant THz field amplitudes for typical laser setups.

2.2.2 Optical Rectification in Zinc-Blende Crystals

While photoconductive sources drove the initial development of THz-TDS, it is now more common to exploit optical rectification in various nonlinear media to generate freely propagating THz electric fields. A key driver of the movement towards optical rectification is the availability of kHz repetition rate regenerative amplifiers working in the near-IR (Schmuttenmaer, 2004). As described earlier in this chapter, these systems can provide sub 100 fs pulses, at repetition rates of 1 kHz, with pulse energies in the mJ range.

The physical process of creation of THz radiation through optical rectification can be considered through several different avenues. From a purely mathematical perspective, the generation of THz radiation is simply a result of a difference frequency process. Within the ZnTe crystal, there is wave-mixing between electromagnetic fields of different frequencies, which are present because of the short duration optical pulse and mixed due to the non-linear susceptibility.

The result of mixing two waves of frequencies ω_1 and ω_2 are signals at the sum frequency and difference frequency. Within the optical pulse, the significant energy exists over the band of 780 nm to 830 nm. If intermediate wavelengths of 798 nm and 803 nm are considered, these correspond to frequencies of 376.0 THz and 373.6 THz respectively. Thus a mixing process results in a signal at the sum frequency, 749.6 THz (400 nm), and at the difference frequency 2.4 THz (125 μm). A proper treatment of this process would of course consider integrals over the optical pulse and consider the various dispersion effects; however, this simple picture illustrates how such a process can result in THz radiation.

Of all the potential nonlinear crystals that could exploit optical rectification, the most popular for THz applications is ZnTe (Schmuttenmaer, 2004). All crystals with a zinc-blende structure have a non-linear susceptibility tensor with a single non-zero element, which is d_{14} using standard notation (Boyd, 1992). The polarization $\mathbf{P}$ can then be written in terms of the non-linear susceptibility tensor and the incident electric fields $\mathbf{E}$ as:

$$\begin{bmatrix} P_x \\ P_y \\ P_z \end{bmatrix} = \begin{bmatrix} 0 & 0 & 0 & d_{14} & 0 & 0 \\ 0 & 0 & 0 & 0 & d_{14} & 0 \\ 0 & 0 & 0 & 0 & 0 & d_{14} \end{bmatrix} = \begin{bmatrix} E_x^2 \\ E_y^2 \\ E_z^2 \\ 2E_yE_z \\ 2E_xE_z \\ 2E_xE_y \end{bmatrix}. \tag{2.1}$$

The process of obtaining the expected THz response due to the susceptibility relation in eq. 2.1 is simply a geometrical manipulation which is well

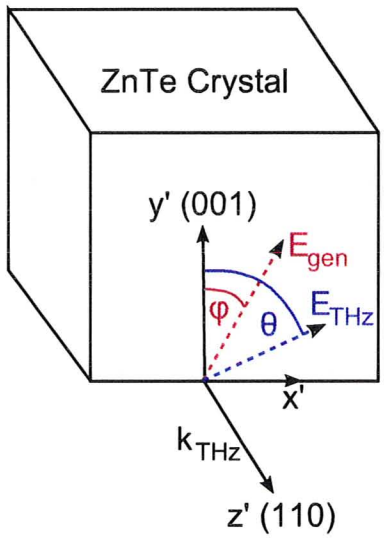

Figure 2.2: Geometry of the electric fields of the optical generator pulse, E_{gen}, and the resulting THz pulse E_{THz}. Optimal THz generation occurs when $\phi = 54.73°$, and the resulting θ is also 54.73°.

documented in several sources (Chen *et al.*, 2001). For brevity the derivation is not repeated here, but using the geometry of figure 2.2 the expected dependence of the THz generation efficiency on the angle, ϕ, between the (001) axis of the ZnTe and the generator pulse is:

$$|\mathbf{E_{THz}}| = d_{14} E_0^2 \left[-3 \left((\sin^2 \theta - \frac{2}{3} \right)^2 + 4/3 \right]^{1/2}. \tag{2.2}$$

A quick analysis of eq. 2.2 shows that the maximum value of $|\mathbf{E_{THz}}|$ is obtained when $\sin^2 \theta = \frac{2}{3}$, or when $\theta \approx 54.73°$. The amplitude of the field at this point is proportional to d_14 and the optical generator beam power:

$$|\mathbf{E_{THzmax}}| \propto \sqrt{\frac{4}{3}} d_{14} E_0^2. \tag{2.3}$$

The other key component to determine is the polarization angle of the THz field, this has been previously determined to be strongly related to the generator polarization angle, ϕ via the relation: (Chen *et al.*, 2001)

$$\theta = \tan^{-1}(2\cot\phi). \tag{2.4}$$

At the angle of maximum THz generation, $\phi = 54.73°$, substitution into eq. 2.4, yields $\theta = 54.73°$. Thus, the optimal generation condition also results in a THz pulse that has an equivalent polarization state to the incident generation polarization state. This behaviour is useful as it means that the absolute polarization state of the THz field can be determined as long as the absolute polarization state of the optical field is known.

Coherence Length in ZnTe

A key consideration in choosing an appropriate ZnTe crystal for generation and detection is the coherence length of the THz and near-IR pulses within the crystal (Bakker *et al.*, 1998). The finite coherence length between the two pulses is the result of the phase matching condition. In literature both phase matching and coherence length are used interchangeably depending on the application. In the generation crystal, coherence is important as the generation efficiency is ultimately limited by the coherence length; beyond the coherence length any generated THz radiation is out of phase with strongest pulse of THz energy and does not contribute significantly to the signal (Nahata *et al.*, 1996). As the absorption coefficient of ZnTe at THz frequencies is non-negligible, being in the range of 5 - 10 cm^{-1} over the region of 1 - 3 THz (Gallot *et al.*, 1999), having a crystal thicker than the coherence length results in significantly reduced THz output.

In the detection crystal, the coherence length plays a role as increase in phase mismatch between the THz and optical pulse results in the sampling of a different point on the time domain profile (Gallot *et al.*, 1999). Thus, as the detector crystal thickness is increased, each acquired THz data point actually represents a weighted average of an increasing time region. Eventually this smearing process will destroy the information contained in the time domain profile and significantly distort the measurement of the THz spectrum (Bakker *et al.*, 1998).

Using previous numerical models of the coherence length (Nahata *et al.*,

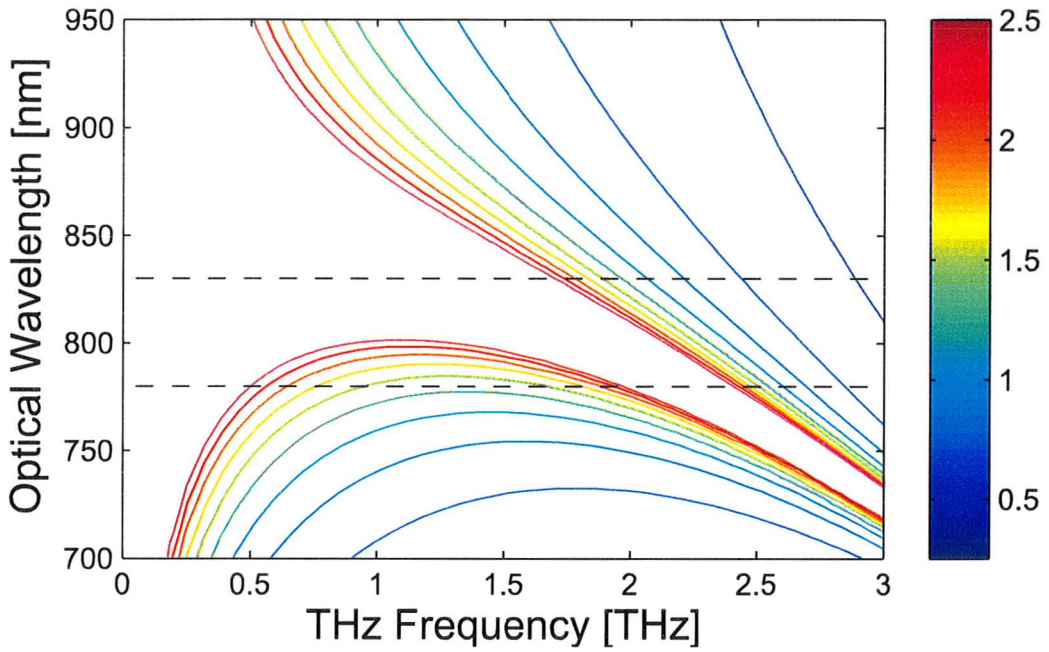

Figure 2.3: The coherence length in ZnTe estimated from the coefficients given in (Nahata *et al.*, 1996). Each contour line represents a change of 250 μm. The horizontal lines denote the limits of the bandwidth of the optical pulse used for THz detection and generation.

1996), figure 2.3 shows the coherence length for the region of interest in a typical THz-TDS apparatus. For wavelengths between 750 and 800 nm, the coherence length is at least 500 μm across the THz bandwidth. However, for longer wavelengths, *e.g.* 830 nm, the coherence length quickly falls off above 2 THz. At 2.5 THz, the coherence length at 830nm is below 500 μm.

This fall-off in coherence length is one of the reasons that limit the measured THz power at frequencies above 2 THz. While strong TO phonon absorption modes at 5.3 THz are often discussed as limiting the bandwidth of THz-TDS experiments, in typical low-frequency experiments (0.3 - 3 THz), the coherence length issues are actually more important (Gallot and Grischkowsky, 1999). The ZnTe crystals used in this thesis were 1.0 mm thick for the generator and 1.3 mm thick for the detector. Full details are available in Appendix A.

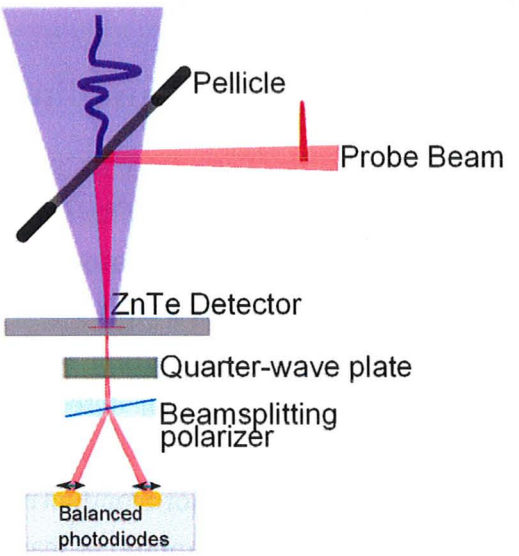

Figure 2.4: Physical layout of a typical electro-optic detection system for THz-TDS. The THz and optical pulses are aligned so their beam waists overlap in space and time within the electro-optic crystal.

2.3 THz Detection

There are three primary methods for detection of THz radiation: bolometric detection, time gated photoconductive antennas and free-space electro-optic sampling (Planken *et al.*, 2001). As the photon energy of 1 THz radiation is only 4 meV, bolometric detection is strongly influenced by thermal noise at room temperature. While cooling with liquid helium and using lock-in amplification can improve the sensitivity of bolometric detection, it is still far inferior to the time domain detection mechanisms.

The detection mechanism for photoconductive antennas was discussed earlier, during the discussion on generation from photoconductive antennas. The typical geometry for THz detection using an electro-optic crystal, see figure 2.4, uses a pellicle beamsplitter to achieve collinearity between an optical pulse and the THz pulse. Both pulses are focussed, the THz with an off-axis paraboloid, and the optical with a long focal length lens, to beam waists within the crystal.

The physical mechanism of electro-optic detection is discussed later, but

first, the mechanism of time domain gating needs to be discussed.

2.3.1 Ultrafast Time Domain Sampling

One of the key advantages of THz-TDS systems is the ability to measure electric fields on a femtosecond time scale. The key enabler of such rapid sampling is the ultrafast pulse, typically generated from a Ti:sapphire laser. Time domain sampling can be implemented with photoconductive or electro-optic detectors in a very similar fashion. From the perspective of gating, the main difference between the two types of detectors is that the ultrafast and THz pulses are typically oriented in the same direction in electro-optic detection, and in opposite directions in photoconductive detection.

In order to implement time domain sampling, at least one optical delay line is required, in either the path leading to the THz beam, or the path leading to the probe beam. Typically, the delay line is placed in the probe beam. The path lengths of the THz setup are initially configured so the optical pulse arrives at the detector slightly before, perhaps by a few to tens of picoseconds, the THz pulse. In figure 2.5 this correspond to t_1. The optical delay line, typically implemented with a retroreflector on a precision motorized stage, can then be translated to increase the optical path length of the probe beam by some amount on the order of tens of microns.

The later time steps t_2-t_6 in figure 2.5 correspond to 60 μm increments in the probe path length which correspond to an increase in delay of 200 fs for each increment. In the case of photoconductive detection, the electronic apparatus detects a current with an amplitude proportional to the THz electric field when the optical probe pulse arrives.

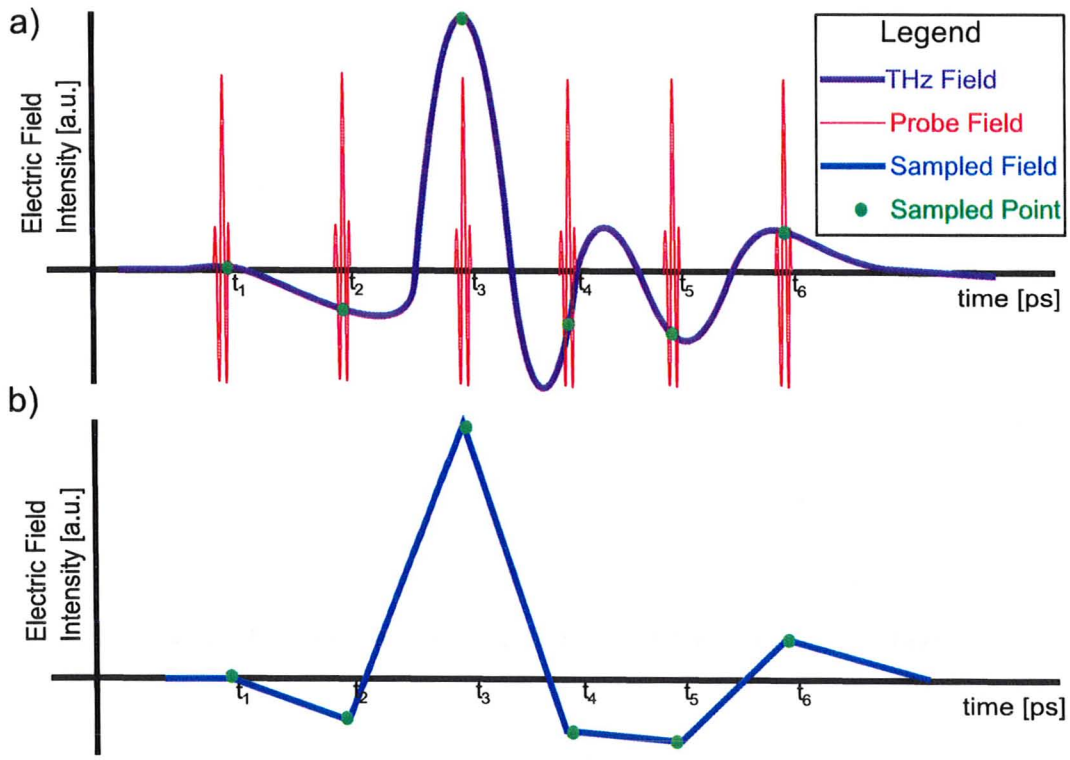

Figure 2.5: Illustration of the time domain nature of the sampling used in free space electro-optic sampling. a) Within the detection crystal, the focussed optical probe pulse overlaps in time with a small region of the THz pulse and the optical delay between the pulses is varied to allow sampling of different regions of the THz pulse. b) Using the 6 time domain points in a), the highly under sampled THz pulse would be recorded as shown.

In order to increase the signal to noise of the apparatus and utilize lock-in detection, the THz generator beam is typically chopped to create an on and off state in the detector electronics. The resulting waveform detected by the electronics is a filtered to obtain primarily the fundamental component of the chopping frequency. The fundamental component is then fed into a lock-in amplifier with the chopper signal as the reference waveform. When the lock-in signal stabilizes, a measurement of the THz electric field at one point in the time domain has been made. Obtaining a complete THz waveform then requires translating the stage through numerous points and measuring the lock-in signal after it has stabilized.

This mechanism of translation and measurement means that each detected THz electric field value in the time domain is really an average over hundreds or thousands of different THz pulses. Each individual time domain measurement is also an average over a different set of THz pulses. This averaging process is very important to understand when considering the limits on noise and systematic errors in THz-TDS measurements.

2.3.2 Electro-optic Detection

The motivation for using electro-optic crystals for THz detection came from the desire to improve on the limited bandwidth and materials processing dependence of photoconductive antennas (Wu and Zhang, 1996). As previously mentioned, the performance of these antennas is highly dependent on the recombination rate of photocarriers within the semiconductor. Over a period of months to years the performance of these antennas tends to decrease (Kübler, 2002). The performance of electro-optic crystals, other the other hand, is only limited by the intrinsic electro-optic coefficients and phonon modes of the material, with processing being a very minor consideration (Gallot and Grischkowsky, 1999; Winnewisser *et al.*, 1997).

Electro-optic detection relies upon the Pockels effect; where the presence of an electric field in a material results in an induced birefringence that is directly proportional to the strength of the electric field (Yariv, 1975). Within a crystal, of length L, that is less thick than the coherence length of the

optical and THz pulse in the material, the THz pulse can be considered to be inducing a constant birefringence when the optical pulse enters the crystal. The material then acts as a waveplate, resulting in a change in the polarization state of the output optical pulse.

The detection apparatus after the electro-optic crystal consists of a quarter waveplate, a beam-splitting polarizer and a pair of photodiodes which are aligned to measure each of the beams off the polarizer independently. The system is initially aligned by rotating the quarter waveplate so the difference of signals received on the two photodiodes is zero. The slight change in the polarization state of the probe field is then detected as the signal between the two photodiodes becomes unbalanced.

The derivation of the dependence of sensitivity electro-optic detection on the relative orientation of the electric field of optical probe and THz field requires a slightly different orientation of the coordinate system. The diagram of figure 2.6 shows the coordinate system (x',y',z') along each crystal axes.

For a zinc-blende crystal, where the only non-zero element is $r_{41} = -4\pi/(\epsilon_0^2 d_{14})$, the index ellipsoid due to an applied electric field $(E_{x'}, E_{y'}, E_{z'})$, is (Yariv, 1975):

$$\frac{x'^2}{n_0^2} + \frac{y'^2}{n_0^2} + \frac{z'^2}{n_0^2} + 2E_{x'}r_{41}y'z' + 2E_{y'}r_{41}x'z' + 2E_{z'}r_{41}x'y' = 1 \qquad (2.5)$$

As with the case of generation in zinc-blende crystals, obtaining the expected change in polarization state requires a geometric transformation by considering the THz electric field from the x-y plane to the (x',y',z') coordinate system. The coordinate system must then be rotated again by an angle, α, to coincide with the principal axes of the index ellipsoid in the y",z" plane (Planken *et al.*, 2001; Chen *et al.*, 2001). From this, the induced birefringence along the index ellipsoid is (Chen *et al.*, 2001):

$$\Delta n = (n_{z''} - n_{y''}) \approx \frac{1}{2} n_0^3 r_{41} |E_{THz}| \sqrt{1 + 3\sin^2 \alpha} \qquad (2.6)$$

From this induced birefringence, the intensity difference measured between

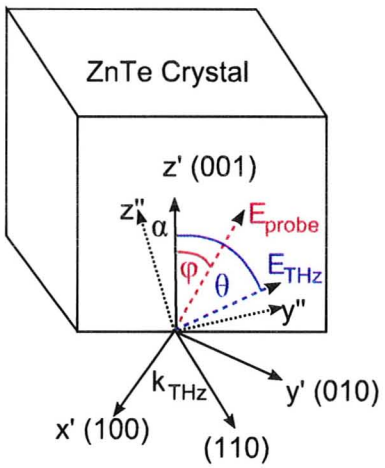

Figure 2.6: Geometry of the electric fields for electro-optic detection in ZnTe. Optimal sensitivity occurs when the THz pulse is polarized orthogonal to the (001) axis of the crystal and the optical probe is polarized parallel or orthogonal to the THz pulse.

the photodiodes can then be readily determined as a function of the angle between the (001) direction of the crystal and the THz and probe electric fields:

$$\Delta I\,(\theta,\phi) \propto \frac{\omega n_0^3 |E_{THz}| r_{41} L}{2c}\,(\cos\theta \sin 2\phi + 2\sin\theta\cos 2\phi) \qquad (2.7)$$

The result of 2.7 is the key result that will be shown in Chapter 3 to enable polarimetric THz-TDS measurements simply by changing the geometry of the detection system.

2.4 Parameter Estimation and Data Analysis

One of the advantages of THz-TDS as an experimental method is that is allows direct determination of the complex dielectric constants of a material across a wide bandwidth. Most spectroscopic techniques only allow determination of the absorption coefficient and rely upon ancillary methods, requiring *a priori* knowledge of either the index of refraction or the use of the Kramers-Kronig relations (Schmuttenmaer, 2004).

As a general method, estimating the materials parameters from THz-TDS transmission experiments requires two measurements; one through a reference and a second through the sample. These time domain measurements can then be converted to the frequency domain by the use of the discrete Fourier transform (DFT). The materials parameters are typically related in some way to the ratio of the DFT of the reference and sample measurements, this ratio is generally referred to as the experimental transfer function, $H_m(\omega)$.

The ability to determine the complex dielectric constants by measuring the electric field in the time domain comes with an important caveat. While literature in the THz-TDS field often expounds on the utility of direct determination versus using the Kramers-Kronig relations, using the DFT also introduces several significant flaws. The most significant of these flaws is a consequence of the finite sampling time and finite sampling duration imposed by experimental constraints. These constraints result in a smearing of the intrinsic complex spectra across several discrete frequency bins in the spectra estimated through the DFT. The combination of these flaws increases the uncertainty of extracted materials parameters and must be considered when comparing THz-TDS to other methods for measuring materials parameters.

The following sections deal primarily with the first order estimate for materials parameters. Numerous groups have developed more complicated estimation methods based on fixed point iteration (Withayachumnankul *et al.*, 2005), estimation of the Fabry-Perot reflection term (Duvillaret *et al.*, 1999), iterative bounded thickness estimation (Dorney *et al.*, 2001), and specialized non-stationary filtering (Pupeza *et al.*, 2007). These more complicated methods are used where necessary throughout the thesis due to the thickness of the sample.

2.4.1 Complex Index of Refraction Estimation

Estimating the frequency complex index of refraction, is particularly useful when studying substrates, polymers, and other materials that are not necessarily transparent in other frequency regimes. In order to derive the appropriate estimation method, it is first assumed that a homogeneous, planar sample

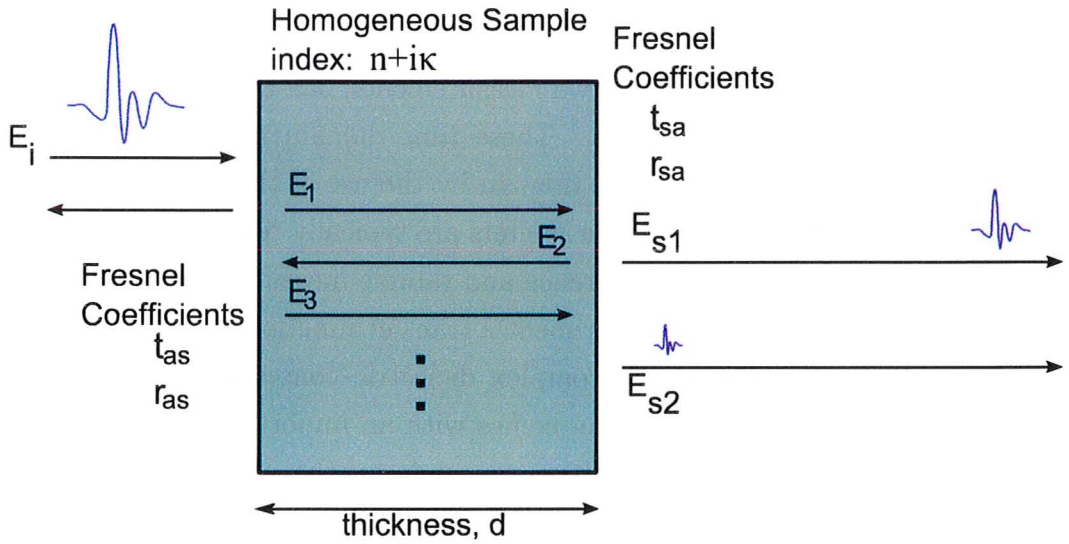

Figure 2.7: Diagram of THz pulse propagation through a homogeneous sample of thickness d. For each of viewing, the pulses are offset vertically each time they reflect from or transmit through an interface.

of thickness d, can be described by an index of refraction $\tilde{n} = n + i\kappa$. The effect of reflections and transmission at each interface of the sample is shown in figure 2.7.

At each interface, where the electromagnetic wave passes from a material with index $\tilde{n}_1$ to a material with index $\tilde{n}_2$ at normal incidence, the portion of the signal that is reflected and transmitted is dependent on the Fresnel reflection and transmission coefficients, which are given by (Griffiths, 1999):

$$t_{12} = \frac{2\tilde{n}_2}{\tilde{n}_2 + \tilde{n}_1}, \tag{2.8}$$

$$r_{12} = \frac{\tilde{n}_2 - \tilde{n}_1}{\tilde{n}_2 + \tilde{n}_1}. \tag{2.9}$$

As the sample is typically in air, further discussion is limited to the case where $\tilde{n}_1 \approx 1$. For the first THz pulse through the sample, that is the pulse that is transmitted at both interfaces and does not undergo reflection, the output electric field, E_{s1}, and the reference electric field, E_{ref} are related to the input electric field E_i by:

$$E_{s1} = t_{as} \exp(i\omega d\tilde{n}_2/c) t_{sa} E_i \quad (2.10)$$

$$E_{ref} = \exp(i\omega d/c) E_i \quad (2.11)$$

The experimental transfer function, H_m can then be determined by taking the ratio of the sample electric field measurement to the reference electric field measurement:

$$H_m(\omega) = t_{as} t_{sa} \exp(i\omega d[n_2 - 1]/c) \exp(-\kappa\omega d/c) \quad (2.12)$$

The result of eq. 2.12 can be used to determine $\tilde{n}_2$ completely, but a transcendental solution does not exist. Instead, $\tilde{n}_2$ must be estimated by an iterative method such as the Newton-Rhapson method. To continue further, assumptions must be made that $\kappa << n$, so the κ term can be safely ignored in both of the Fresnel coefficients. With this assumption, the only contribution to the phase of H_m is the argument of the exponential involving the real part of $\tilde{n}_2$. The index of refraction can then be estimated as:

$$n_2(\omega) \approx 1 + arg[H_m(\omega)] \frac{c}{d\omega}. \quad (2.13)$$

With the index known and continuing to assume that $\kappa << n$, the Fresnel coefficients can then be determined from n_2 and the magnitude taken of eq. 2.12. Recognizing that the absorption coefficient, α, is related to κ by $\alpha = \kappa\omega/(2c)$, the magnitude of H_m is yields:

$$\alpha(\omega) \approx -\frac{2}{d} \ln\left(\frac{|H_m(\omega)|(n_2+1)^2)}{4n_2}\right). \quad (2.14)$$

For thin samples, direct substitution of $n_2(\omega)$ in eq. 2.14 typically results in significant distortion in α due to the Fabry-Perot effect. This distortion can be reduced by either modelling the Fabry-Perot effect on the data, as is done in some of the complicated analysis methods mentioned earlier, or more simply by using the average of n_2 over a ranges of ω, instead of using frequency dependent value.

2.5 Conclusion

The laser systems which enable THz-TDS and the non-linear phenomena that permit generation of THz electric fields using them have led to widespread investigations into the THz spectrum. The theoretical background discussed in this chapter will also need to be buttressed by a significant amount of experimental development, which is discussed in the following chapter.

Chapter 3

THz Experimental Techniques and System Diagnostics

The area of THz time domain spectroscopy first appeared in the early 1990's and has spread from use primarily by physicists (Grischkowsky *et al.*, 1990), to chemists (Schmuttenmaer, 2004), and engineers (Reid and Fedosejevs, 2006). Despite the adoption of THz-TDS within many research settings, rise of a "killer application" within the THz field has yet to occur. The lack of an application where THz-TDS truly shows its superiority over other methods is due to a number of factors, one of the most commonly cited being the difficulty of working with THz-TDS.

As mentioned in Chapter 2, THz-TDS requires the use of femtosecond laser in order to generate and detect the radiation. While the short duration of the laser pulses in these lasers is of particular utility when studying dynamics, the fragility of these laser systems makes industrial uses far more difficult.

Experiments using THz radiation occupy an interesting median between optical and RF measurements. Experimental techniques in both of these regimes are quite advanced, yet in a THz experiment the difficulties encountered in both types of experiments interact. Perhaps the most frustrating aspect of THz experiments is the lack of an accessible direct method to measure a THz signal. These themes influence numerous aspects of experimental optimization and diagnostic techniques for THz-TDS experiments.

This chapter covers a variety of topics of particular interest to any experimentalist working in the THz field. The chapter begins with a discussion of an appropriate noise measurement technique for THz-TDS and the levels of signal to noise that can realistically achieved in a typical THz-TDS setup. The fallacy of the often claimed 100 dB signal to noise ratio is discussed along with some mechanisms to improve signal to noise performance.

The second section of the chapter is dedicated to systematic errors in THz-TDS experiments. Many of these errors were found and minimized or eliminated as part of an attempt to improve the performance of the spectrometer system. Finally the chapter concludes with an overview and in depth mathematical analysis of the method of THz-TDS polarimetry developed in the course of this thesis.

3.1 Appropriate Noise Measurement

Noise in a THz-TDS experiment is far more complicated than a simple additive Gaussian type noise typical of many experiments. The issue of noise is critical for several reasons: thin film experiments the noise model directly affects the uncertainty on parameter estimates, and in absorption spectroscopy experiments the noise model affects the detection limit and detection sensitivity.

Despite the critical importance of a good noise estimate, researchers in the THz field often neglect to do a full analysis of the noise characteristics of their signal. Completing a proper noise estimate is a tedious procedure if the entire signal must be measured a statistically significant number of times, as THz scans often take several minutes to complete. Through years of experience, a shorter method that creates a very good estimate of a complete noise model has been developed and is now used within the Photonics Research Lab at McMaster University. The following section outlines the procedure used evaluate the THz noise model and gives an example of typical measurement.

3.1.1 Method for Noise Characterization

Typically a noise estimate is performed by measuring a zero or constant signal level for an extended period of time. The extended measurement should comprise enough measurements to build a solid statistical model of the noise. In most normal applications, building a noise model on repeated measurements of a time varying signal would be difficult due to problems synchronizing the acquisition system and signal. In a THz-TDS experiment, repeatedly measuring the THz amplitude at a single point is trivial as the delay stage is simply set to a single position and the lock-in value is read for as long as desired.

It should be noted that this method of time-domain noise characterization by measuring at a single delay stage setting results in a slight underestimate of the noise. The effects caused by the translation of the stage and any resulting oscillation in the position of the retro reflector mirrors are neglected in using this type of characterization.

The key observation in developing the noise characterization method was to realize that physical processes in a THz experiment result in three primary classifications of noise:

1. additive noise: completely uncorrelated to the signal amplitude,
2. proportional noise: linearly dependent on the signal amplitude,
3. derivative noise: linearly dependent on the time derivative of the signal amplitude.

Each of the above classes of noise can have systematic and random components, and it is very important to look for both. Systematic errors are most likely to appear when examining the proportional and derivative noise components. A common source of proportional noise is fluctuation in the output power of the laser system. A shift in the relative path length between the THz and probe beam paths, such as a shift caused by thermal expansion, will directly become a source of systematic derivative noise. The following discussion concentrates on random noise sources, with systematic noise to be discussed in a later section.

To estimate the distribution of each of the noise classifications, the most optimal locations to do the noise estimate must be determined. As a quick estimate, three locations for noise measurement can be selected so that at least one of the other components is zero. These optimal locations, shown in figure 3.1.1 are:

1. pre pulse: measured before the THz signal has arrived;
2. pulse peak: measured at the point where the amplitude of the signal is maximal;
3. zero crossing: measured at the point where the time derivative of the signal amplitude is maximal.

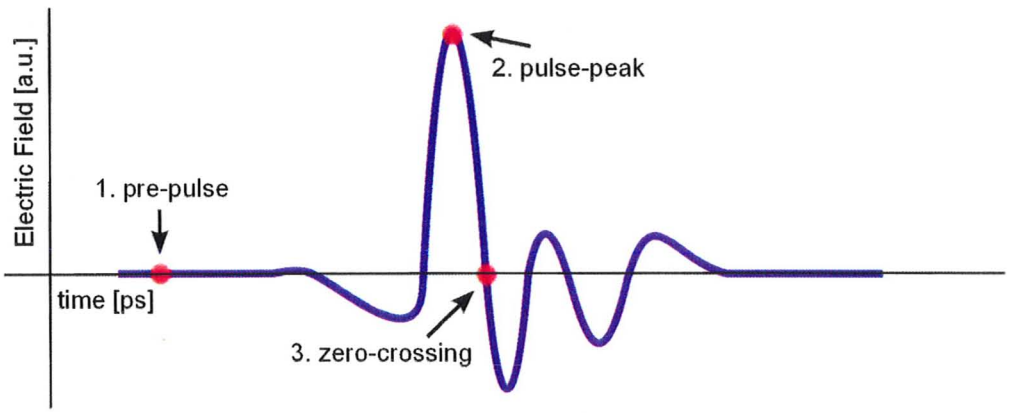

Figure 3.1: The three key locations for characterization of the measurement noise in a THz-TDS system. Monitoring the recorded signal at these optical delay positions allows examination of both systematic and random contributions to the noise.

The pre pulse measurement gives a direct estimate of the additive noise coefficient, which is typically quite small. The random noise at the pulse-peak is comprised of only additive and proportional components, so combined with the pre pulse measurement, it allows determination of the proportional noise coefficient. The final location for measurement is the zero crossing, where the

proportional noise is zero, allowing determination of the derivative component. In practise, the proportional and derivative noise components are orders of magnitude larger than the additive noise, and so the second and third noise measurement locations can be taken as direct estimates of the respective noise coefficients.

This quick method for noise characterization allows both systematic and random components of the noise to be studied with minimal experimental time. The presence of time-variant systematic contributions is detected by moving the THz delay stage to one of the measurement positions and then repeatedly measuring the electric field amplitude for a period of many minutes to hours.

3.1.2 Typical Noise Measurements

When significant changes are made to a THz-TDS setup, or performance problems are noted, it is prudent to use the method of noise measurement to examine the noise characteristics. Figure 3.2a shows a typical noise measurement taken at the THz pulse peak. The photodiode signal was recorded every second for an hour with the optical delay stage locked in place. As the noise contains periodic and random components, a filter was developed to split the noise into these components.

In figure 3.2b, two key systematic fluctuations can be seen. The most obvious component is the fluctuation in amplitude of about 1% with a period of approximately 2 minutes. This fluctuation may be due to short-term fluctuations in the pulse energy of the laser. If figure 3.2b were expanded to include the full hour long measurement, the longer term fluctuation of 1.5% with a period estimated to be 2 hours would also be apparent.

Filtering out the periodic noise also allows an estimate of the level of random fluctuation in the detected THz signal. The standard deviation of the random fluctuation is 0.5%, which translates to a laser power fluctuation of about 0.3%. By comparison, the statistical fluctuation in the pre-pulse measurement is almost 3 orders of magnitude lower than the fluctuation at the peak. Many articles written on THz-TDS technology indicate that signal to noise ratios of 90 dB or higher can be achieved. When measuring this SNR;

however, those articles measure only at the pre-pulse location.

As indicated by these measurements, a much more realistic expectation for the SNR is 50 - 60 dB. Through more precise control of the laser power fluctuations and improved experimental setups, this ratio could be improved. The significant periodic noise measured at the peak should be taken into account when conducting experiments. As THz-TDS measurements typically take several minutes, at least one period of the period fluctuation will occur. In order to reduce the effect of these fluctuations, several measurements can be taken in succession and averaged. Each of these measurements should occur over as short a time frame as possible. It is also important to ensure that the period of the amplitude fluctuation does not correspond to the period of the measurement. If this condition occurs, the influence of the amplitude fluctuation on parameter estimates may be increased rather than being reduced.

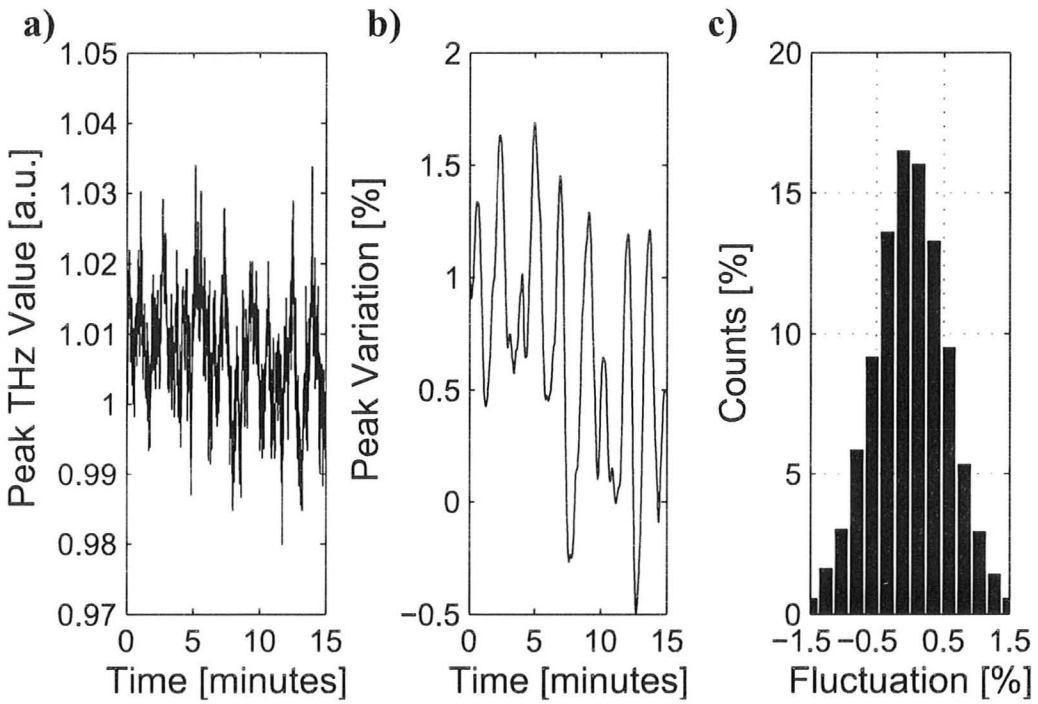

Figure 3.2: Typical noise signals when measured at the THz peak. a) The measurements, taken every 1 second for an hour, show random fluctuations along with periodic noise. b) By filtering the data, periodic fluctuations can been seen. The period of these fluctuations is about 2 minutes with an amplitude of 1%. A longer fluctuation with a period greater than an hour, shows an amplitude drift of about 1.5%, in addition to the shorter variation. c) The random contribution to the noise is obtained by subtracting the periodic components, the standard deviation of this noise is less than 0.5% of the signal peak value.

3.2 Systematic Errors in THz-TDS Systems

Some common systematic contributions to proportional errors are laser power fluctuations and beam drift. In a THz-TDS system using optical rectification for THz generation and electro-optic sampling for THz detection, the detected electric field amplitude is proportional to the laser power to the power of 3/2. Thus even small fluctuations of a few percent in the laser power/pulse energy result in larger variations in the measured THz electric field. It should be noted that a fluctuation in the peak pulse intensity, even without a decrease in average laser power, has an equivalent effect to a change in the laser power.

As a contributor to proportional systematic errors, beam drift primarily plays a role within the detection crystal. The THz beam waist, whose size varies with frequency, must overlap with the much smaller optical probe beam waist within the crystal. Relative drift between the two beam waists causes the optical beam to probe a different region of the THz beam profile. The change in the location of the probe changes the detected THz amplitude and can also lead to significant changes in the detected THz spectrum, especially for the high frequency components.

3.2.1 Path Length Drift

One of the most frustrating aspects of designing and operating a THz-TDS system is the need to maintain the path length of two separate beam paths with micron precision over a typical total path length of metres. This problem is particularly relevant in the gas-cell setup discussed in Chapter 6, as the probe and generation optical beams are split nearly 3 metres before they recombine in the detector crystal. Path length drift is important, as it is the primary source of systematic derivative error in THz-TDS systems.

As mentioned previously, beam drift can result in systematic proportional errors and it can also result in systematic derivative errors. A small change in the approach angle to a mirror of either the probe or generator beam can result in a slight path length variation. While in most optical systems these extraordinarily tiny variations can be neglected, in a THz-TDS system, even a

micron path length variation can result in a very significant systematic error. Beam drift can be introduced by components with adjustable controls, but can also be intrinsic to the laser systems. Drift due components can be minimized by securing those components and minimizing nearby thermal fluctuations and air currents; drift intrinsic to the laser system is very difficult to eliminate.

Thermal fluctuations are problematic for beam drift; however, they are actually more concerning as a direct mechanism for path length drift. Within a research lab, it is common to fabricate custom mounts out of aluminum due to its ease of machining. The thermal expansion coefficient for aluminum is quite large, meaning for a realistic mount with dimensions in the tens of centimeters, a bulk temperature fluctuation of 1° is more than enough to result in noticeable systematic error in the THz signal. The most common use for custom fabricated mounts in THz-TDS systems is actually as a mount for the retro-reflector in the THz delay stage. This location also happens to be the worst possible place for a thermal path length variation to occur as the path length variation is potentially tripled due to physical layout of a retro reflector.

The problem of temperature control is a larger issue than often suspected, due to fluctuations in the local temperature within the research lab. A well-tuned climate control system can pin the average room temperature to a fraction of a degree Celsius; however, the large amount of equipment and air currents around them results in local temperature extrema well outside the deviation in the average temperature. So even if the temperature in a lab is stable to within a fraction of a degree, thermal path length drift must still be considered in THz-TDS systems.

If a custom machined retro-reflector mount is used in the THz-TDS setup, the thermal path length drift can be minimized by machining a second identical retro reflector setup and putting in nearby the first retro reflector, but within the generation beam path. The second retro reflector does not need to be translated, but is there simply to mirror the effect of any temperature fluctuation on my both beam paths.

3.3 Other Experimental Issues

3.3.1 Regenerative Amplifier Repetition Rate Tuning

The de-facto industry standard for repetition rates of Ti:sapphire regenerative amplifiers is 1 kHz; however, many of these systems can also be run at other repetition rates. The effect of changing the repetition rate is something that has not generally been studied within the THz-TDS research community; however, from a theoretical perspective there could be some very significant advantages to tuning the repetition rate.

THz-TDS systems based on photoconductive sources currently have a significant advantage over those based on optical rectification, as they do not require a regenerative amplifier. Thus in photoconductive systems the repetition rate can be as high as the intrinsic repetition rate of the Ti:sapphire oscillator, which is typically designed for around 80 MHz. To achieve lock-in detection, photoconductive systems are often amplitude modulated by an envelope in the region of tens of kHz, but this still an order of magnitude higher than the regenerative amplifier systems.

One of the experimental areas where the repetition rate plays a key role is in lock-in detection. In order to get an accurate measurement from a lock-in amplifier, numerous cycles of the waveform must be acquired and processed. Increasing the repetition rate allows either faster convergence of the acquired value towards the true value, or, if the acquisition window is decreased to keep a constant number of pulses, faster acquisition of the THz waveform.

As the regenerative amplifier system in the Photonics Research Lab is capable of different repetition rates, the possibility of changing from the default 1 kHz was investigated. The results of the investigation are summarized in figure 3.3. As the optical systems within the regenerative amplifier and pump laser have been designed with 1 kHz in mind, the efficiency of the amplifier is clearly reduced as the repetition rate is increased. When considering the effect the THz generation system, it becomes apparent that the optimal signal to noise is actually achieved at a repetition rate around 1.4 kHz, despite the much lower THz power. This improved signal to noise is potentially useful

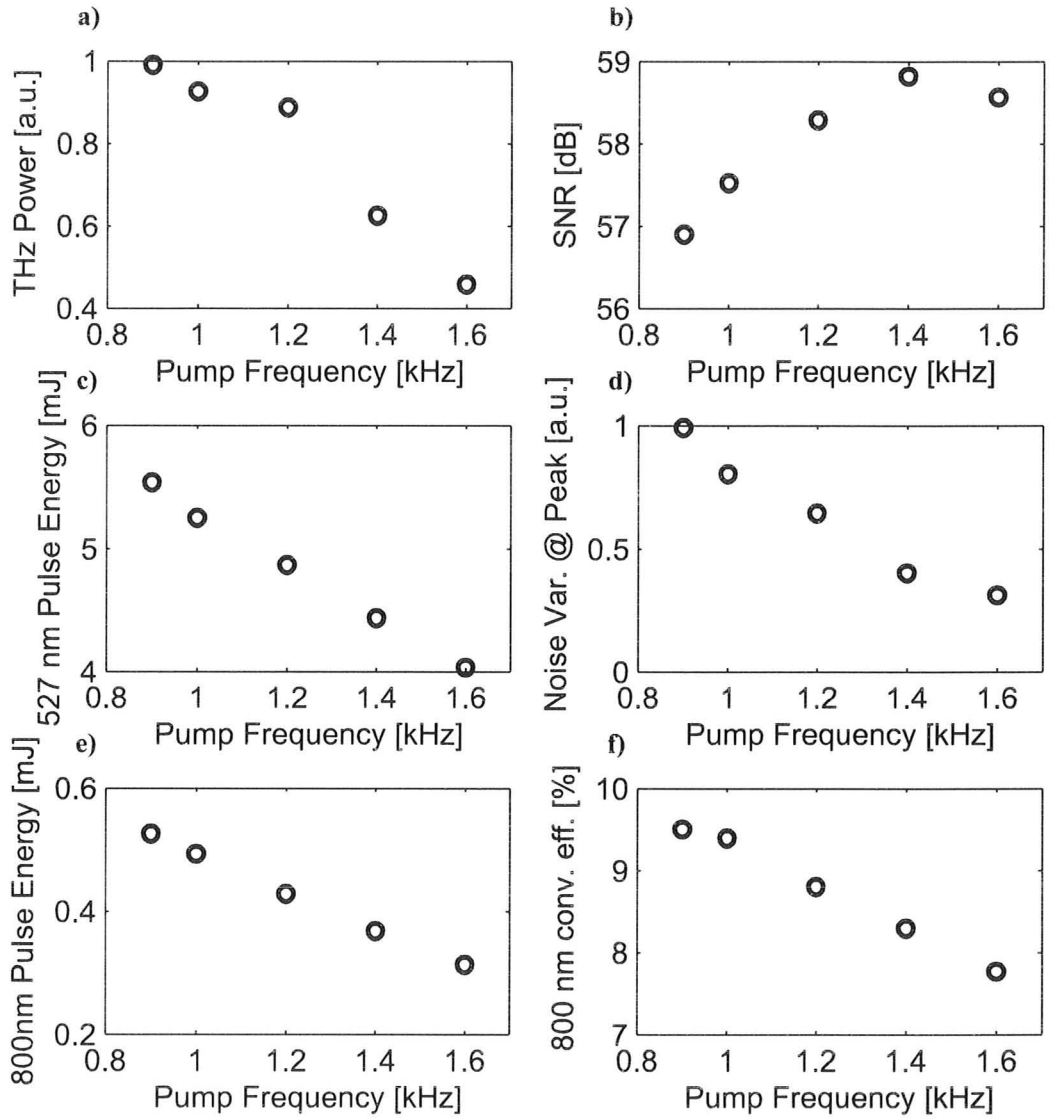

Figure 3.3: Variation of various important physical quantities as the regenerative amplifier pump repetition rate is change: a) THz power calculated over the entire experimental bandwidth, b) signal to noise ratio, which affects the uncertainity of parameter estimates and is optimized at around 1.4 kHz c) pulse energy out of the pump laser decreases linearly with frequency, indicating a near constant average power, d) the noise variance at the peak measured using the process described in section 3.2 e) the 800 nm pulse energy drops off faster than the pump pulse energy f) the conversion efficiency in the regenerative amplifier is higher at lower frequencies; however, going too low risks damage to the optics within the amplifier.

in experiments as it would yield parameter estimates with lower uncertainty given the same experimental conditions.

3.3.2 Mechanical Vibrations in Pellicles

When designing THz-TDS systems based on electro-optic sampling, one of the important geometrical considerations is how to get the optical probe beam collinear with the THz beam. The most prevalent method for achieving collinearity is to use a pellicle beamsplitter constructed from a polymer material that is highly transparent to the THz radiation. The other primary option is drill a hole in the centre of one of the parabolic focussing mirrors within the THz-TDS setup, which inherently introduces some distortion to the THz wavefront.

The THz systems in the Photonics Research Lab all use the pellicle method to achieve collinearity. One significant drawback of pellicles is the possibility of mechanical resonances of the thin membrane. The frequency of these mechanical resonances can be accurately determined by sweeping a noise source, such as a audible speaker, through a range of frequencies. The resonances in the ThorLabs BP145B2 pellicles used in this research are sensitive enough that vibrations from the mechanical chopper used to modulate the generator beam are strong enough to see a noticeable signal. These resonances are often serendipitously noticed as a sinusoidal signal in the acquired THz waveform, even with no THz signal present. The presence of a significant amount of noise without a THz signal present indicates that signal is actually due to the displacement of the probe beam on the detector photodiodes, as indicated in figure 3.4a.

The problem of displacement of the probe beam can be minimized through two mechanisms. The first option is to decrease the path length between pellicle and detection apparatus, so the absolute displacement of the beam is smaller, and potentially less than the photodiode size. Another way to reduce the displacement of the beam is to shrink the spot size on the photodiode by reducing the divergence angle of the probe beam. These two mechanisms can be used in a complementary fashion by using a longer focal length lens in the

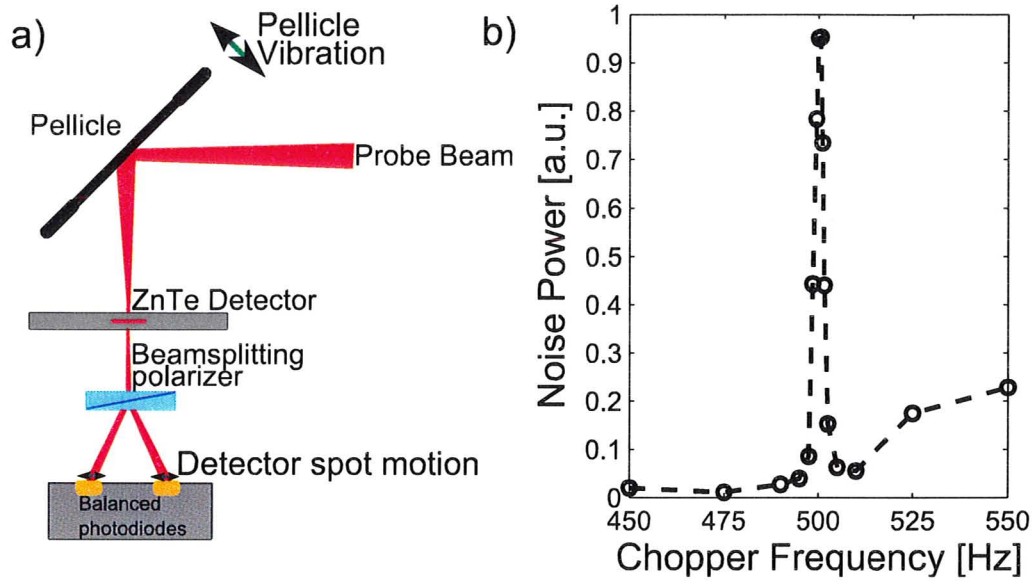

Figure 3.4: a) Periodic noise is introduced to the detected probe signal due to vibrations of the pellicle which shift the physical location of the probe beam on the detector crystal. b) The amplitude of the periodic noise induced on a ThorLabs BP145B2 pellicle.

probe beam, which reduces the divergence angle, and then by reorganizing the system geometry to move the pellicle as close to the detector crystal as possible.

Even if the displacement of the probe beam is reduced to the point where clipping no longer occurs, the mechanical vibrations still result in measurement problems through additional derivative noise. The mechanical vibration of the pellicle results in a physical displacement and thus a path length variation for the probe beam. As mentioned previously, derivative noise is the most problematic type of noise for phase based parameter estimates. It is strongly preferable to reduce the mechanical vibrations by tuning the laser system off the resonance frequency.

As mentioned previously, the laser systems in the Photonic Research Labs are capable of continuous repetition rate tuning around 1 kHz, although with some slight efficiency losses. After some experimentation, 1.1 kHz was chosen as the default pump repetition rate for THz experiments. The divergence

angle of the probe beam was also significantly reduced by switching from a 400 mm focal length plano convex lens, to a 1000 mm focal length plano convex lens. The last measure taken to reduce the effect of the pellicle vibration was the redesign of the detection optics to allow for the photodiodes to be located less than 10 cm downstream from the beam waist of the probe beam. The combination of these efforts virtually eliminates the sinusoidal noise seen previously, when the system is optimally aligned. It should be noted that even a small misalignment in the detection optics can result in the phenomena returning, despite all of these efforts to eliminate it.

3.3.3 Aperture Enhancement

When conducting experiments on solid samples, the THz beam is often focussed to a waist where the sample is placed. In order to find the specific location of the waist, a metal aperture with variable size is placed in the vicinity of the focus. Through an iterative method of moving the physical location of the aperture, decreasing its size, and monitoring the THz signal, the THz beam waist can eventually be found. In typical experiments, the aperture is then switched for a pre-aligned sample which is then measured.

This indirect method for locating the THz beam waist is also an opportunity to investigate one of the more interesting difficulties in dealing with such broadband pulses: the variation of the beam waist with wavelength. The THz pulse contains significant energy over a bandwidth from less than 100 μm to over 600 μm. It is well known that Gaussian optics predicts that a focussed Gaussian beam does not focus to a point, rather to a waist whose diameter, d_0 is dependent on the wavelength λ, the input beam diameter D, and the focal length of the optical element F:

$$d_0 = \frac{4\lambda}{\pi}\frac{F}{D}. \tag{3.1}$$

The input beam diameter of the THz is approximately 1 cm, and the focal length of the parabolic mirrors is 10 cm, thus the expected beam waist is approximately 1.9 mm for $\lambda = 150\mu$m and 5.7 mm for $\lambda = 450\mu$m. To test the

effect of a metal aperture placed at the THz focus, a series of experiments were conducted while the aperture was gradually closed. The size of the variable aperture was calibrated by using drill bits available in the PRL. In the results shown in figure 3.5, it is clear that the simplistic model of the THz field at the focal plane expected from Gaussian optics is not applicable.

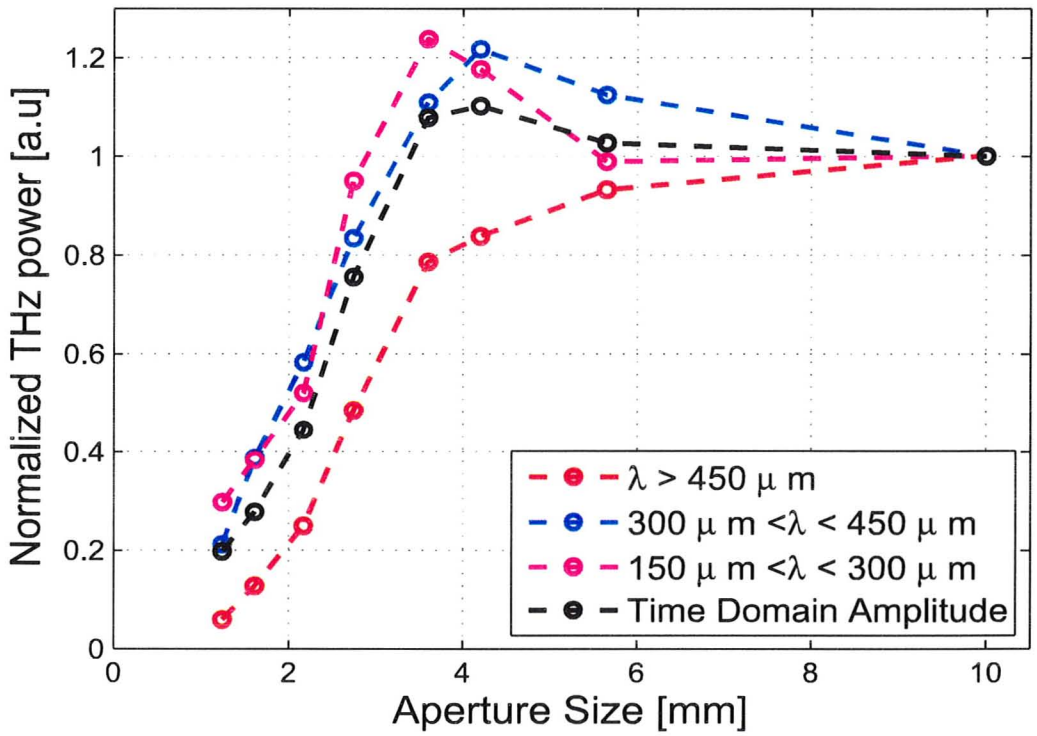

Figure 3.5: Detected THz power through apertures of various sizes in several wavelength regimes. Wavelengths greater than 450 μm show the expected behaviour, but shorter wavelengths show an apparent enhancement effect when the aperture is approximately 10-20x the wavelength of interest.

At long wavelengths, $\lambda > 450\mu$m, the behaviour of the THz power is as expected, with the detected power significantly decreasing once the aperture is smaller than the expected beam waist. At shorter wavelengths, the behaviour is much more complex. At aperture sizes approximately a factor of 2 larger than the expected beam waist, the detected THz power is actually enhanced by the presence of the aperture. In fact, the total detected THz energy is in fact greater with the aperture set at 3.5mm than with it open. Clearly, the

aperture is not creating a THz field, so for an explanation the nature of the detection mechanism must again be considered.

In order to detect the THz electric field, an optical probe is focussed and directed onto a path collinear with the focussing THz beam. The system is aligned such that the THz beam and optical probe focus at the same point in space. However, the focal point of the optical beam is several orders of magnitude smaller than the THz beam waist. Thus, the measurement is effectively a sampling of one region of the THz electric field. While careful alignment can ensure that the sampled region is the most intense region of the THz electric field, this measurement technique is prone to changes in the THz spatial profile. The aperture clearly changes the THz beam profile by introducing diffraction and also through spatial filtering of various frequency components.

The results of figure 3.5 indicate that, for wavelengths shorter than 450 μm, closing the aperture actually results in a tighter beam profile at the detector crystal and thus a more intense electric field. If the THz beam were truly Gaussian out of the generation crystal, this effect should not occur. However, previous data has shown that the 800 nm beam profile is not Gaussian and the 2nd order process which generates the THz radiation in the crystal, combined with the square aperture of the generation crystal, present ample opportunity to distort the beam shape even further.

These results, in some ways, present an opportunity as well. If the lower frequencies are not as desirable for an experiment, the detected THz field can be increased by as much as 30% simply by filtering the beam with an appropriately sized aperture. Through the introduction of additional focussing optics, additional manipulation of the beam profile may be possible resulting in detected field enhancement beyond the 30% possible using the current setup.

3.3.4 Chirp in THz Pulses

When dealing with broadband pulses, the phenomena of chirp is of particular interest. Chirp is generally described as a frequency dependent delay difference and prevents the peak intensity and duration of a pulse from reaching Fourier transform limits. Previous experiments have shown the presence of temporal

chirp in generated THz pulses, although the phenomena has not been studied in detail (Beard *et al.*, 2002). By using the short-time Fourier transform (STFT) with a window width of 1.01 ps and a shift of 0.27 ps, the chirp was extracted from a typical THz-TDS dataset. A clear trend of higher frequency components arriving later in the pulse is apparent in figure 3.6 indicating that positive chirp is present. Approximately 750 fs of chirp occurs over a frequency difference of 2 THz.

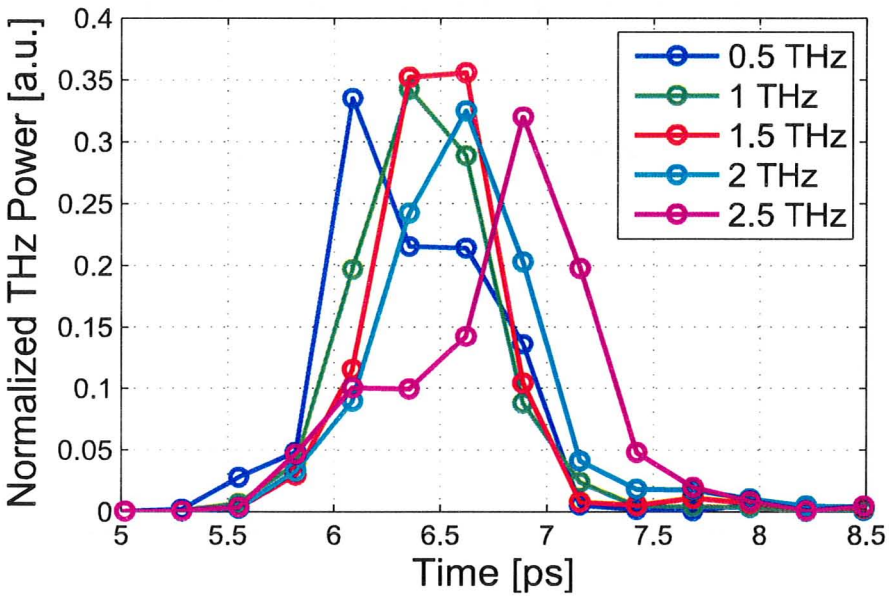

Figure 3.6: Evidence for chirp in a THz signal generated from optical rectification in ZnTe. The relative power was extracted by using the short-time Fourier transform with a window shift of 0.27 ps and a width of 1.01 ps. The THz power was normalized by summing each frequency component over all time windows.

As an experimental diagnostic, chirp is of interest as it effectively will increase the duration of the THz pulse well beyond the desired single cycle radiation often described in theoretical studies. In the THz focal plane, chirp plays an interesting role in changing the evolution of the energy distribution. As the beam-width at the focus is also frequency dependent and the low frequency components arrive first due to positive chirp, the outer regions of the focal plane receive energy earlier and potentially with shorter duration than

the center of focal plane. In experiments where the THz power has the potential to perturb the sample significantly, the effect of chirp at the focal plane may need to be considered.

3.4 THz Polarimetry

Typically THz-TDS studies focus on transmission or reflection of linearly polarized radiation and utilize polarizers to ensure a highly polarized input to the sample and measured output at the receiver. By forcing the input and output polarization to a single linear axis, potentially relevant information on sample anisotropy is discarded.

The focus of this discussion is to demonstrate that the common practise of using polarizers is not necessary when electro-optic detection is utilized, and equivalent or better performance can be achieved through careful adjustment of the experimental setup. The removal of the polarizers from the experimental picture not only reduces cost, but allows access to highly relevant details regarding sample anisotropy.

We refer to our method for accessing anisotropy information as THz polarimetry as the key information is extracted via the change in the polarization state of an arbitrarily polarized THz field. Several polarimetric methods for THz-TDS have already been developed, typically based on techniques used for infrared spectroscopy (Kanda *et al.*, 2007; Masson and Gallot, 2006).

3.4.1 Current THz Polarimetry Methods

Within the THz research community, numerous approaches have been used to conduct THz polarimetry. All of these systems utilize wire grid polarizers in some capacity to either refine the polarization state, or as an analyser before the detection mechanism. Cross-Nichol polarizer configurations, which require three measurements in order to determine the polarization state, have been used to study chiral metamaterials (Kanda *et al.*, 2007). In another study, an analyser polarizer was rotated in 10° increments in order to characterize a waveplate at THz frequencies (Masson and Gallot, 2006). A similar method of

rotating polarizers was also used to characterize the elliptical THz polarization state achieved by using multiple pulses for THz generation in ZnTe (Shimano *et al.*, 2005).

These polarimetric methods require the use of at least two, and often three wire-grid polarizers. An example of how these polarizers could be used in a THz-TDS system is shown in figure 3.7. In this case, the first polarizer is used to create a polarization state at 45° in the laboratory x-y plane. The second polarizer is then used to decompose this polarization state into the x and y electric field components. In this case, the first polarization creates a limit on the extinction ratio, as the initial THz field is at 45° to the polarizer axis.

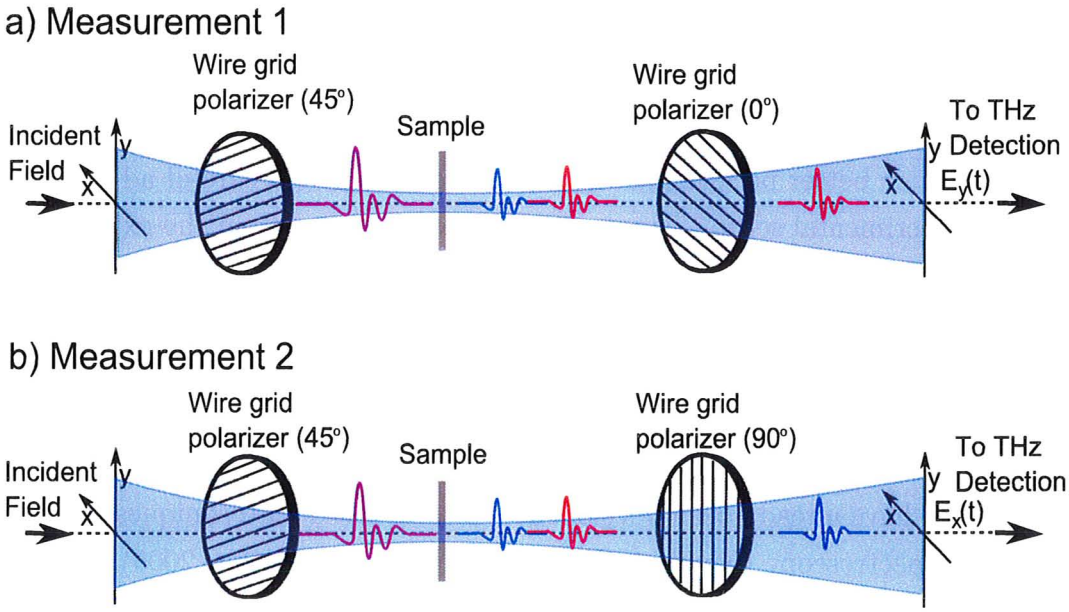

Figure 3.7: Typical setup for measuring both THz electric field components using either electro-optic crystals or photoconductive antennas for generation and detection. By rotating the second polarizer, the component measured by the detector is changed.

Attempts have been made to simultaneously measure both electric field components by using a directional photoconductive antenna fabricated on Fe^+ ion-implanted InP (Castro-Camus *et al.*, 2005). The device was fabricated by sputtering gold contacts and transmission lines on top of the substrate while leaving two orthogonal gaps between the contacts and ground, as shown

in figure 3.8. While this method does eliminate the need for polarizers, the extinction ratio of these devices is limited to much less than 10^3.

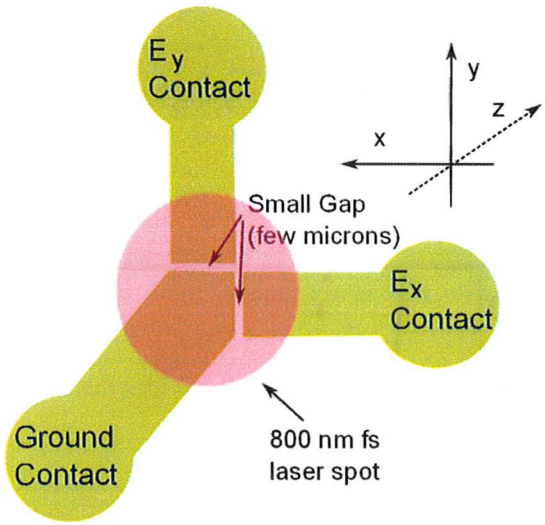

Figure 3.8: Diagram illustrating the multicontact photoconductive antenna used for polarimetric THz-TDS by Castro-Camus *et al.* (2005).

Wire Grid Polarizer Performance

Current methods for THz-TDS polarimetry typically use several wire-grid polarizers. These polarizers are essentially an array of free-standing or embedded wires in tension across a wide aperture. As the wires are conductive at THz frequencies, an electric field component parallel to the wires results in a current and thus a significant reduction in the transmitted power.

In the region below 1 THz, these polarizers can perform extremely well, with transmission as low as 10^{-5} for the parallel component. Data sheets published by a manufacturer of these polarizers, Microtech Instruments, show that the transmission of the parallel component increases with the square of frequency. For THz-TDS measurements, which may have a Q factor of 0.1, this results in a reduction of the extinction ratio by at least a factor of 100 over the experimental bandwidth. The predicted extinction ratio performance of Microtech Instruments' best performing polarizers are shown in figure 3.9.

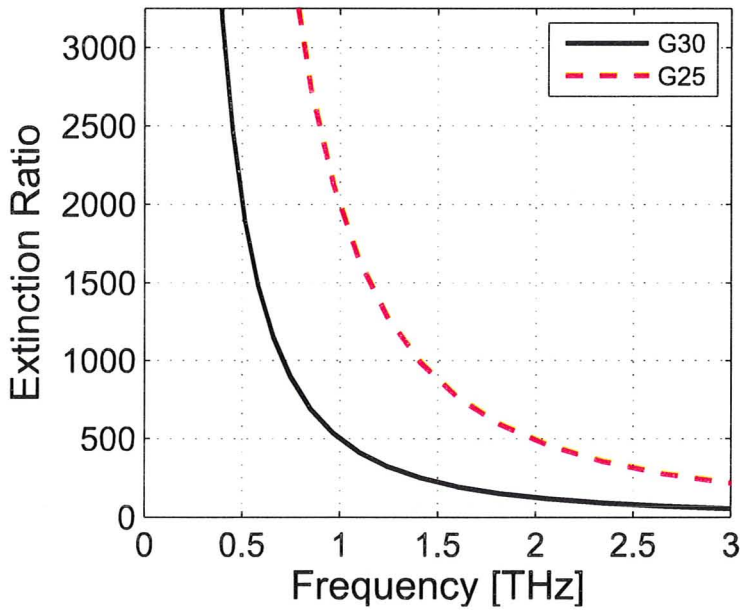

Figure 3.9: Predicted extinction ratio performance for the wire-grid polarizers available from Microtech Instruments that are often used in THz-TDS studies. The primary source of the reduction in extinction ratio is the transmission of the component parallel to the wires, which increases as f^2.

Although the wire grid polarizers are not useful as the polarization analysis element for the polarimetric system developed in this work, they are still have utility. In later experimental data, the trend generally shows that lower THz frequencies have a much less pure linear polarization state than higher frequencies. In this case, a single wire grid polarizer would still be useful to increase the extinction at frequencies below 0.5 THz.

3.4.2 Polarimetric THz-TDS without Polarizers

In Chapter 2, the angular dependence of THz radiation generated from optical rectification in ZnTe and angular dependence of electro-optic detection were discussed in detail. It was clearly demonstrated that the signal detected by the photodiodes was strongly dependent on the angle between the THz field, probe field and (001) axis of the ZnTe crystal (Planken *et al.*, 2001). For reference, the geometry of interest is presented in figure 3.10, with the angles θ and ϕ being of primary interest.

In these conditions, the detected intensity difference at the photodiodes, which is proportional to the THz electric field, is given by eq. 3.2. Examining this relationship gives insight into how it can be exploited for polarimetry. It is relatively straightforward to verify that the global maxima of eq. 3.2 occur when $\phi = n\pi/2$ and $\theta = \pm\pi/2 + m\pi$, where m and n are integers.

$$\Delta I(\theta, \phi) \propto \cos\theta \sin 2\phi + 2\sin\theta \cos 2\phi \tag{3.2}$$

As the period of the ϕ maxima is $\pi/2$, for every quarter rotation of the probe electric field relative to the crystal axis, another maxima is possible. However, the response to θ, the angle between the THz electric field repeats only every 180° . If we consider rotating the entire crystal clockwise by an angle Θ, then both θ and ϕ are rotated by the same amount, as in eq. 3.3.

$$\Delta I(\theta, \phi, \Theta) \propto \cos(\theta - \Theta) \sin 2(\phi - \Theta) + 2\sin(\theta - \Theta) \cos 2(\phi - \Theta) \tag{3.3}$$

If $\Theta = \pi/2$, and the system was originally setup to maximize the detected

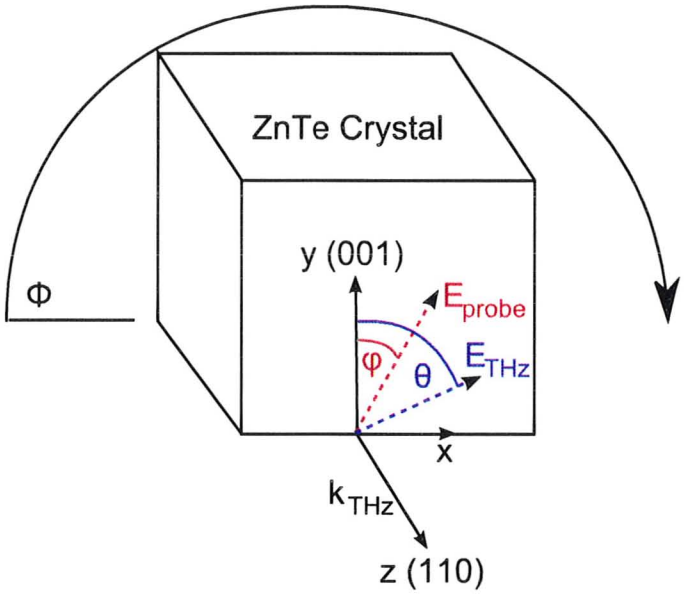

Figure 3.10: Geometry of the THz and 800 nm probe electric fields within the ZnTe crystal. The amplitude of the detected signal on the two photodiodes depends significantly on the angle between both electric fields and the (001) axis.

electric field, then the detected response should be 0. However, if the THz electric field of interest was actually polarized at 90° from the original field, then the system would again be at a detection maxima. In other words, if the original position of the crystal made it sensitive to the x component of the THz electric field, then by rotating the detection crystal by 90° , the signal detection should be directly proportional to the y component. Thus, by simply rotating the detection crystal, selectivity between both electric field components can be achieved.

While the ability to rotate the detection crystal and achieve polarimetric measurements would appear to be a simple solution, there are numerous factors which significantly complicate actually achieving this. The following sections discuss the actual implementation of this scheme and the issues which must be addressed. The aforementioned procedure assumes that perfectly linearly polarized THz radiation is available with a known orientation. Achieving both linear polarization and knowing the orientation is far more difficult at

THz frequencies than at optical frequencies. It should be noted that having a single wire grid polarizer for initial alignment purposes would significantly simplify the procedure. As no wire-grid polarizers, which cost several thousand dollars and are extremely fragile, were available in the PRL, the procedures documented below were required.

3.4.3 A Method for Optimal Alignment

Before getting into significant detail about the optimization of THz polarimetric setup, the overall design needs to be discussed. The diagram in figure 3.11 gives a to scale overview of general setup used for polarimetry.

The generation laser for the system is a regeneratively amplified Ti:sapphire femtosecond laser system which has an output of around 500 μJ per pulse at 1.1 kHz. The beam is split off into two separate paths, with 95% of the energy being used for generation and approximately 5% being directed towards a movable delay stage to be used for electro-optic sampling.

On the generation side, a mechanical chopper blocks every other pulse, reducing the effective repetition rate for generation to 550 Hz. This reduction is necessary in order to use lock-in detection, as an on and off state must be detectable on the photodiodes. After the chopper, the first key addition for the polarimetric system is a standard optical polarizer used to ensure the polarization orientation of the generation beam.

Before the setup was constructed, two polarizers were calibrated to be precisely crossed through a series of optical measurements using high sensitivity photodiodes. One of these polarizers was placed in the generator beam path and one was placed just before the pellicle in the detection beam path. These polarizers allow an effective absolute frame of reference when optimizing the polarization of the THz signal. Without them, it would be extraordinarily difficult, if not impossible to optimize the polarization state of the THz signal due to the indirect measurement method and lack of THz polarizer. It is also important to note that, over the optical beam path, the polarization angle is prone to a slight change. One possible source of the accumulation of polarization rotations are the slight rotations introduced by the numerous mirrors in

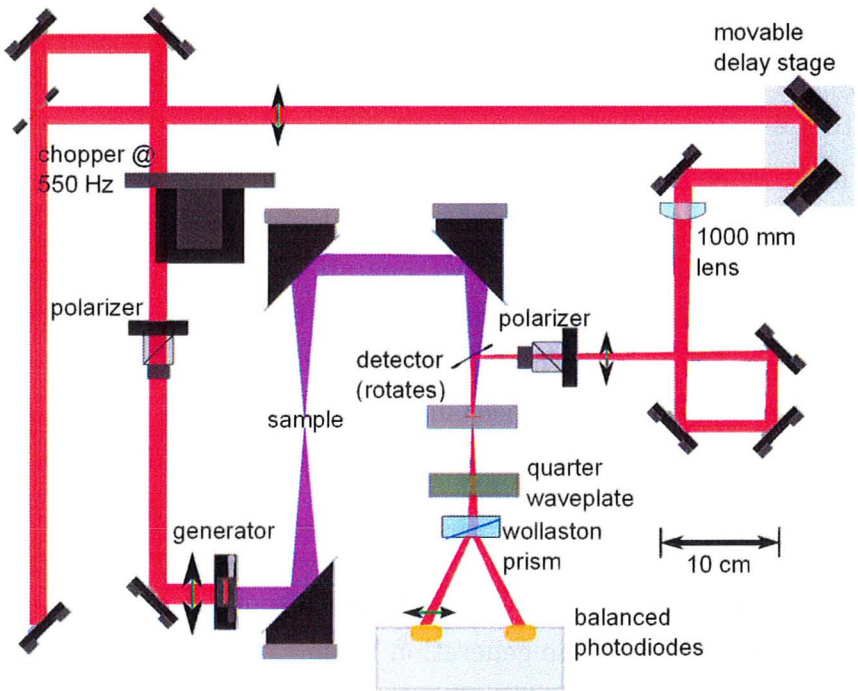

Figure 3.11: To scale diagram of the polarimetry setup developed and optimized in this thesis.

the setup which may have not have perfectly equivalent Fresnel coefficients.

The process of optimizing the alignment of the THz-TDS system with two ZnTe crystals with unknown axis locations must be done iteratively. The polarization angle of the THz electric field is highly dependent on the angle between the (001) axis and the 800 nm generator beam polarization. For optimal generation, the 800 nm polarization should be 54.73° from the (001) axis (Chen *et al.*, 2001). In this orientation the polarization of the THz electric field is parallel to the 800 nm electric field. At all other angles, except for the 180° rotation from 54.73° , the THz electric field is non-parallel to the 800 nm field. This polarization rotation plays a very important role as the initial placement of the generator crystal will likely result in THz polarization state that is at some unknown angle to the laboratory $x - y$ plane.

One way to begin optimizing the system is to rotate the detector crystal through an angle of at least 180° , taking a THz scan at every 5-10° . Doing this rotation and then calculating the power at each detector angle should yield a relationship of the type shown in figure 3.12a. The solid line in figure 3.12 shows an optimally aligned system. In the optimally aligned case, the two secondary maxima in THz power are of equivalent height. As the system becomes unaligned, the secondary maxima shift in position slightly, but in height even more significantly, with the direction being dependent on the direction of the shift.

The directional change of the secondary maxima indicates there is a relatively straightforward way to optimize the generator crystal. Once the first 180° rotation of the detector crystal has been completed, the generator crystal can be rotated in an effort to reduce the difference in the secondary maxima. In succeeding rotations of the detector crystal it is not necessary to rotate through a full 180° , rather only the height and location two secondary maxima need to be determined. This reduction in required scans is important as a THz scan takes at least a minute, and a full 180° rotation can easily take a half-hour. By only measuring the secondary maxima, this can be reduced to 5 - 10 minutes. It should be noted that the secondary maxima are normally separated by about 125° .

The process of stepping the rotation of the generator crystal while scanning

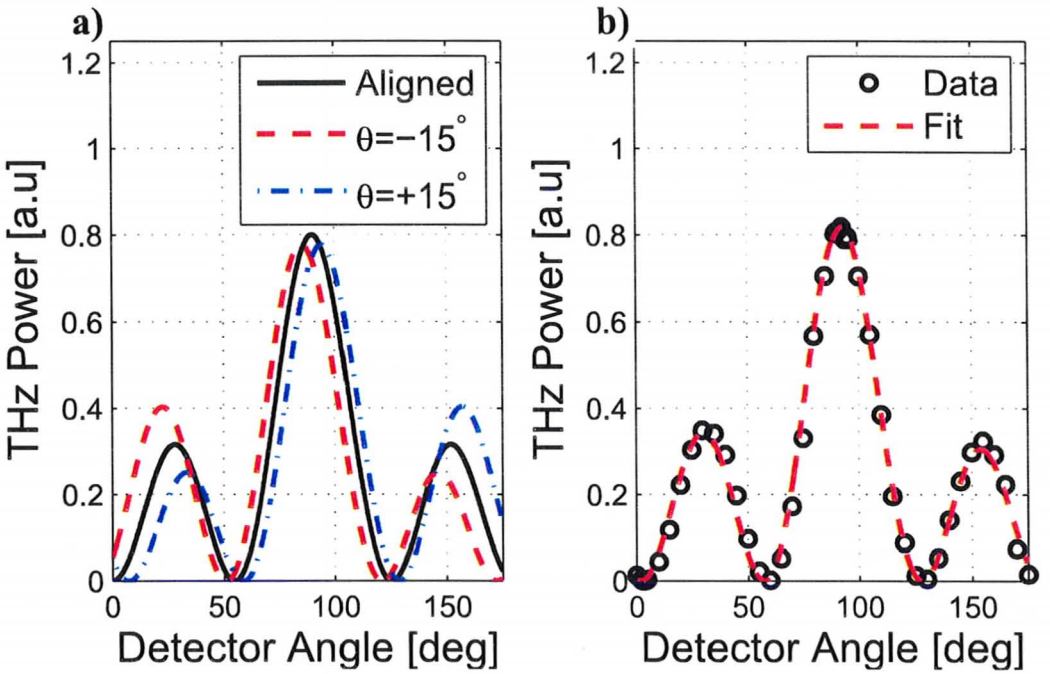

Figure 3.12: Dependence of the detected THz power on the angle of the detector crystal. a) Simulated relationship with the THz electric field $\pm 15°$ off from the optimal positioning. The location and height of the secondary maxima are highly dependent on the THz field angle, whereas the primary peak is significantly less sensitive. b) A Typical measurement of detected THz power with a moderately well aligned system and a parametric fit to the data. In this data set the THz field is estimated to be $3.65°$ from optimal positioning.

through numerous detector angles allows the system to be slowly optimized. Alignment of the generator crystal to within 1° of optimal from an arbitrary position can often be achieved in about 10 iterations, taking approximately 2 - 3 hours. Optimization beyond 1° of optimal often takes much longer and numerous effects come into play that complicate the issue. As the system becomes closer and closer to alignment, the step size of the generator crystal rotation needs to be decreased quite rapidly. For the optimal alignment data shown in this thesis, the generator step size was reduced to 0.04° after optimization to within 1° had been achieved.

The standard method of optimization for THz-TDS systems is to sit at the peak of the THz time domain trace and rotate the detector and generator crystal to reach a maximum detected intensity. While this method can be complimentary to the aforementioned method, it can not replace it for alignment of THz-TDS polarimetric systems. The first problem with measurement of the peak is that changes in the optical path length alter the measurement location and make frequent adjustment of optical delay necessary. The second problem is that the sensitivity of the peak to changes in polarization state is quite low, that is quite significant changes in the angle of the generator are required to see a change in the peak. This lack of sensitivity makes it very difficult to achieve alignment to within a fraction of a degree, something that can be done through the secondary maxima monitoring.

Later in this work, an automated rotation stage was purchased for use with the detector crystal. This stage permitted highly accurate and repeatable rotations of the detector crystal and enabled an improvement on the alignment algorithm. For the initial alignment, a complete scan such as in figure 3.12, was done and the data fit using the theoretical relationship of eq. 3.3. The parameters for this fit allowed the quick determination of the THz electric field angle which could then be used to determined the necessary rotation of the generator crystal. While this method did greatly improve the speed of the initial steps of the alignment, the later steps, beyond 1° of optimal for the generator crystal, still required the slow and tedious task of small rotations of the generator crystal.

3.4.4 Extinction Ratio Limitations

The extinction ratio is defined as the ratio of the power of desired electric field polarization, to the power the orthogonal undesired electric field polarization. By using the method of optimization of the generator and detector crystal angles described above, the THz-TDS system can be tuned to have a high extinction ratio on the order of 10^4 (40dB) when averaged over the bandwidth. A spectrum of a typical extinction ratio after such an optimization is shown in figure 3.13.

What is immediately striking is the significant frequency dependence of the extinction ratio. The variation of 20 dB over a range of just a few hundred GHz is a variation of two full orders of magnitude. While the average extinction ratio of the measurement of figure 3.13 is still quite impressive, being an order of magnitude better than anything in literature, it is less than optimal for use as a sensitive detector of polarization state changes.

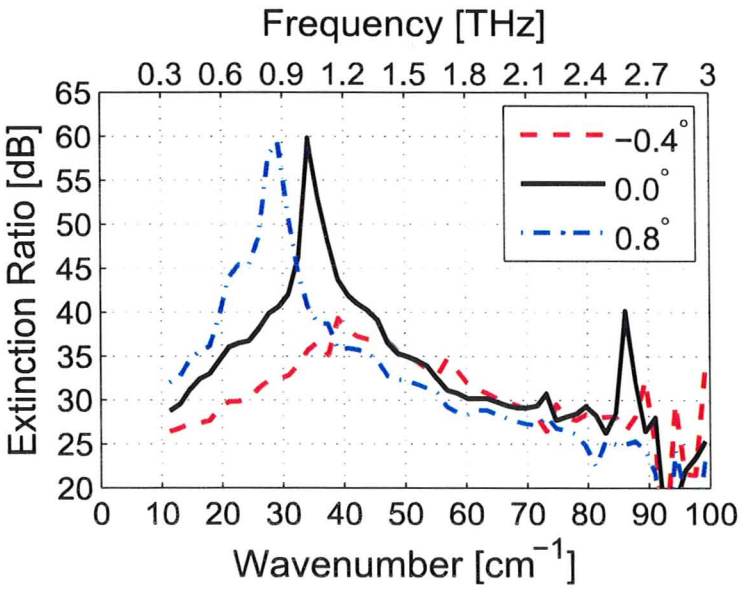

Figure 3.13: Typical extinction ratio measurement after optimization of the setup described in figure 3.11. The extinction ratio is extremely dependent on the frequency.

In order to understand the root cause of the frequency dependent extinction

ratio, it is necessary to examine several possible causes for this effect.

Birefringence in ZnTe

Birefringence is a likely candidate for limiting the extinction ratio as a birefringent material should alter the polarization state from a linear state to an elliptical state. The degree of ellipticity introduced is dependent on the birefringence of the material and the path length of the material the beam has travelled through. Both the generator and detector ZnTe crystals are known to be birefringent. This birefringence can quickly be verified in the detector crystal by blocking the THz beam and then rotating the detector crystal. In this case, the detected signal on the lock-in amplifier goes through several maxima and minima as the polarization state of the optical beam is altered by the variation in index of refraction.

When several materials are birefringent, the likely result would be a highly frequency dependent extinction ratio, as the combination of polarization rotations in the system would likely result in a small band of frequencies that have the necessary rotation to be almost optimally polarized. Despite this being a likely scenario, later evidence shows that birefringence is unlikely to be the root cause of the limitation to extinction ratios.

Birefringence in HDPE

While not indicated in the diagram of the THz-TDS setup, a thin piece of black HDPE is used after the generator crystal to block the 800 nm generator beam from continuing through the optical setup. An opaque material is absolutely necessary as any remaining optical power would be focussed at the sample, likely damaging it, and then again at the detector crystal, likely drilling a hole quickly through it.

Unfortunately, it will be later demonstrated that this HDPE material is slightly birefringent. As the axis of this birefringence is not aligned with the physical axis of the material, in most of the measurements conducted early in this thesis, the birefringence was present and likely was part of a limiting factor in the extinction ratio. A birefringent sample introduces a frequency

dependent rotation of the THz electric field which cannot be compensated for in aligning the system.

Pellicle Fresnel Coefficients

The pellicles used for achieving a collinear path between the THz beam and the 800 nm probe beam were obtained from Thorlabs. While these pellicles work well, their data sheet does state that P and S polarized light are transmitted with different coefficients. The values of coefficients are not stated in the data sheet. As the pellicles are used at non-normal incidence, both P and S components must be considered and thus a slight polarization rotation should be expected. Part of this rotation is likely compensated for during the optimization procedure, but it would be strongly preferable to avoid the use of pellicles in the THz-TDS system. The pellicles can be removed by drilling a small hole in the centre of the final parabolic mirrors to have a small hole drilled in the centre. The probe beam can then be directed down this hole and thus achieve collinearity without requiring a pellicle.

Non-Normal Incidence

Another potential source of a limited extinction ratio is non-normal incidence of either the generator beam on the generator crystal, THz electric field on the detector crystal, or probe beam on the detector crystal. With the exception of the THz electric field, this effect can be eliminated through careful alignment of the THz-TDS setup and is not believed to be a key contributor to the limited extinction ratio.

Broadband Effects

Despite the efforts to minimize all the aforementioned effects, the broadband extinction ratio was still limited to the order of 10^4. In order to increase the extinction ratio further, it was hypothesized that the broadband nature of the 800 nm pulse could actually play a role in limiting the extinction.

The 800 nm pulse has a FWHM bandwidth on the order of 50 nm, corresponding to a Q factor of approximately 16. While this is far narrower than the THz pulse, it is certainly far from a monochromatic source. Within the ZnTe detector crystal, the THz and 800 nm pulses overlap and the birefringence induced by the THz pulse results in an induced ellipticity on the 800 nm pulse. This induced ellipticity will be frequency dependent, as the introduced phase delay is proportional to the frequency of the 800 nm electric field.

For thick crystals, the coherence length variations in ZnTe work to reduce the effect of the frequency dependent phase delay introduced by the birefringence. While the coherence length across the THz bandwidth is greater than 2 mm between 800 nm and 825 nm, below 790 nm, the coherence length is halved to around 1 mm across much of the experimental bandwidth. The reduction in coherence length should result in a shorter effective length of interaction for the higher frequencies (i.e. shorter wavelengths) of the 800 nm pulse and less polarization rotation.

The final broadband interaction to consider is within the $\lambda/4$ waveplate used to balance the photodiodes. Again, the waveplate is cut from a material that is birefringent and thus provides frequency dependent phase delay across the bandwidth of the optical pulse. The variation with frequency is the same as the induced birefringence in the ZnTe and so these two effects build upon each other. While the effect in the ZnTe crystals are unavoidable, the introduced frequency variation from the waveplate can be reduced by obtaining an achromatic waveplate, or removed completely by removing the waveplate entirely.

3.4.5 Optimal Extinction Ratio Measurements

With the knowledge that the $\lambda/4$ waveplate could play a key role in limiting the extinction ratio, the waveplate was removed from the setup. Removing the waveplate results in a very significant reduction in the sensitivity of the detection mechanism, on the order of 10^1. The probe electric field was also rotated by 45° to allow effective splitting of the 800 nm field by the fixed Wollaston prism used. The result of these changes can be clearly seen in the

extinction ratio measurement of figure 3.14.

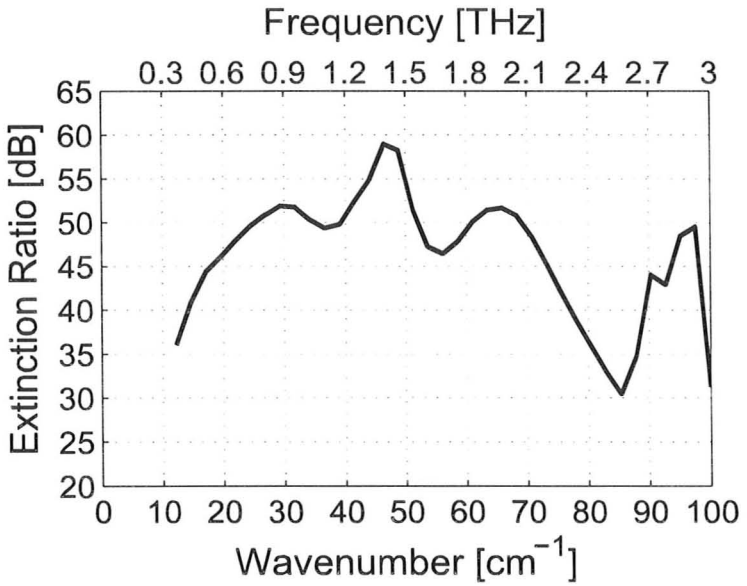

Figure 3.14: To scale diagram of the polarimetry setup developed and optimized in this thesis.

By removing the $\lambda/4$ waveplate, the extinction ratio has been increased to almost 50 dB across the entire bandwidth. The broadband extinction ratio has also increased by an order of magnitude to 10^5, and is very near to the signal to noise ratio in the setup. Thus, it would appear that after the system has been properly aligned, broadband effects are the key limiting factor to the extinction ratio. In designing a polarimetric THz-TDS setup, the trade-off between the reduced sensitivity and increased extinction ratio must be considered in order to achieve the best experimental results.

3.4.6 Mathematics of Polarimetric Analysis

In order to succinctly derive the necessary polarimetric relations to determine the materials properties of samples under test, Jones calculus is typically used (Jones, 1941). In Jones calculus, the polarization state of light is represented in a Cartesian space by a two element vector, i.e. the electric field strength

in the x and y directions, with propagation assumed to be along the third dimension, z (Hecht, 2001). It is possible to extend the Jones calculus formalism to arbitrary propagation; however, this extension significant complicates the math required with no discernible benefit for the polarimetric setup used in these experiments (Gil, 2007).

The effect of an individual optical element on the polarization state of incident electromagnetic radiation is represented as complex 2x2 matrix. The appropriate matrix for an individual optical element can be readily found in a number of sources, such as Hecht (2001). The effect of rotation an optical element around the z axis can also be modelled with an appropriate rotation matrix.

In the case of THz-TDS polarimetry, the Jones calculus is used to model the transmission through a sample compared to the transmission through a reference. In this experimental geometry, the effect of the sample is considered as a single combined Jones matrix and thus is related to the reference measurement as:

$$\tilde{\mathbf{E}}^{\mathbf{samp}} = \tilde{J}^{samp}\tilde{\mathbf{E}}^{\mathbf{ref}}. \tag{3.4}$$

The following analysis assumes that the difference in the Fresnel reflection and transmission coefficients at each interface are negligible. The analysis could be expanded to include these differences, by adding additional Jones matrices describing partial polarizers to the eq. 3.4; however the correction factor is generally small for the range of anisotropy studied in this work. As an example, for a material with $\Delta n = 0.1$ and a $n_o = 2.0$, the relative difference in Fresnel coefficients is only 1.5 %.

The coordinate system is described by x', y', z' for the sample reference frame and x, y, z for the laboratory reference frame. Assuming that the material is of thickness, d and can be described completely by two complex indices of refraction, $n_{x'} + i\kappa_{x'}$ and $n_{y'} + i\kappa_{y'}$, one along each principal axis, and the sample reference frame is merely a clockwise rotation around the z axis by an angle θ, then $\tilde{J}^{samp}$ can be written as:

$$J^{\tilde{samp}} = \begin{bmatrix} \tilde{m}_{x'}\cos^2\theta + \tilde{m}_{y'}\sin^2\theta & (\tilde{m}_{x'} - \tilde{m}_{y'})\cos\theta\sin\theta \\ (\tilde{m}_{x'} - \tilde{m}_{y'})\cos\theta\sin\theta & \tilde{m}_{x'}\sin^2\theta + \tilde{m}_{y'}\cos^2\theta \end{bmatrix}. \tag{3.5}$$

The terms $\tilde{m}_{x'} = \exp\left(-i\left(d\omega/c\right)\left(n_{x'} - i\kappa_{x'}\right)\right)$ and $\tilde{m}_{y'} = \exp\left(-i\left(d\omega/c\right)\left(n_{y'} - i\kappa_{y'}\right)\right)$ are the materials dependent parameters (Jones, 1941). To proceed further in the analysis, either a rigorous mathematical approach must be taken, or some simple assumptions made about the reference measurement and the experimental procedure. In order to motivate the more rigorous approach, it is assumed the reference electric field is perfectly polarized in the x direction and the sample is rotated to θ =45° from the laboratory frame. Under these conditions, eq. 3.4 can then be simplified:

$$\tilde{\mathbf{E}}^{\mathbf{samp}} = \tilde{J}^{samp}\begin{bmatrix} 1 \\ 0 \end{bmatrix} = \frac{1}{2}\begin{bmatrix} \tilde{m}_{x'} + \tilde{m}_{y'} \\ \tilde{m}_{x'} - \tilde{m}_{y'} \end{bmatrix}. \tag{3.6}$$

In systems were the dichroism is small: $\kappa_{x'} \approx \kappa_{y'}$, then the κ term merely results in an overall amplitude factor which is common to all elements in the vector and it can be simply factored out. If the real part of the index of refraction is then simplified such that $n_{avg} = (n_{x'} + n_{y'})/2$ and $n_{diff} = (n_{x'} - n_{y'})/2 = \Delta n/2$, then:

$$\tilde{\mathbf{E}}^{\mathbf{samp}} \propto \begin{bmatrix} \exp\left(-in_{diff}d\omega/c\right) + \exp\left(-in_{diff}d\omega/c\right) \\ \exp\left(in_{diff}d\omega/c\right) - \exp\left(-in_{diff}d\omega/c\right) \end{bmatrix} \exp\left(-in_{avg}d\omega/c\right) \tag{3.7}$$

The complex exponentials of the each electric field component in eq. 3.7 can then be rewritten as sinusoids: $\tilde{E}_x^{samp} \propto \cos\left(n_{diff}d\omega/c\right)$ and $\tilde{E}_y^{samp} \propto i\sin\left(n_{diff}d\omega/c\right)$. Finally, taking the magnitude of the ratio of components, the birefringence, Δn can be related to the measured electric fields:

$$\Delta n = \frac{c}{df\pi}\tan^{-1}\left(\frac{\left|\tilde{E}_y^{samp}\right|}{\left|\tilde{E}_x^{samp}\right|}\right) \tag{3.8}$$

The result of eq. 3.8 clearly shows the motivation for pursuing the method

of polarimetry for measurement of the birefringence. Using this methodology, the birefringence can be determined by a measurement at a single orientation of the sample while only requiring the ratio of the amplitudes of the transmitted electric field components. Using the amplitudes for birefringence determination, rather than the relative phase delay, significantly reduces the effects of path length drift and Fabry-Perot reflections on the uncertainty and systematic error in birefringence estimates.

While eq. 3.8 is attractive due to its simplicity, several problems exist with using it directly. Numerous assumptions were stated throughout the derivation, one of which was the assumed polarization purity of the input electric field. While extinction ratios in excess of 10^5 have been achieved, these ratios are far from the norm. A more typical extinction ratio is on the order of 10^3, which is often reduced to the order of 10^1 when the amplitude ratio is considered, instead of the power ratio. To offer a more mathematically rigorous polarimetric analysis method, the polarization purity assumption must be revisited.

Returning to eq. 3.5, the terms of the exponentials can be expanded and simplified using trigonometric relations to yield a symmetric matrix which has the form of: (Kanda *et al.*, 2007; Naydenova *et al.*, 1997)

$$\tilde{J}^{samp} = \begin{bmatrix} \tilde{J}_1 & \tilde{J}_2 \\ -\tilde{J}_2 & \tilde{J}_1^* \end{bmatrix}. \tag{3.9}$$

The simplification of eq. 3.9 is important as it allows rearrangement of eq. 3.4 to solve for $\tilde{J}_1$ and $\tilde{J}_2$, as per eq. 3.10. These two matrix elements can then be related to the physical material properties through appropriate physical modelling.

$$\begin{bmatrix} \tilde{J}_1 \\ \tilde{J}_2 \end{bmatrix} = \begin{bmatrix} \tilde{E}_x^{ref} & \tilde{E}_y^{ref} \\ \tilde{E}_y^{ref} & -\tilde{E}_x^{ref} \end{bmatrix}^{-1} \begin{bmatrix} \tilde{E}_x^{samp} \\ \tilde{E}_y^{samp} \end{bmatrix}. \tag{3.10}$$

As with the simple analysis, use of eq. 3.10 to determine physical parameters requires some assumptions about the physical model and the experimental procedure. If the measurement is taken 45° off the principal axes and the

material assumed to be birefringent, but not dichroic, then a transcendental solution exists for the birefringence:

$$\Delta n = \frac{c}{df\pi} \tan^{-1}\left(\frac{\left|\tilde{J}_2\right|}{\left|\tilde{J}_1\right|}\right). \tag{3.11}$$

In the following discussion, the use of eq. 3.11 is referred to as the advanced analysis method and eq. 3.8 is referred to as the simple analysis method. If the inverse of the extinction ratio is on a similar order to the desired resolution of the estimate, then the advanced method is highly preferable over the simple method. In most THz-TDS polarimetric systems, the extinction ratio is going to be limited to the order of 10^3, so if a resolution of greater than 1% is desired, then the advanced method must be used. A negative consequence of the advanced method is that it requires an additional reference measurement. The simple analysis method actually allows extraction of the birefringence with no reference measurement, assuming the thickness of the sample is known *a priori*. Even if the sample thickness needs to be determined, only $\tilde{E}_x^{ref}$ needs to be measured to extract this information. The advanced analysis cannot be performed without taking a reference measurement that consists of time domain scans of both electric field components.

In the preceding analysis, methods to estimate the linear birefringence were the only methods discussed. Using the same principles and eq. 3.10, appropriate analysis methods can can be rapidly determined for estimating the linear dichroism, circular birefringence, and circular dichroism.

3.5 Conclusion

THz-TDS is an experimental technique that allows exploration of regions of the electromagnetic spectrum that were previously difficult to access. This ability comes with limitations, as the current methods for generation and detection of THz radiation require complicated laser systems and rather fragile experimental setups. In designing a THz experiment, it is important to be aware of the specific challenges that result from the time domain nature of the

experiment. With careful planning and calibration of the experimental setup, many of these challenges can be overcome.

Chapter 4

Applications to Birefringent Materials

The simplest, and perhaps most pervasive, case of anisotropy in materials systems is birefringence. At THz frequencies, birefringence has been measured in semiconductors and dielectrics (Grischkowsky *et al.*, 1990), liquid crystals (Tsai *et al.*, 2003), and oriented natural materials such as wood and paper (Reid and Fedosejevs, 2006), as well as plant leaves (Jördens *et al.*, 2009). The ready availability of birefringent materials offers an ideal test case for a polarimetry system. Birefringence is also an extremely useful property in device design, as optical polarizers, waveplates, beamsplitters and numerous other devices can all be fabricated from birefringent materials.

This chapter focusses on several different birefringent systems found during the course of research, some through chance and others where the birefringence at THz frequencies is well known. In several cases, the anisotropic materials properties were altered through the application of mechanical force and thermal energy. The capabilities of polarimetric methods in THz-TDS are compared to the more commonly employed phase extraction method and the tradeoffs are analyzed.

4.1 Mathematical Review

The most widely used method for obtaining complex index of refraction estimates from THz-TDS data relies upon using the phase of the Fourier transform to determine the real component, n and the magnitude to determine the absorption coefficient, α, which is related to the imaginary part of the index of refraction κ (Griffiths, 1999).

As previously discussed, two key sources of systematic error in THz-TDS experiments are laser power drift and path length drift due to temperature or mechanical vibration. Using the widely accepted, which will be further referenced as the "classical", approach laser power drift error is coupled into the absorption coefficient measurements and path length drift is coupled into the real part of the index of refraction measurements. The laser power drift can be compensated for quite readily by repeating scans; however, the phase error is much more difficult to compensate for. As a result, the classical method typically results in noisier estimates of the index of refraction and more stable estimates of the absorption coefficient.

From chapter 2, the index of refraction can be estimated from the phase delay between a sample and reference scan:

$$n = 1 + c\frac{(\phi_{samp} - \phi_{ref})}{2\pi f d}. \tag{4.1}$$

In order to solve for the absorption coefficient, α, the Fresnel coefficients for the sample must be known *a priori*. As the Fresnel coefficient cannot be fully determined without the absorption coefficient, it is necessary to either resort to solving for the absorption coefficient through an iterative minimization procedure, such as the Newton-Rhapson method, or to assume that κ is small, so that the index of refraction can be approximated by n. Assuming κ is small then:

$$\alpha \approx -\frac{2}{d}\log\left(\frac{|\tilde{E}_{samp}|}{|\tilde{E}_{ref}|}\frac{(n+1)^2}{4n}\right). \tag{4.2}$$

The other relationship used extensively throughout this chapter is the

method to extract the birefringence from the change in polarization state of the THz field. As mentioned at the end of chapter 3, if the polarization purity of input THz field is poor, then the advanced analysis method should be used to estimate the birefringence. As the advanced method requires more scans, an approximation to use the simple method of analysis in the case of a low extinction ratio would be useful. In the case where the polarization angle of the reference electric field is small, then the simple polarimetric analysis can be modified by simply taking the difference of the polarization angles. The birefringence can then be approximated as:

$$\Delta n \approx \frac{c}{\pi f d} \left(\theta_{samp} - \theta_{ref}\right). \tag{4.3}$$

These three relationships are the basis of analysis performed on the samples in this chapter. Where necessitated by the sample, the advanced polarimetric analysis method was also used.

4.2 Polymer Materials

Polymer materials have a long history of being studied through infrared measurements and spectroscopy (Peterlin, 1971). These measurements have allowed insight into the orientation of polymer chains within a material and how the materials properties of the polymer are affected by heating (Wietzke *et al.*, 2009), extrusion (Peterlin, 1971), radiation damage (Clough, 2001) and blending (Turcsnyi *et al.*, 1987).

In this section, two particularly interesting examples of birefringent polymers are discussed. First, a sample of silicone rubber heat-shrink tubing is examined before and after heat is applied. In addition to the change in physical dimension, the tubing exhibits significant changes in birefringence and dichroism. The second set of measurements is particularly relevant the THz-TDS measurements in the PRL as the material, a thin sheet of optically opaque HDPE, is used in all of the experimental setups to block 800 nm beams. In this sample, the relatively small initial birefringence is increased by an order

of magnitude through mechanical stretching of the material. Both of these examples serve to show the superiority of polarimetric analysis for birefringence estimates.

4.2.1 Heat Induced Birefringent Variability

Numerous materials were investigated for birefringence at THz frequencies. While many materials exhibited birefringence, in a subset of materials a significant change in birefringence was also able to be introduced. The ability to induce and perhaps control the level of birefringence is interesting from both an engineering and scientific perspective. As an engineering tool, modification of the birefringence at high speed is useful for creating electro-optic modulators.

While the methods used in this work to induce birefringence are non-reversible and thus are not relevant as an engineering technology, scientific relevance still exists. The level of birefringence in a material is an indication of the ordering of the material on relevant length scales of the radiation used.

One of the most interesting samples measured, was a sample of 1.0 cm diameter unbranded silicone rubber 2:1 heat-shrink tubing obtained from Sayal Electronics. Heat-shrink tubing is manufactured from numerous different polymers, with the most common material for electronic applications being polyolefin. While the mechanism resulting in shrinkage is different for different materials, it generally requires creating a non-equilibrium state within material (Clough, 2001). Radiation is used to partially cross-link the material, which is then heated above its crystalline melting point, stretched, and finally cooled while still stretched. As a result of this process, the material is stretched beyond its normal equilibrium dimensions, later application of heat then allows the cross linked polymers to pull the material back into the state before the initial heat was applied (Clough, 2001).

Sample Preparation

While numerous polyolefin samples were investigated, obtaining high quality measurement results was difficult as the material was typically quite thin, on

the order of 0.1 mm. The silicone rubber tubing, at 0.33 mm provided a much better platform for investigating the changes in materials properties of the heat-shrink tubing.

The silicone rubber tubing was cut lengthwise to obtain a flat strip of material of 2.0 cm by 2.0 cm. The initial thickness of the heat-shrink tubing was measured with a digital caliper to be 0.33 ±0.2 mm. After application of heat using a heat-gun, the thickness increased to 0.62 ±0.2 mm. Applying heat resulted in a decrease in the horizontal dimension of approximately 50%, and a slight decrease of approximately 10% in the vertical dimension as shown in figure 4.1. Thus the application of heat resulted in a slight decrease in the total volume of the material, and thus a higher material density.

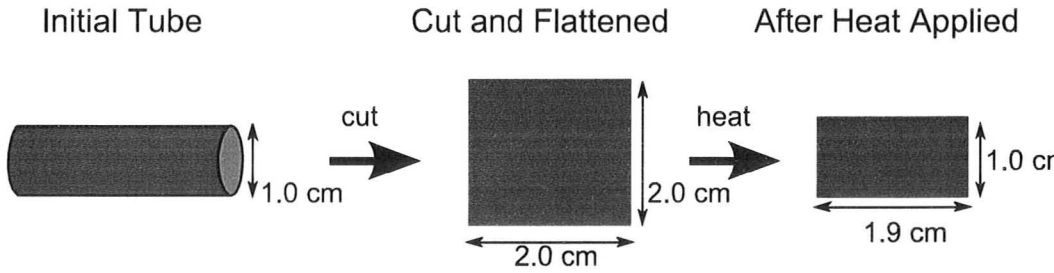

Figure 4.1: Preparation of the heat shrink sample. The initial tube is cut along its axis and then cut into a 2.0 cm x 2.0 cm square. This sample was measured using the THz-TDS polarimetry method. A heat-gun was then used to heat the sample well above its shrink temperature resulting in the reduction in the horizontal and vertical dimensions indicated.

Data Analysis and Results

Determining the anisotropic index of refraction in the heat-shrink tubing using THz-TDS requires several steps. In order to reduce the time needed for scans, only 192 points at a sampling time of 66.7 fs were taken. A series of five reference scans were taken with no sample in place and averaged to reduce variability. The principal axes were determined by measuring the change in polarization state of the THz radiation while rotating the sample through at least 180° . As shown in figure 4.2a, the difference in polarization state is maximized when the incident radiation is polarized 45° off the principal axes

and minimized when the radiation is polarized along one of the principal axes. As a function of frequency, shown in figure 4.2b, the change in polarization angle is almost linear for the off-axis measurements, and effectively negligible when polarized along the axis. As should be expected for heat-shrink tubing designed to reduce in size primarily in one direction, the principal axes line up with the physical dimensions of figure 4.1.

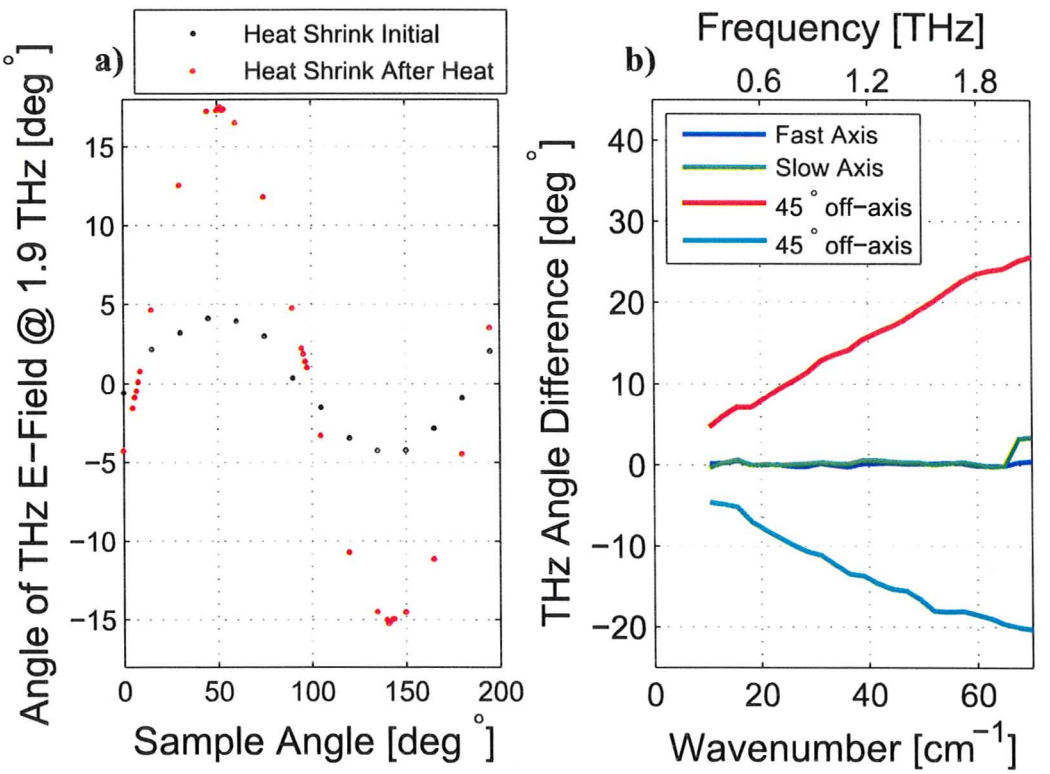

Figure 4.2: Experimental process for determining the principal axes a) The sample is rotated through at least 180° and a polarimetric THz-TDS scan is taken. The angle of the THz electric field is determined. The principal axes are located at the sample angles where there is no change in the THz electric field angle. The location for optimally determining anisotropic materials properties using polarimetric analysis are 45° off of the principal axes b) As a function of frequency, the THz angle difference at the off-axis locations is nearly linear indicating a nearly constant δn. The fast and slow axes are determined by using the phase of the individual THz-TDS scans to calculate the delay relative to a reference pulse.

An inherent part of the process of taking the polarimetric THz-TDS measurements is taking the measurements along the principal axes that would be taken to use for the classical analysis. Using these measurements, the classical analysis was used to extract the index of refraction along both principal axes, as well as the absorption coefficient, both before and after heat was applied. Table 4.1 summarizes the estimates of these properties at 2.0 THz. This frequency range was chosen as the estimates are generally quite poor below 1.5 THz due to several aspects that are discussed later.

Table 4.1: Complex index of refraction estimates extracted using the classical analysis method for heat shrink tubing, before and after application of heat. All estimates are for 2.0 THz (67 cm^{-1}). The real part of the index of refraction, n, is approximately constant over the experimental bandwidth, while absorption coefficient increases in an approximately linear fashion with frequency (or wavenumber).

Axis	n_{before}	n_{after}	change	α_{before} [cm^{-1}]	α_{after} [cm^{-1}]	change [cm^{-1}]
slow	1.59	1.66	+0.07	24	22	-2
fast	1.58	1.63	+0.05	23	18	-5

The classical analysis method makes it quite clear that birefringence exists in the initial stretched material, and is significantly increased after heat is applied. It is also interesting to note that the initial material only has a slight linear dichroism; however, after the heat is applied a quite significant linear dichroism is estimated. The key limitation of the classical method is demonstrated in figure 4.3. As the sample is quite thin, Fabry-Perot reflections within the material cannot be neglected. These reflections, as explained in Appendix B, result in sinuisoidal variations in the magnitude of the estimated transfer function. More importantly the phase is also significantly distorted, which in turn distorts the estimate of index of refraction. The distortions along each principal axis are slightly different and when taking the difference between the estimated indices, as is done to determine the birefringence, the distortion is significantly enhanced. The net result, shown in figure 4.3a and b, is a birefringence estimate that is difficult to interpret.

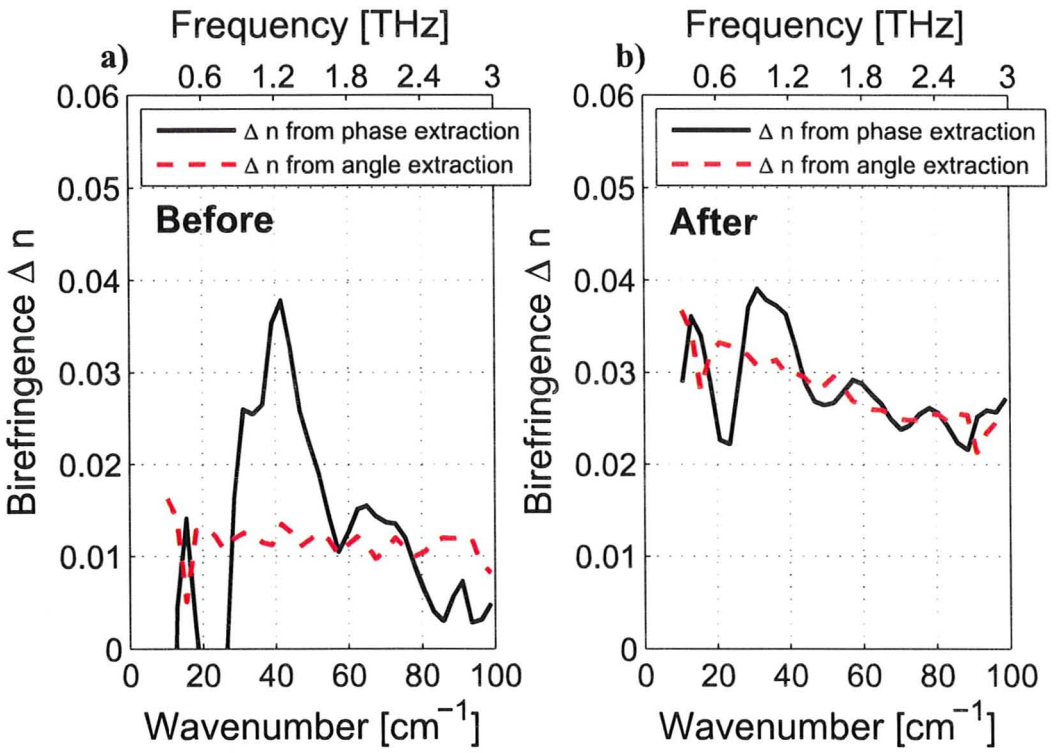

Figure 4.3: Birefringence estimates obtained using both the classical phase extraction method and the polarimetric angle extraction methods. Due to the sample being 0.32 mm thick before heat application and 0.66 mm thick after, the periodicity of the Fabry-Perot reflections is quite different between the two measurements.

In both the before and after cases, the polarimetric analysis method provides birefringence estimates that have significantly less variability than the classical phase extraction method. While the Fabry-Perot reflections are still present in the polarimetric data, their influence is significantly reduced as the absolute magnitude is less sensitive to the introduced variability than the phase. Despite the improvement in the polarimetric birefringence estimate, the "after" estimate still suffers from a clearly systematic decrease with frequency. In the estimates given in table 4.1 a clear linear dichroism was present at 2 THz, and the analysis of the entire dichroism spectrum in figure 4.4a, shows this effect is present across the entire bandwidth.

The estimates shown figure 4.4a are particularly noisy as the material sample is quite thin. So while the absorption coefficient is quite high, upwards of 25 cm^{-1} at 2 THz, the actual measured absorption is quite small. Estimating the absorption coefficient also requires *a priori* knowledge of the real part of the index of refraction, as per equation 4.2, to estimate the Fresnel reflection and transmission coefficients at the interfaces. The classical method for analysis uses the estimate of n obtained from the phase to estimate α, thus the Fabry-Perot reflections and their systematic error are introduced through two mechanisms in the estimate.

One key complication of dichroism is that the simple method for polarimetric analysis yields biased estimates of the birefringence. This bias can be corrected by compensating for the effect of the dichroism and including that effect within the polarimetric analysis of the absorption coefficient. The linear dichroism exhibited in figure 4.4a, despite being quite noisy, can be approximated as being stepwise linear with frequency, with negligible dichroism below 0.7 THz . Using this approximation, the slope of the linear dichroism curve is 4 cm^{-1}/THz with a dichroism of 0 cm^{-1} from 0.0 to 0.7 THz. This approximation for the linear dichroism can then be used as a correction factor for the original measurements of $|\tilde{E}_{samp}|$.

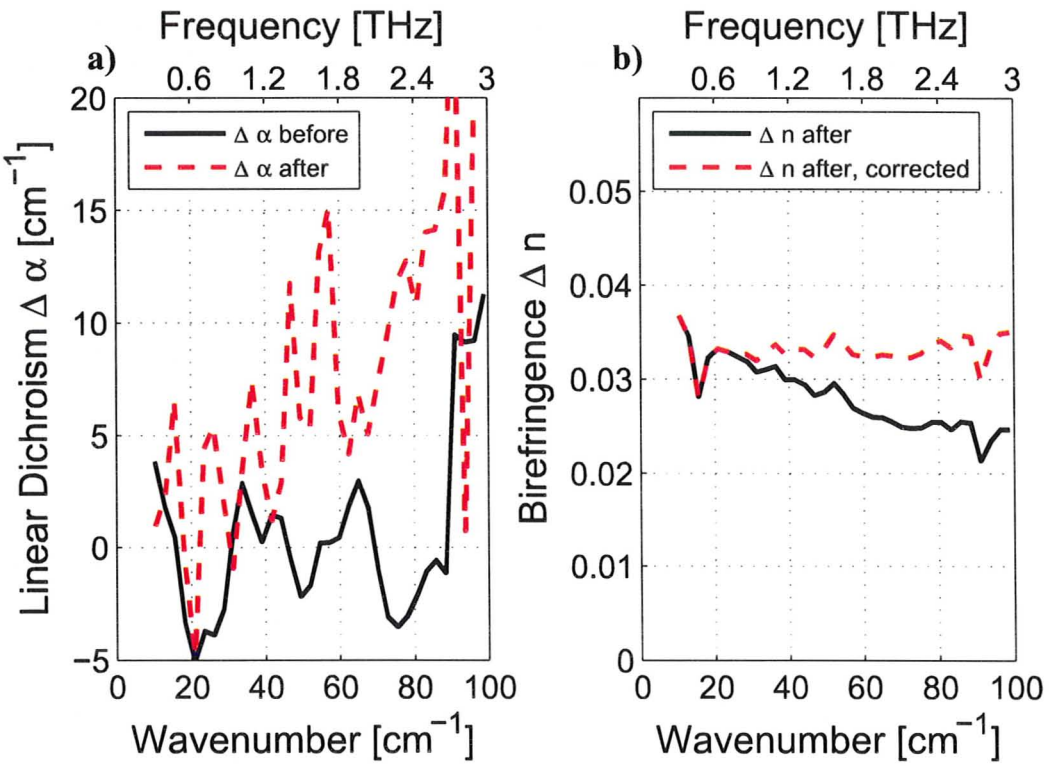

Figure 4.4: Linear dichroism is present in the heat-shrink sample after heating and plays a role in adding bias to the polarimetric estimate. a) Using the classical analysis method the difference in absorption coefficient before and after application of heat was determined. While both estimates are quite noisy, the dichroism is only apparent after heat is applied. b) Assuming the linear dichroism is proportional to frequency, a correction factor for the dichroism was applied to the polarimetric estimate method resulting in the estimate shown.

Using this correction factor yields the corrected birefringence measurement in figure 4.4b. The corrected graph fits with numerous other experiments conducted within the course of this work that show a near constant birefringence across the experimental bandwidth for most of the polymers investigated.

These experimental results should be examined in the scientific framework for heat-shrink polymers that was earlier discussed. After the initial application of heat to melt the crystalline portions of the polymer, the cross-linked chains in the desired direction of shrinkage have been distorted. The net directionality of the cross-linking in this state may have occurred due to the initial method for cross-linking, or may simply be a result of the mechanical stretching. After application of heat, the chains are pulled back into shape to reduce the potential energy of the cross-linked chains. As the birefringence increases, the relaxed state must have a net higher percentage of chains oriented in the same direction.

4.2.2 Mechanically Induced Birefringent Variability

One of the materials commonly used in constructing equipment for THz-TDS experiments is polyethylene, or PE. Polyethylene is the most widely used plastic, most notably used in plastic shopping and garbage bags, and is available in numerous different weights. These weights correspond to different densities and branching structures possible along the polymer chain (Peterlin, 1971). Within the PRL, black coloured high density polyethylene (HDPE), sheets are used to block the 800 nm pump radiation within the THz beam path, while causing only a minor (7%) reduction the THz field intensity.

Sample Preparation

The HDPE sheets have a nominal thickness of between 50-60 μm. As the material is opaque to optical probes, measuring the thickness in this regime is somewhat complicated. In order to verify the thickness, multiple THz-TDS measurements were taken and the estimates for introduced optical path length increase was averaged. The nominal value of n was then determined by stacking 15 layers, obtaining a thickness significant enough to measure with

a micrometer, and then conducting another THz-TDS measurement. The index information obtained from the stacked pile was then used to extract the thickness, d, from the individual sheet measurements based on the optical path length, as $OPL = nd$.

Using the aforementioned method, the initial thickness of the sheets was determined to be $54 \pm 6\mu$m. In order to induce birefringence in the sheets, a sufficient load must be applied to result in deformation. In this case, the desire is to create a measurable plastic deformation. Thus a load must be applied that exceeds the yield strength such that plastic, rather than elastic, deformation occurs.

The yield strength in various HDPE samples is known to range between 26-30 MPa (Turcsnyi *et al.*, 1987). In order to estimate the approximate load needed to cause plastic deformation, the approximate size of the cut sheets was decided to be 4 cm. Thus the cross sectional area of the 4 cm by 54 μm sheet would be approximately $2 \times 10^{-6}\text{m}^2$. Thus the required load would be 60 N, or about 6 kg. Using a clamping apparatus, loads of 6 kg were spread across the width of a cut sheet of the HDPE, plastic deformation was noticeable within several seconds. The deformation rate accelerated rapidly resulting in fracture if the load was left applied for more than 10 seconds. An optimized maximum deformation length of 250% of the original length of was determined through several trials, and a block used to prevent the load from deformation from exceeding this limit.

More than twenty samples of stretched HDPE were created. Each sample was measured using polarimetric THz-TDS before the load was applied. In some cases, additional heat from a heat gun was applied to reduce the required load for plastic deformation. The sample described in the following data sets demonstrated the largest induced birefringence amongst all the samples, and was created using a 3 kg load with heat applied. As the entire stretched sheet was typically 4 cm x 10 cm, a 1.5 cm x 1.5 cm portion of the sample was cut to be used in the measurement. The sample creation process is shown in figure 4.5.

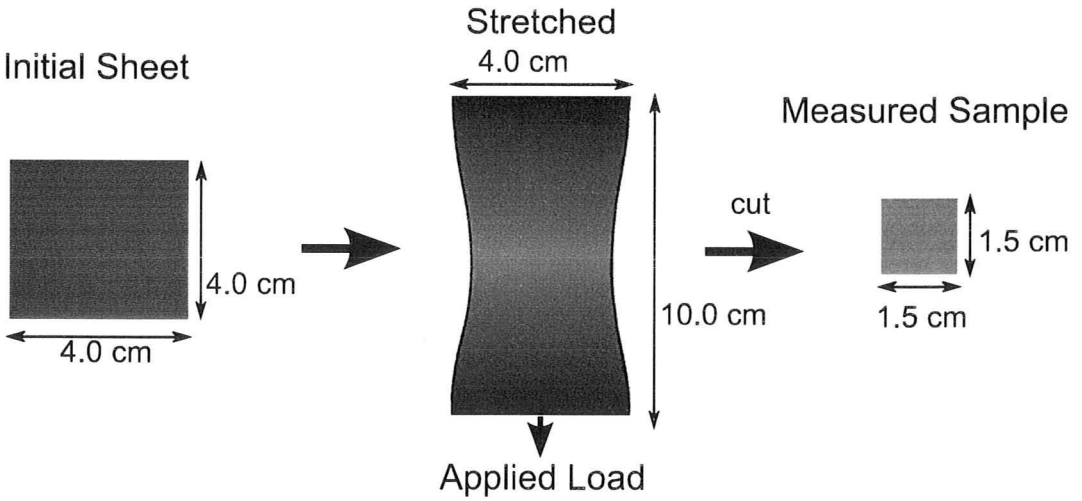

Figure 4.5: Sample preparation steps for the HDPE sheet. The initial sheet was cut from a roll of HDPE, with the edges parallel to the edges of the roll. This initial sample was measured using THz-TDS. The sample was then stretched using a load clamped to the bottom of the sheet. After the sample was stretched, a noticeable change in opacity occurred. The stretched sample was cut from the center of the large piece of stretched material.

Data Analysis and Results

The measurement and analysis for the HDPE sheets is very similar to the process followed for the heat-shrink sample. The key complication in the HDPE measurements is that the thickness can not be measured independently using a micrometer. Instead, the THz-TDS measurements themselves must be used to determine both the thickness and index of refraction. For the initial sample, the thickness determination was done using multiple sheets to first determine n. With the stretched sample, the thickness has clearly decreased.

The initial measurements of the HDPE sheets are shown in figure 4.6. An inspection of the initial sheet data in figure 4.6 a shows that a slight birefringence must be present, as the angle of the THz field varies as the sample is rotated. The peak of the angle variation occurs at a sample angle of 72° , indicating that the principal axes are located at sample angles of 27° and 117° . As the sample was mounted such that 0° corresponded to the THz field being parallel to the vertical edge of the HDPE sheet, these locations

of the principal axes indicate that the sheet has built-in strain in a diagonal direction.

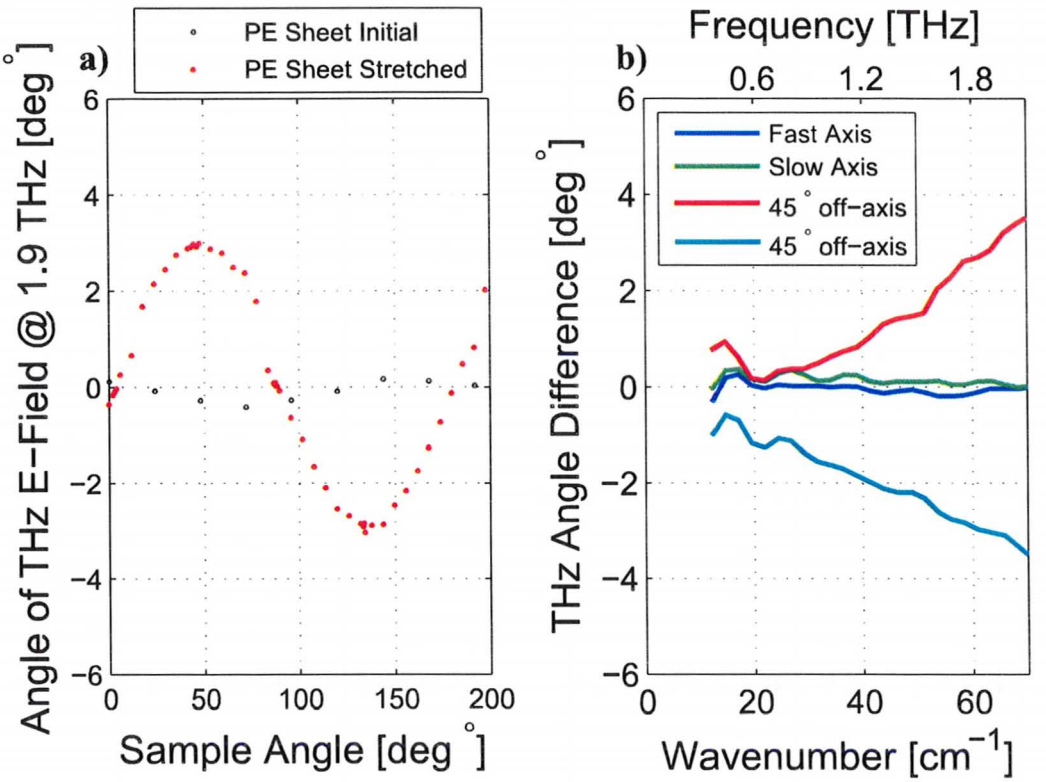

Figure 4.6: Steps in analysis of the stretched polyethylene sheet. a) Initially a small birefringence of $\Delta n < 0.01$ is present. The principal axes do not line up with the edges of the sheet, rather they are approximately 27° off the physical axes. After stretching the sheet along the physical axes, the principal axes lie along the physical axes. b) Compared the heat-shrink, the change in polarization state as a result of the polyethylene film is significantly less due as the thickness of the material is an order of magnitude less.

The principal axes in the stretched sheet are parallel to the physical axes of the sheet. This is expected as the principal axes should follow the orientation of the strain applied to the sheet. The measurements along the slow axis in figure 4.6b indicate some systematic flaws in the experiment as the angle difference is non-zero for frequencies below 1.5 THz. This flaw may be due to a non-uniform distribution of deformation within the stretched sheet. While care was

taken to obtain a sample that visually appeared uniform, without microscopic analysis of the sample over a wide area, this is hard to guarantee. As previously discussed in Chapter 3, the size of the THz focus is frequency dependent, and so lower frequencies are more susceptible to non-uniform materials. The slow axis measurement in figure 4.6b clearly less systematic error at higher frequencies, which also supports the hypothesis of non-uniformity as a cause of this error.

As with the heat-shrink measurement, both the classical phase extraction method of analysis and the polarimetric method of analysis were used to estimate the birefringence in the sample, with the results shown in figure 4.7. In order to extract the birefringence measurement after the material has been stretched, the thickness must first be determined. The method used to determine the initial thickness and index cannot be used as the sample is not homogeneous enough to get sufficient stacked pieces. Instead, an iterative process of estimating the index of refraction and thickness is used until a converged estimate of the thickness is achieved. The initial measurement of the index of refraction, n=2.09, was used to start the iterative procedure. To increase the accuracy of the estimate, the procedure was applied to numerous estimates with the sample at different rotation angles. These estimates formed a distribution, which was then averaged.

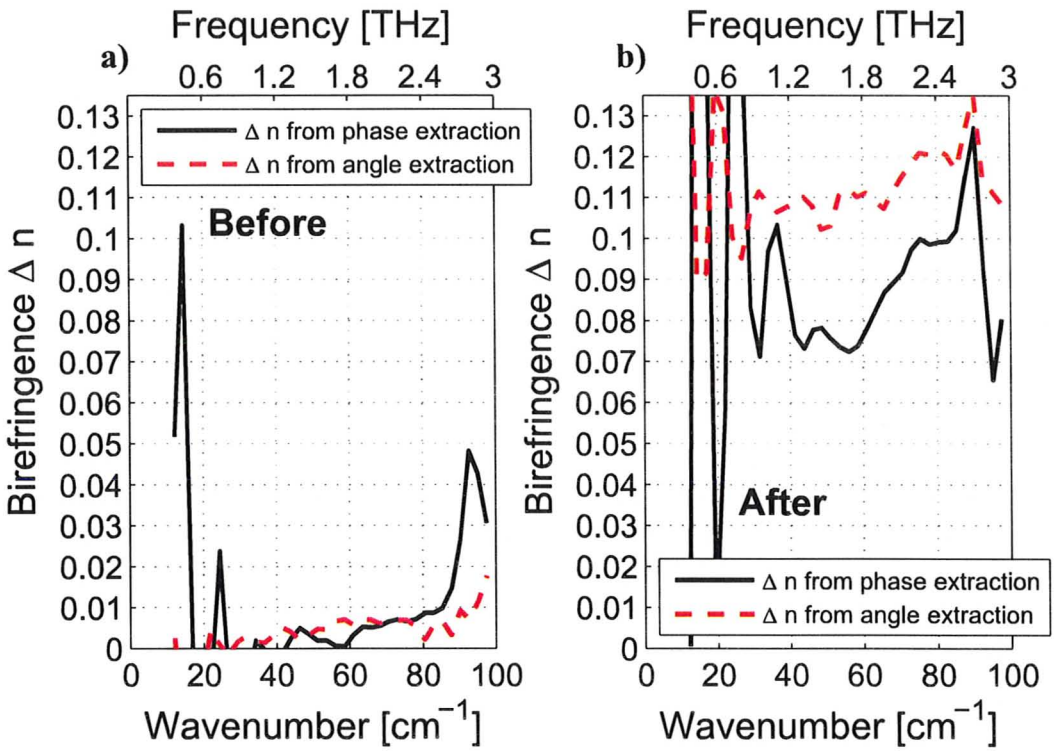

Figure 4.7: Birefringence estimates obtained using both the classical phase extraction method and the polarimetric angle extraction methods. Due to the sample being only 54 μm thick before being stretched and 24 μm thick after, the Fabry-Perot reflection effect is quite pronounced. a) The birefringence is small before the HDPE sheet is stretched. b) After being stretched, the birefringence was amongst the largest measured in this work.

The measurements of birefringence in the HDPE sheet demonstrate the utility of of the polarimetric method. The classical method fails completely on such a thin sample due to the Fabry-Perot reflections and phase instability; however, the polarimetric method still provides a useful estimate. In the polarimetric birefringence estimate, a bias, as in the uncorrected heat-shrink measurements, appears to be present at higher frequencies. In this case, the cause does not appear to be anisotropic absorption, as no linear dichroism was detectable.

The change in refractive indices of the HDPE sheet before and after stretching are summarized in table 4.2. Unlike the heat-shrink tubing, mechanical

stretching of the HDPE results in an increase in the index of refraction along one principal axis, and a decrease in the other. This difference could simply be due to the relative difference in the change in material density. In the physical measurements of the heat-shrink, figure 4.1, the change in dimensions showed the material must have had a net increase in density after heat was applied. This increase in density would be expected to yield a higher index of refraction and a higher absorption coefficient. In the case of the HDPE, the average density was not determined, although it could be estimated through sensitive mass measurements.

Table 4.2: Index of refraction estimates extracted using the classical analysis method for the HDPE sheets, before and after being stretched. The principal axes used were the axes after the stretching. All estimates are for 2.0 THz (67 cm^{-1}). Reliable estimates of the absorption coefficient could not be obtained, as material does not cause sufficient absorption.

Axis	thickness before [μm]	thickness after [μm]	n_{before}	n_{after}	change
slow	55	24	2.095	2.125	+0.030
fast	55	24	2.090	2.035	-0.055

Infrared measurements of polymer systems with induced birefringence have been a staple of polymer science (Peterlin, 1971);however, the use of THz-TDS has been quite limited. Polarimetric THz-TDS measurements allow the simultaneous determination of the thickness of the material, through the optical delay change, and the anisotropic materials properties. In materials systems, such as the HDPE sheets, where the thickness is otherwise troublesome to determine, THz-TDS provides a significant advantage over infrared techniques.

The region of the spectrum where THz-TDS operates is also a benefit over infrared polymer measurements. Absorption at the low end of the THz regime, below 1 THz, is typically quite low, while the mid-range of the THz regime may contain interesting features, such as the 2.5 THz phonon mode in polyethylene. THz-TDS allows the probing of such phonon modes under varying experimental and materials conditions, which could prove interesting.

4.3 Crystalline Lanthanum Aluminate

Crystalline materials can be intrinsically birefringent depending on the presence or lack of symmetry in the spacing of atoms within the crystalline lattice. With the exception of cubic crystals, all other crystalline materials are intrinsically birefringent (Fowles, 1989). While crystalline birefringence is not a key component of this thesis, one example of this birefringence demonstrated the utility of THz-TDS polarimetry.

Within the thin film growth facilities at McMaster University, numerous different substrates are used for growth. When growing any epitaxial thin film, lattice matching between the substrate surface layer and the thin film layer is extremely important. A large lattice mismatch results in film growth that with numerous dislocations, built-in strain and other defects (Ohring, 2002). In order to grow a wide-variety of exotic films, a wide variety of substrates must be employed. One particular substrate used in the growth of superconducting YCBO films is lanthanum aluminate, as it is lattice matched to within 2% (McDaniel and Hsu, 1996).

The crystalline structure of lanthanum aluminate is a perovskite which is uniaxial at room temperature (McDaniel and Hsu, 1996). The material is prone to twinning, with the twins easily distinguishable optically through a microscope.

Sample Preparation

The samples of lanthantum aluminate were obtained from a cleaved wafer at the thin film facilities in the Brockhouse Institute of Materials Research. The sample was trapezoidal with a total area of approximately 1 cm^2 and the thickness was measured to be 530 μm with mechanical calipers. The sample was mounted on a mechanical rotation stage behind a 5 mm diameter aperture. Rather long scans of 768 points at a sample rate of 40 fs were taken. The longer scans were necessary as the high index of lanthanum aluminate results in quite a significant optical delay even from a relatively thin sample.

Data Analysis and Results

These measurements were taken almost a year before all other measurements presented in this thesis and the system had significantly lower SNR and significantly more phase noise. As a result, a significant amount of data tuning was required to obtain the index of refraction estimates. The increased phase noise results in numerous 2π offsets in the extracted phase of the Fourier transform of the each scan as the wrong branch cut is selected when unwrapping. In order to correct this limitation of the standard unwrap procedure, appropriate multiples of 2π were manually added to the required phase values in order to present the index estimate of figure 4.8. Similar correction was not required in the other birefringent samples measured with the improved THz-TDS experimental setup.

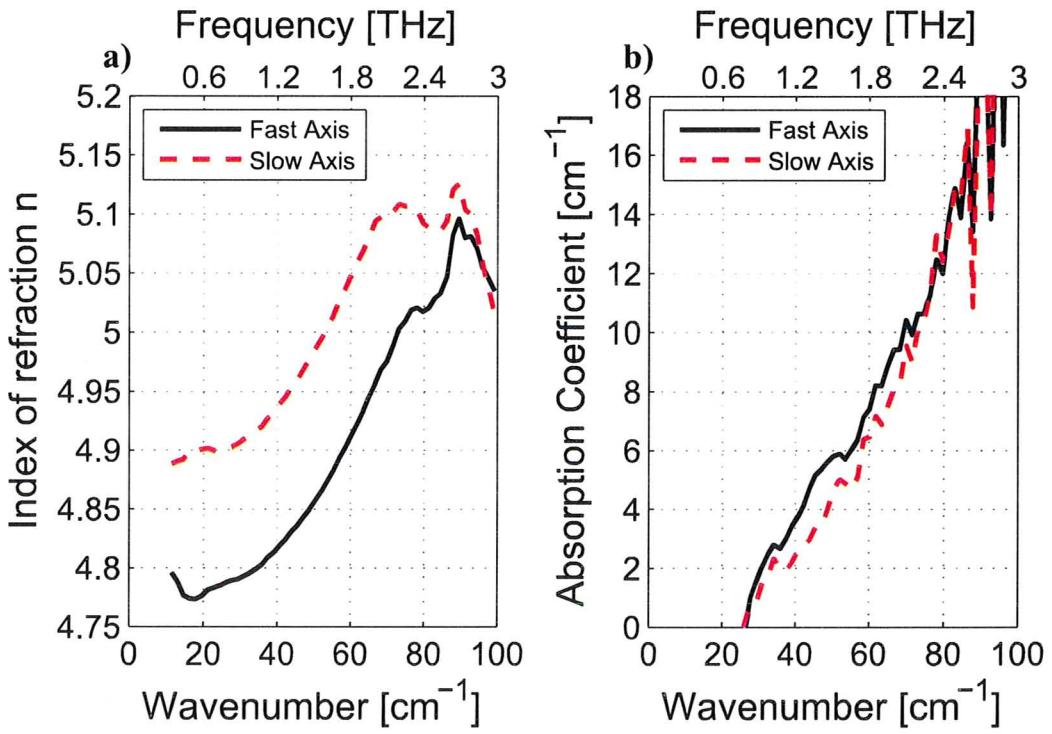

Figure 4.8: Optical properties along both the principal axes of the lanthanum aluminate sample obtained by the phase extraction method for THz-TDS data analysis. a) The index of refraction increases monotonically, as does the b) absorption coefficient.

The measurements of figure 4.8 show that the lanthanum aluminumate sample is strongly birefringent with a slight dichroism as well. Unlike many the of polymer samples, the index of refraction varies significantly across the THz bandwidth. The index of refraction is also quite high, at approximately 5, which yields much larger Fresnel reflections at the sample interface and thus a stronger Fabry-Perot etalon effect. The net electric field transmission through the sample, assuming negligible absorption, is at best 56% due the Fresnel losses.

Using both the phase extraction and polarimetric analysis method, the birefringence of the lanthanum aluminate was measured and is shown in figure 4.9a. The birefringence actually shows several interesting features. While the initial bump in the birefringence at 500 GHz may simply be due to Fabry-Perot reflections, the gentle upwards slope between 750 GHz and 2 THz cannot.

The significant drop in the birefringence after 2 THz is also quite interesting. One possible explanation for this behaviour is the twins present within the crystal sample. While care was taken to measure through an optically homogeneous region, microscopic verification of the homogeneity was not performed on this sample. As the beam waist varies significantly with frequency, it is possible that the higher frequency measurements are measuring the region of a single twin, where as the lower frequency measurements are across several twins.

Evidence for the possibility of various between twins could be obtained by the rotation of the sample through a serious of intermediate angles, and translation of the sample in the plane orthogonal to the propagation of THz field. The combination of these measurements would allow a more complete understanding of the physical phenomena at play.

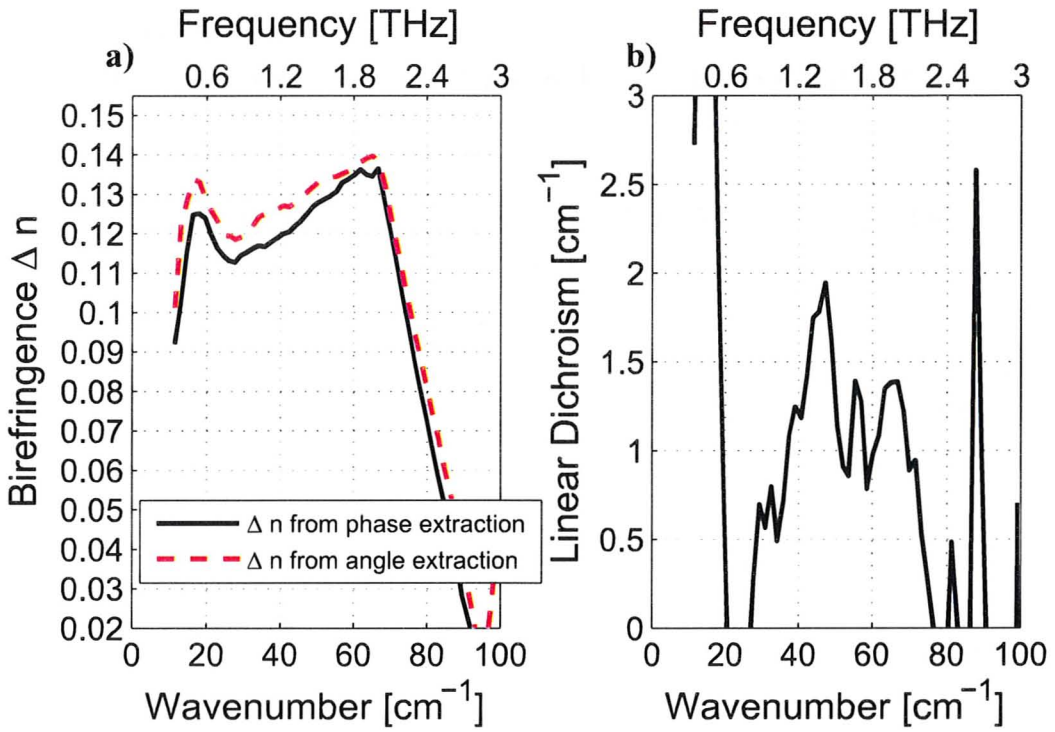

Figure 4.9: Anisotropic optical properties of the lanthanum aluminate sample. a) Using both phase-extraction and polarimetric data analysis, the birefringence was extracted. Unlike polymer samples, the birefringence decreases above 2 THz. b) The linear dichroism is small, but clearly present between 0.75 and 2.0 THz. The dichroism measurement is relatively noisy due to the small absorption and relatively large Fresnel losses.

The linear dichroism estimates, shown in figure 4.9b, also support the measured changes in birefringence as physical manifestations and not experimental errors. Through the Kramers-Kronig relation, a change in the birefringence of the material must be accompanied by a change in the dichroism of the material. In the case of the two regions of rapid change in birefringence, (below 0.6 THz and above 2.0 THz) corresponding changes in the dichroism are present.

As a final note to this discussion on lanthanum aluminate, previous measurements have not noted birefringence at THz frequencies (Grischkowsky *et al.*, 1990). Indeed, significant birefringence makes a material particularly unappealing as a substrate for measurement of thin films. Another closely

related material, lanthanum gallate, has been noted as having significant birefringence at THz frequencies, although estimates of the values were not published (Grischkowsky *et al.*, 1990). Lanthanum gallate has similar optical features and n and α profiles at THz frequencies when compared to lanthanum aluminate, so it is possible, although unlikely, that the sample received was incorrectly labelled. If the sample were still available, it would be prudent to conduct further studies to ascertain is chemical composition.

4.4 Conclusion

Birefringence occurs widely in materials and can be due to intrinsic materials properties or due to the processing the material has received. While classical THz-TDS analysis is generally able to only examine birefringent samples at least hundreds of microns thick, polarimetric THz-TDS allows examination of much thinner samples. The ability to study thin samples, especially those which may be opaque at infrared frequencies, is an additional measurement tool that can be used in the study of materials. The examination of various polymer systems may be aided by the use of THz-TDS in addition to the more typical analysis using IR spectroscopy and x-ray measurements.

Chapter 5

Design of an Achromatic THz Waveplate

The broadband nature of THz-TDS systems presents a challenge for designing optical components. Optical pulses in the visible and telecommunications wavelength regimes typically have bandwidths in the tens of nanometers, corresponding to a quality factor, Q, of greater than 10. However, THz pulses frequently have a Q below one underscoring the ultrabroadband nature of these pulses.

Through the use of various materials, broadband lenses and polarizers have been created for THz frequencies. However, one key missing component of the optical toolset are broadband waveplates. In 2006, Masson *et al.* fabricated a multilayer THz achromatic waveplate from birefringent quartz using a stacked structure as shown in figure 5.1. While their waveplate performed well, it required the use of custom fabricated quartz layers and was over 3 cm thick (Masson and Gallot, 2006).

The goal of this chapter is to show that polymer systems can be used to create an achromatic waveplate of similar efficiency to the quartz achromatic waveplate while only using layers cut from a single sheet. This task is complicated by non-negligible linear dichroism in the samples which requires effective modelling to enable design of the waveplates.

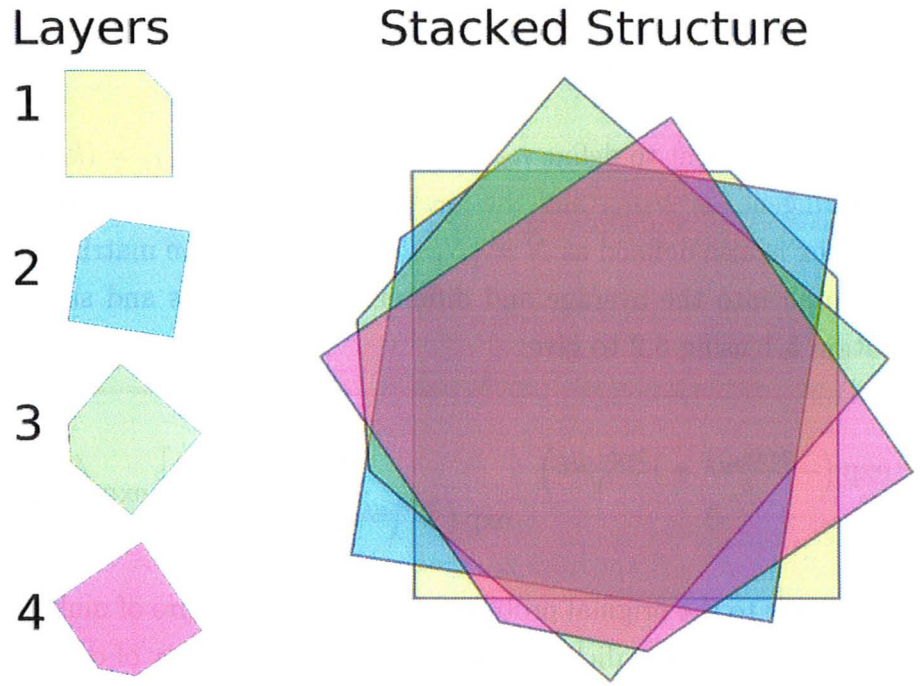

Figure 5.1: A stacked waveplate is formed by mechanically attaching several layers of birefringent material oriented such that the output polarization state is technologically useful over a broad range of frequencies, rather than in just a narrow band.

5.1 Mathematical Modelling and Optimization

The following treatment of EM wave propagation in anisotropic media follows closely the work in (Naydenova *et al.*, 1997) and the description given in chapter 3 for polarimetric analysis. In general, the Jones matrix, $\tilde{\mathbf{J}}$ for propagation of an EM wave with free-space wavelength λ through a linear medium of thickness d can be written in terms of the wave propagation matrix $\tilde{\mathbf{K}}$:

$$\tilde{\mathbf{J}} = \exp\left(-i\tilde{\mathbf{K}}d\right). \tag{5.1}$$

In order to treat the general case with linear dichroism and linear birefringence two complex indices of refraction are required: $\tilde{N}_1 = n_1 + ik_1$, $\tilde{N}_2 = n_2 + ik_2$. The $\tilde{\mathbf{K}}$ can then be expressed in terms of these indices:

$$\tilde{\mathbf{K}} = \frac{2\pi d}{\lambda}\begin{bmatrix} N_1 & 0 \\ 0 & N_2 \end{bmatrix}. \tag{5.2}$$

It is then convenient to define $n_{diff} = (n_1 - n_2)/2$ and $k_{diff} = (k_1 - k_2)/2$, so the birefringence is $2n_{diff}$ and the linear dichorism is $2k_{diff}$. The average complex index is also defined as $\bar{N} = (\tilde{N}_1 + \tilde{N}_2)/2$. The wave matrix can then be decomposed into the average and difference components and substituted into equation 5.1 using 5.2 to give:

$$\tilde{\mathbf{J}} = \begin{bmatrix} \exp\left(-\frac{2\pi dk_{diff}}{\lambda} + i\frac{2\pi dn_{diff}}{\lambda}\right) & 0 \\ 0 & \exp\left(\frac{2\pi dk_{diff}}{\lambda} - i\frac{2\pi dn_{diff}}{\lambda}\right) \end{bmatrix} \exp\left(i\frac{2\pi d}{\lambda}\bar{N}\right). \tag{5.3}$$

Turning back to the original problem of a stacked structure of multiple layers of birefringent, linearly dichroic material, the Jones matrix of equation 5.3 can be combined with the general rotation matrix operator, $R(\theta)$ to determine the effective Jones matrix for the entire stack:

$$J_{tot} = \begin{bmatrix} \tilde{J}_1 & \tilde{J}_2 \\ -\tilde{J}_2 & \tilde{J}_1{}^* \end{bmatrix} = \prod_{j=1}^{M} R(-\theta_j) J_j R(\theta_j), \text{ where:} \tag{5.4}$$

$$R(\theta) = \begin{bmatrix} \cos\theta & \sin\theta \\ -\sin\theta & \cos\theta \end{bmatrix}. \tag{5.5}$$

The key parameter of interest for performance of a waveplate is the dephasing, $\Delta\phi$ between polarization components, mathematically this can be derived from the Jones matrix of equation 5.4 as:

$$\Delta\phi = 2\tan^{-1}\sqrt{\frac{\Im[\tilde{J}_1]^2 + \Im[\tilde{J}_2]^2}{\Re[\tilde{J}_1]^2 + \Re[\tilde{J}_2]^2}}. \tag{5.6}$$

The form of equation 5.6 should make it clear that the overall average material term of $\exp\left(i2\pi d\bar{N}/\lambda\right)$ in equation 5.3 can be safely ignored when calculating the dephasing.

This preceding derivation gives the mathematical formality necessary to

design waveplates with arbitrary dephasing responses. The initial case of interest is a waveplate stack compromised of M layers of known thickness, d and complex indices of refraction, $\tilde{N}_1$ and $\tilde{N}_2$, with each plate orientation at some angle θ_i around the optical axis. This case occurs when numerous pieces of a material are cut from a single homogeneous sheet or slab of material. The product of 5.4 then yields a matrix product with M unknown angles θ_i.

Determining these angles is a case of non-linear parameter estimation and numerical software is the best approach to solving this problem. An introduction to parametric estimation methods is given in Appendix A and the following discussion adopts the formalism described in Appendix A.

Parameter estimation problems are normally restated in terms of a cost function, $\chi^2(\theta)$, with parameters θ. For a given output data set y with estimated variance, σ^2, and given a model, λ, which depends on the input variable x and estimated parameter set θ_g , the χ^2 function for a least squares fit is given by (Tarantola, 2004):

$$\chi^2(\theta) = \sum_{i=1}^{M} \frac{(y_i - \lambda(x_i; \theta_g))^2}{\sigma_i^2}. \tag{5.7}$$

The role of the optimization software is to take an initial parameter guess, calculate the χ^2, and then adjust the parameters to attempt to reduce the value of χ^2. This process is repeated until some termination condition, typically either a maximum number of iterations or minimum change in parameter values, is reached.

To solve the design problem of the stacked waveplate, the desired frequency response of $\Delta\phi$ is given as y and λ is the determined from the Jones matrix using equation 5.6. Since the design test case is for a quarter wave plate between 1 THz and 2 THz, y is set to $\pi/2$ for this frequency range and is unconstrained for all other frequencies. For any given material parameters, we now have a general way to design a waveplate with arbitrary dephasing response.

5.2 Material Selection

Two classes of materials are obvious candidates for use in a THz waveplate. Birefringent single crystals, such as quartz (SiO_2) and lanthanum aluminate ($LaAlO_3$), are readily available, but are typically costly and also tend to have moderate indices of refraction, resulting in higher Fresnel losses. The other obvious candidates are polymer systems, several of which are quite transparent at THz frequencies. Birefringence in polymer systems occurs during the fabrication process, as the partially molten material is put under significant strain resulting in a net orientation of the polymer chains (Tagaya *et al.*, 2001). This birefringence can readily be observed at optical frequencies in everyday items, such as overhead transparencies. The amount of birefringence is dependent on the fabrication process and can be increased or decreased through the addition of dopant molecules (Tagaya *et al.*, 2001).

Among polymer systems, TPX® (polymethylpentane), Tsurupica, HDPE and Teflon® are commonly used for THz components. TPX is commonly used for medical applications as its glass transition temperature is above that of typical autoclave temperatures. It is readily available, but typically only in large quantities. Tsurupica, being custom engineered, is only available in very limited quantities and is rather expensive. High Density Polyethylene (HDPE) is one of the most widely used polymers; it can be found in a variety of thicknesses and grades to suit just about any purpose. The glass transition of HDPE is just above 100°C, so it is not particularly well suited for heating applications. Teflon® films and sheets find wide use as dielectrics in various electrical components due their high breakdown voltage and glass transition temperature. A final option is polypropelene, which has similar THz optical properties as Teflon® and HDPE, but has yet to commonly used for THz components.

The key properties of the aforementioned polymers are summarized in table 5.1. If Tsurupica and TPX are excluded from the analysis, then the common polymers HDPE, Teflon® and polypropelene are all quite similar. HDPE is the least preferable of the three materials, as it has a higher index of refraction and the lowest glass transition temperature. Teflon® and polypropelene appear

to be very similar; however, it turns out that thin polypropelene sheets are not commonly manufactured. Teflon® sheets, on the other hand, are readily available due to its common use as a dielectric and as an anti-stick work surface.

Table 5.1: Properties of selected polymer materials transparent at THz frequencies.

Polymer	Index n	α at 2 THz [cm^{-1}]	Visible Properties
HDPE	1.54	2.5	Opaque
Polypropelene	1.49	3.5	Opaque
Teflon®	1.38	2.5	Opaque
TPX®	1.46	1.1	Polished to transparent
Tsurupica	1.52	1.0	Polished to transparent

Through the use of the polarization sensitive THz system described in Chapter 3, dozens of samples can be quickly inspected for birefringence. The sample is mounted at an arbitrary angle and then the principal component of the electric field is measured, allowing determination of the location of the THz signal. The detector system is then rotated so that it is sensitive to the perpendicular field polarization and another quick THz scan is taken. If the material is isotropic, the second scan should yield an extremely low power determined by the extinction ratio of the detector system. However, even a small birefringence of $\Delta n = 0.001$ for a sample a few mm thick will yield a significant power increase in the second scan relative to an isotropic sample. If no increase is noted, the sample must then be rotated, typically by 45° around the optical axis, and another scan obtained. This second scan is necessary in case the first scan happened to be along a principal axis of the material, which would result in no net rotation of the electric even if it were anisotropic.

If an increase in the detected secondary polarization signal is noted, the material likely has anisotropy. These samples can then be marked for more detailed investigation. Through a mixture of polarimetry and direct measurement along the principal axes, the anisotropic material parameters can be gleaned from the data and independently verified. The remaining discussion focusses on a particular set of Teflon® sheets obtained from P&A Plastics in

Hamilton, Ontario. These sheets are 1.70 mm thick and have a significant birefringence.

Using the classical method for extraction of the anisotropic material parameters, the parameters for the sheet were extracted and are shown in figure 5.2. The birefringence is 0.010 across the entire THz bandwidth and the dichroism varies with frequency. As with the heat-shrink tubing sample of Chapter 4, the dichroism is approximated by a piecewise linear function for the purposes of modelling. The birefringence is assumed to be constant across the bandwidth.

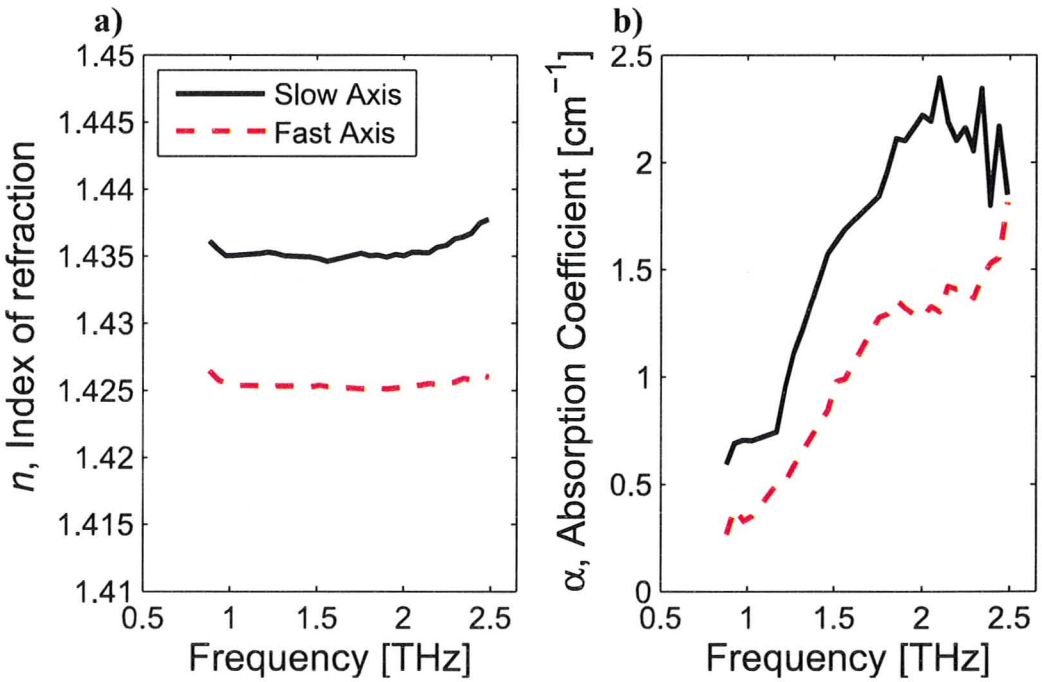

Figure 5.2: a) Index of refraction and b) absorption coefficient estimates for the 1.70 mm thick Teflon® sheet. The estimates have been extracted using the classical analysis method.

5.3 Mechanical Construction

In order to construct the achromatic waveplate, numerous layers must be cut from a section of material and properly oriented to within a small margin of error. One potential worry when attaching multiple layers of material is that

resulting air gaps between the layers must result in significant interface Fresnel reflections. These reflections would be apparent in the THz spectrum due to the presence of Fabry-Perot type distortions as discussed in Appendix B.

In several initial measurements, the individual layers were stacked together and their edges were attached with aluminum foil tape. THz-TDS measurements of these stacks showed Fabry-Perot type distortions only with the periodicity of the entire stack, and not individual layers. Thus this stacking method was sufficient for waveplate construction and there was no need to find a suitable filler or glue for use between the layers.

To test the possibility of creating an achromatic waveplate, a program was written in MATLAB® to implement the process described in section 5.2. Achromatic plates with varying number of layers were modelled and constructed. The best performing combination of these plates was constructed from 11 layers with the orientations described in table 5.2. It should be noted that the absolute reference for the angle of the layers does not matter, rather then key importance is the relative angle between each layer. The template used to cut these layers from a sheet of Teflon is shown in figure 5.3.

Table 5.2: List of layers and relative orientation angles for TTAQ 006

Layer	Angle [°]	Layer	Angle [°]	Layer	Angle [°]
01	270	05	20	09	0
02	67	06	20	10	181
03	218	07	14	11	185
04	22	08	5		

To aid in alignment of each layer, a guide similar to the primary and secondary flats used on semiconductor wafers was cut into each layer. With knowledge of the top side of the layer, via a marking and the cut corner, the layers can be oriented to within less than a degree rapidly.

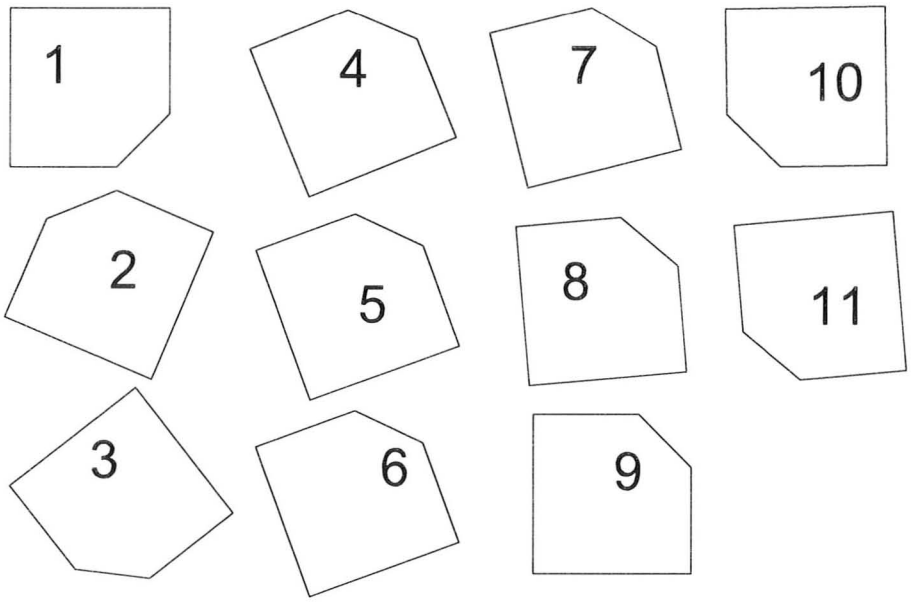

Figure 5.3: Orientation of various layers of the test waveplate, TTAQ 006, as cut from a uniform sheet of material. After cutting the layers are placed in order and aligned by using the angled edge to form the completed waveplate.

5.4 Results

The performance of the waveplate can be quantified in numerous ways. For our purposes, the primary use of the waveplate is to create right and left circularly polarized THz fields and so the most appropriate metric is ellipticity of the output polarization. Using the polarimetric THz-TDS apparatus, several scans were taken to determine the fast and slow axes of the waveplate, along with the angle for optimal output of circularly polarized light. As expected, optimal circular polarization was achieved at $\pm 45°$ from the axes.

Typical results of the scans are shown in figure 5.4. The trace in figure 5.4a is a polar plot of the individual electric field components. For a continuous source that is perfectly circularly polarized, this plot should show a perfect circle. However, for a pulsed source, obtaining a perfect circle is impossible as the amplitude varies, thus a pulse with a ellipticity of ± 1 would be a spiral out and then a spiral back down to zero amplitude, similar to what is shown in the figure. The plots in figure 5.4a also demonstrate that the waveplate is

zero order as a higher order waveplate would result in a polar plot that was nowhere near circular at any point. The condition of zero-order is important for pulsed operation as it is desirable to maintain the short THz pulse.

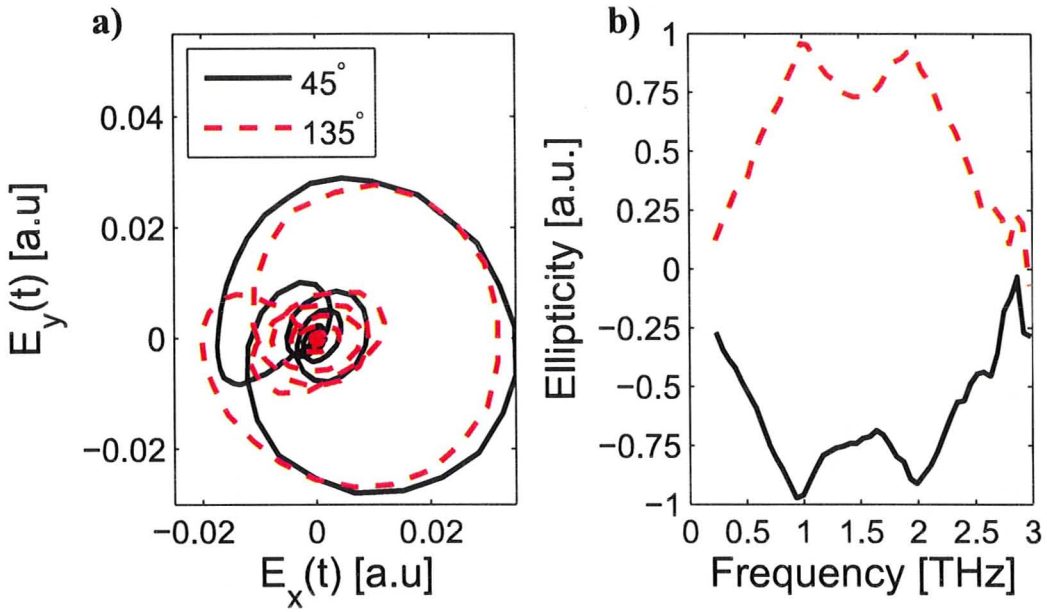

Figure 5.4: Measurements of the performance of the test waveplate. a) Polar plot of the time domain traces of the individual electric field components. b) Ellipticity estimate, an ellipticity of 1 indicates a perfect right circular polarization state and -1 indicates a left circular polarization state.

The second metric in figure 5.4b is the ellipticity which is the ratio of the minor to major axes of the polarization ellipse. For a perfect circular polarization state, the ellipticity should be ± 1. Measurements indicate the achromatic waveplate has an ellipticity which exceeds 0.75 over a bandwidth of 0.75 to 2.25 THz. This bandwidth corresponds to the bandwidth of the THz-TDS apparatus.

Another key performance measure for the waveplate is the total transmitted amplitude. Due to both Fresnel reflections and absorption within the polymer material, the electric field intensity is significantly reduced. At 1.87 cm thick, and with an average absorption coefficient of 2.0 cm^{-1} at 2 THz, the expected transmitted intensity is only 0.15 at 2 THz. While the performance shown in

figure 5.5a does indicate that the waveplate performs better than the average absorption coefficient would indicate, the significant amount of absorption degrades its usefulness.

As a secondary demonstration that the waveplate is in fact zero order, the individual components of the electric field are shown on the same axis in figure 5.5. Both pulses clearly maintain the shape a THz pulse. The delay of approximately 25 ps, seen in the time axis, is due to the optical thickness of the material.

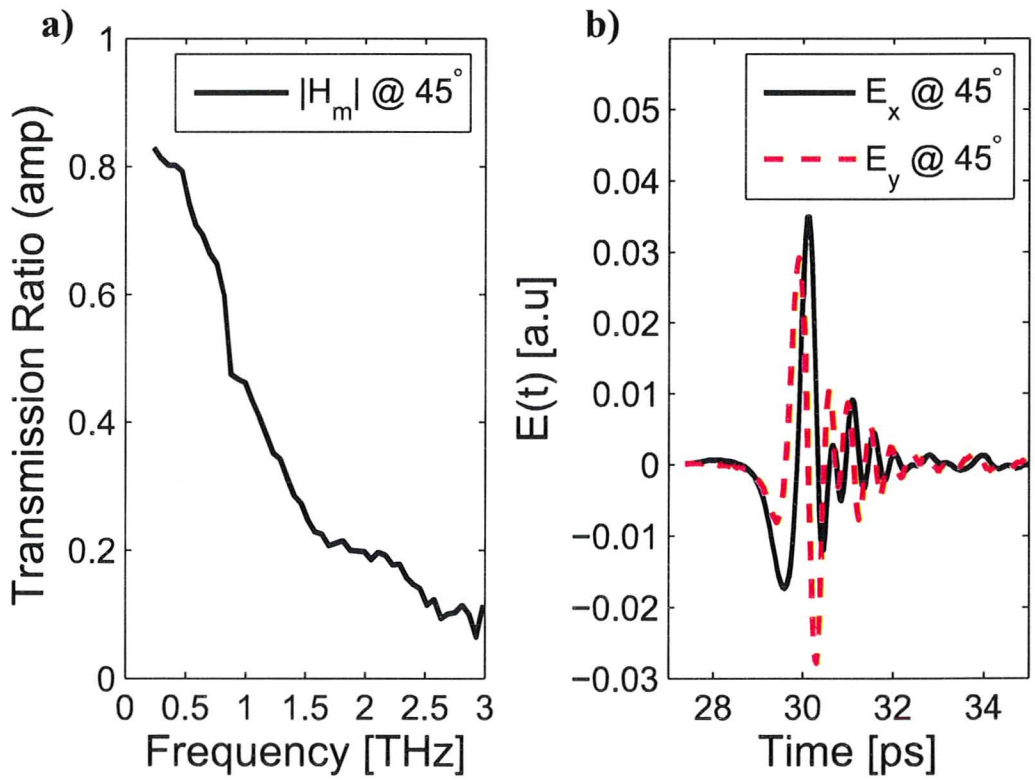

Figure 5.5: Measurements of the performance of the test waveplate a) the transmission ratio of the plate falls off significantly with frequency due to the thickness of the plate and the moderate absorption coefficient. The net transmitted field has an almost flat spectrum from 0.5-2.0 THz due to the normal shape of the spectrum. b) Time domain traces of both electric field components show that the pulse shape is maintained despite transmission through the waveplate, indicating that it is zero-order waveplate.

For the achromatic waveplate to be a useful experimental tool, more strongly birefringent materials are needed. As was shown in Chapter 3, it is possible to significantly increase the birefringence in polymers that have low THz absorption. This ability should enable the construction of a waveplate that has excellent performance, but much lower THz absorption. As an example, the HDPE sample in which birefringence was increased to Δn=0.11, would allow construction of a waveplate only 1.5 mm thick with ellipticity performance equivalent to 5.4b. This waveplate would transmit over 75% of the THz amplitude at 2 THz, even with Fresnel reflections taken into account.

5.5 Conclusion

Using mathematical modelling and non-linear optimization, a process for creating achromatic waveplates has been developed and tested. Through the use of the process, numerous waveplates were created and tested at THz frequencies. The resulting waveplates were achromatic across a broad-band of the spectrum. The best performing waveplate was able to create a THz field that had an ellipticity in excess of $\pm$0.75 across the THz bandwidth from 750 GHz to 2.25 THz.

These waveplates are a proof of concept for more precise waveplates that could be designed using materials with higher anisotropy. Through use of numerous different materials and an appropriate optimization procedure, achieving an achromatic quarter waveplate that is less than 2 mm thick with minimal absorption should be readily achievable.

Chapter 6

THz Gas Sensing

In the current THz literature, experiments involving samples in the solid phase are by far the most prevalent. Solid phase experiments include thick materials investigated to determine their complex dielectric constant, thin films on substrates measured for their materials properties, compressed pellets of heterogeneous material and more. At THz frequencies many liquids present rather uninteresting behaviour and are generally neglected for measurements. From the first THz-TDS experiments, where water absorption lines dominated the response, it was well understood that the gas phase was potentially a rich source for molecular responses at THz frequencies.

While many isotropic gas species have been measured, we are unaware of any reports of measurements of anisotropy in the gas phase in the THz range. Given the high sensitivity of the developed THz polarimeter to anisotropy and the potential for a very long interaction length, on the order of meters, the possibility exists for measurement of anisotropic THz interactions in the gas phase. The following chapter discusses the design of a THz gas sensing system built around the previously described THz-TDS polarimetery setup. The testing of the sensitivity of this system on numerous isotropic polar gas species is also discussed. The ultimate goal of this work is to enable THz circular dichroism spectroscopy in the gas phase, the possibilities of this sort of sensing are left until the following chapter.

6.1 Cell Design and Implementation

A gas cell for spectroscopic purposes can take many different formats. While the simplest format is a simple single pass linear cell, multi-pass cells can be of significant utility for detection of minute changes in absorption. The use of multi-pass cells for THz gas spectroscopy has been previously explored, with cells of path lengths up to 7.5 m to show the detection of parts-per-million levels of various gases species (Harmon and Cheville, 2004).

While multi-pass cells are very useful, their construction quickly becomes an expensive and time consuming endeavour. The White cell cited in the previous study requires three mirrors that are precision machined and mounted in addition to a large rectangular enclosure that is capable of withstanding vacuum. Even using an inexpensive material, such as aluminum, to construct the rectangular enclosure would quickly run costs up into the thousands of dollars given the large dimensions of greater than 60 cm x 60 cm x 15 cm used in the 7.5 m White cell (Harmon and Cheville, 2004).

Given that the standard size for optical tables is approximately 2.0 m, the construction of a single pass cell in the vicinity of 1.5 m should be possible. Using the full 2.0 m would be very difficult given the extra optics required to route the THz and probe beam to the detector, which must be outside the gas cell. When designing the cell, there is an inherent trade-off between the minimum detectable concentration of gases and the maximum absorption coefficient that can be measured. As any measurement system is constrained by a signal to noise ratio, SNR, the upper limit on the length of cell, L, to detect a species of with absorption coefficient of α can be calculated as:

$$L < \frac{\ln\left(SNR(\omega)\right)}{\alpha\left(\omega\right)}. \tag{6.1}$$

In order to decide the appropriate length, the species of interest must be considered. One particular species of interest is methanol, as it has a very rich THz spectrum and is often used for spectroscopic calibration. Over the bandwidth of interest, the peak absorption coefficient of methanol has been measured to be in the vicinity of 0.1 cm^{-1}. The achievable signal to noise

in the THz spectrometer is in the vicinity of 60 dB or 10^6 : 1. Given these values, the upper limit on the length from equation 6.1 is 138 cm. With this information in hand, the length of the single pass cell was chosen to be 125 cm to allow detection of absorption coefficients as high as 0.1 cm^{-1} even if the signal to noise was slightly degraded. Selection of 125 cm also greatly simplified the physical layout on optical table as the THz focussing optics could be fit directly alongside the gas cell.

Most gas cell designs (Harmon and Cheville, 2004) rely on evacuating the cell and then controlling the introduction of gas species up to the vapour pressure of the sample gas at room temperature. This mechanism is highly effective for gas species with high absorption; however, the primary purpose for designing this cell is to detect very small absorption features. Thus, the ability to increase the pressure of the gas species well above the room temperature vapour pressure is quite desirable. The vapour pressure could be increased by simply heating the sample; however, the main gas cell would then be super-saturated and the gas species would condense out on the cell walls and windows. Condensation must be avoided at all costs as most liquids are highly absorbent at THz frequencies. Thus any condensation would completely distort the absorption measurement of the gas species.

The design chosen to avoid the problem described above is a two-cell design, where the liquid sample is maintained in a cold-cell and the measurement conducted within a hot-cell. The hot cell temperature must be maintained above the cold cell otherwise condensation will occur within the hot-cell. The cold cell temperature does not need to be maintained at room temperature, but can be increased to just below the hot-cell temperature. With this design, it is desirable to have a hot-cell operating at as high a temperature as possible. The key parameters limiting the operation of the hot-cell are the melting point of the materials involved and the auto-ignition temperature of the gas species. Above the auto-ignition temperature, spontaneous combustion is expected, thus it should be avoided by a significant safety margin.

The layout of the two-cell design is shown in figure 6.1. The hot-cell should be made from a material with high thermal diffusivity to encourage a uniform

temperature distribution, so a metal is the obvious choice. Stainless steel was chosen for the hot-cell as the reactivity the metal surface with various samples was a key concern.

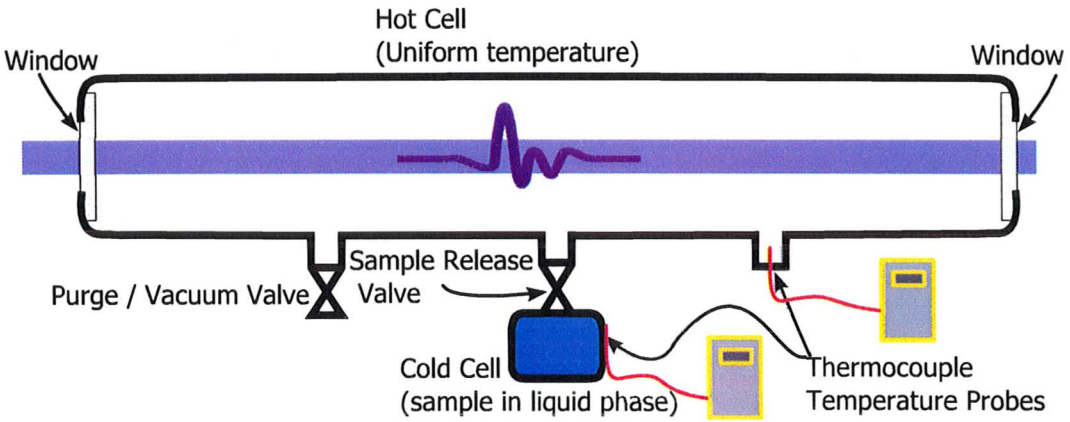

Figure 6.1: Physical layout of the two-cell THz gas spectroscopy chamber. The collimated THz beam is less than 1 cm in diameter (FWHM) and has minimal divergence over the 1.25 m length of the chamber.

Heating of the hot-cell was achieved using a variable power 3 m long heat tape wrapped around the cell with a turn at least every 10 cm. The tape was secured to the cell using aluminum tape and several layers of aluminum foil were used to create an envelope around the cell. The heat tape was rated for up to 375 W; however, the maximum sustainable power was only half that, around 200 W. At the 200 W setting, the hot cell took approximately 2 hours to reach a stable temperature of around 110 °C, which was sufficient for all the species measured.

The internal temperature of the cell was monitored via a thermocouple inserted through a Teflon plug in one of the lateral access paths to the cell. The external temperature was monitored with several thermocouples placed along the length of the cell.

The arrangement for heating the cold cell was much simpler. Due to the small volume, a 20 m of twisted pair waxed 26 gauge copper wire was sufficient to provide about 20 W of heating to the cold-cell. The wire was wrapped around the cell and secured with aluminum foil tape. A thermocouple was

placed underneath wire and provided the temperature reading used to estimate the partial pressure of the gas species.

Gas-Cell Optical Layout

The complete layout of the gas chamber within the THz-TDS setup is shown in figure 6.2.

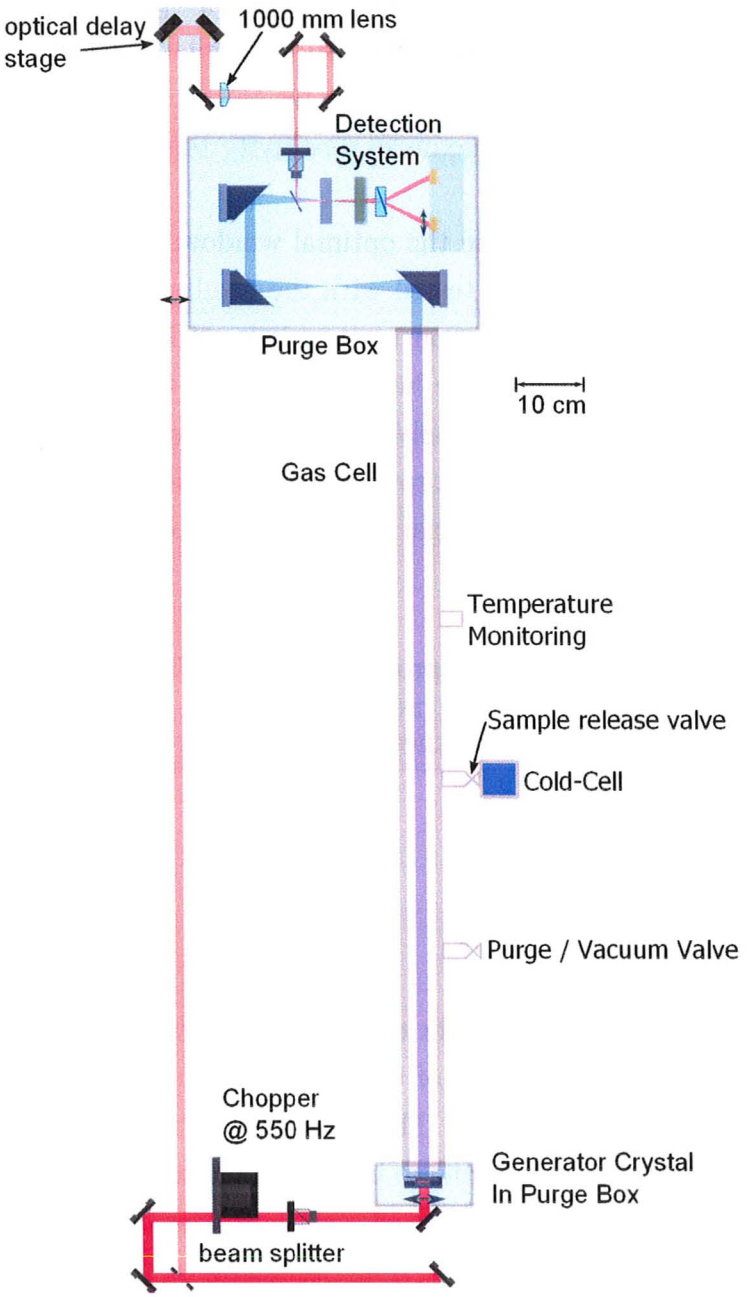

Figure 6.2: The complete optical setup for gas-cell spectroscopy setup. The diagram is to scale.

6.1.1 Window Materials

The choice of materials for windows for the gas cell is very similar to the selection available for the achromatic waveplate design discussed in Chapter 5. The obvious difference is that, for the gas cell windows, the anisotropy should be minimal to maximize sensitivity to anisotropy within the gas-THz interaction.

In order to determine the optimal window material, numerous samples of HDPE and Teflon were tested with the results summarized in table 6.1. Due to its higher glass-transition temperature, HDPE is the preferable choice as it permits operation of the hot cell at higher temperatures . One key disadvantage of HDPE is that polyethylene has a wide phonon band near 2.5 THz that causes significant absorption and distortion of the THz pulse. Selecting HDPE as a window material results in 300 GHz band where measurements are suspect.

Table 6.1: Measured THz properties of potential window materials extracted using the classical analysis method.

Material	Thickness [mm]	α at 2 THz [cm^{-1}]	Δn
HDPE	2.38	2.7	0.007
HDPE	3.18	2.5	¡0.005
HDPE	4.76	2.6	0.009
Teflon	1.52	2.5	0.011
Teflon	3.04	2.4	0.005

As the absorption coefficient is similar for all of the materials tested, the key difference between all of the tested window materials is their mechanical stability and birefringence. The Teflon sheets, in general, are quite flexible and are significantly more prone to bowing when exposed to a pressure differential. The 3.18 mm thick HDPE sheet was chosen for the window material as it has the lowest birefringence and is mechanically rigid enough.

6.2 Data Analysis and Results

In order to extract parameters from gas phase spectroscopy measurements, a similar methodology to solid experiments must be used. As with previous derivations, the electric field components are considered in the frequency domain as continuous functions. With the gas cell in place, the THz radiation traverses the first window, with transmission matrix $\tilde{T}_{w1}$, the gas itself, $\tilde{T}_g$ and a second window $\tilde{T}_{w2}$. Thus the reference and sample scans are related to the scan without the gas-cell in place by:

$$\tilde{E_{samp}} = \tilde{T}_{w2}\tilde{T}_g\tilde{T}_{w1}\tilde{E}, \tag{6.2}$$

$$\tilde{E_{ref}} = \tilde{T}_{w2}\tilde{T}_{purge}\tilde{T}_{w1}\tilde{E}. \tag{6.3}$$

For the purposes of the following experiments, molecules with isotropic features are being considered, so the transmission matrices of equation 6.2 and 6.3 are simplified to complex scalars. In addition, it is assumed that the gas mixture is homogeneous and can be represented by a complex index of refraction at every frequency.

$$\tilde{H}_m = \frac{\tilde{E}_{samp}}{E_{ref}} = \exp\left(\frac{i(n_g - 1)\omega L}{c}\right) \exp -\left(\frac{\alpha L}{2}\right) \tag{6.4}$$

Even in cases where the absorption is significant, the deviation in the real part of the index of refraction of the gas n between the purged tube and the tube with the sample in place will be quite small. Thus the measured transfer can be rewritten, assuming $n_g = 1$, as: $\tilde{H}_m = \exp -(\frac{\alpha L}{2})$. It is then clear that the absorption coefficient, α_m can be determined from the magnitude of the measured transfer function, and obtained as:

$$\alpha_m = \frac{2}{L} \ln \left|\tilde{H}_m\right|. \tag{6.5}$$

The determination of α_m can also be used to determine the relative density of absorbers within the chamber. From the Beer-Lambert Law, the absorption coefficient is equivalent to the product of the absorption cross section σ and

the density of absorbers N: $\alpha_m = \sigma N$ (Swinehart, 1962). The absorption cross section is not generally known; however, if the temperature of gas species is held constant, then σ should be constant. Thus, by comparing the absorption coefficient at multiple different cold-cell temperatures, the ratio of $N(T)/N_0$, where N_0 is the quantity of absorbers at the reference temperature, can be determined. It should be noted that the Beer-Lambert Law is only truly applicable for monochromatic light sources, in the case of broadband sources, numerous other deviations must be considered (Swinehart, 1962). Despite these shortcomings, this method still provides a direct quantification of the gas density in the chamber, provided care is taken in its application.

6.2.1 Experimental Optimization

One of the critical parameters affecting the quality of THz experiments is the stability of the entire experimental system. In the case of THz-TDS, the stability of the mechanical apparatus, the thermal environment and the humidity must all be well controlled, in addition to the stability of the laser and detection electronics. The gas cell system adds an additional complication to maintaining a stable THz setup, as the hot cell has a large thermal mass and must be heated above the boiling point of the material under study.

The first step in addressing stability in gas-cell experiments is to address the temperature stability of the entire apparatus. Before even starting the laser in gas cell experiments, the heater for the hot-cell was turned on and set to the desired power level. The apparatus, including the gas cell, thus had several hours to reach equilibrium while awaiting the laser warm-up. Typically four hours was required for sufficient stability.

During the experiment itself, temperature stability is also an issue as the cold-cell temperature is changed. In the case of the cold-cell temperature being changed, waiting several hours for an equilibrium to be reached is simply not an option, as experiments would require several days to complete. Instead, 15-30 minutes, depending on the temperature difference required, were allowed to elapse while the system came to equilibrium.

When taking actual THz measurements, the step time was reduced to the

minimum workable step duration, 200 ms, resulting in a scan time of under 3 minutes for a 768 point, 40 ps scan. At each cold-cell temperature a minimum of five THz scans were taken. During data analysis, stability was then checked by ensuring the standard deviation of the THz power in several key frequency bins, 1 THz, 1.5 THz and 2.0 THz, was less than 1 percent. If the standard deviation with the five measurement sample exceeded this threshold, the data was rejected. For each individual sample, specific spectral absorption bands were also checked to ensure their stability over the five measurements was within 5 percent.

Reducing the step duration to 200 ms results in significant decrease in the signal to noise. As the data has been verified to be stable, the five THz scans taken at each temperature were averaged. Assuming purely random noise, this averaging should improve the signal to noise ratio by $\sqrt{5}$ or 3.5 dB.

The above methodology was developed through repeated experimental trials. All of the results in the following section utilized this methodology.

6.2.2 Uncertainty in Spectroscopic Parameter Estimates

Before delving into several different spectroscopic studies, an important note should be made about the uncertainty in absorption coefficient estimates using THz-TDS. In order to obtain a THz-TDS absorption spectra, two measurements are required, a sample and reference, and both of these measurements influence the uncertainty of parameter estimates. Taking both of these contributions into account, the uncertainty in the parameter estimate can be readily determined through some simple calculus.

The uncertainty in the measured spectra can be estimated by calculating the variance of the complex spectra over the region of 3 - 6 THz. It is important to chose a region just outside the experimental bandwidth for the noise estimate as the effect of proportional noise does not contribute significantly at higher frequencies. Using this region for the noise estimate, the uncertainty in the absorption coefficient for one of the water measurements in the following section has been calculated and is shown in figure 6.3.

The most significant influence on the uncertainty at a particular frequency

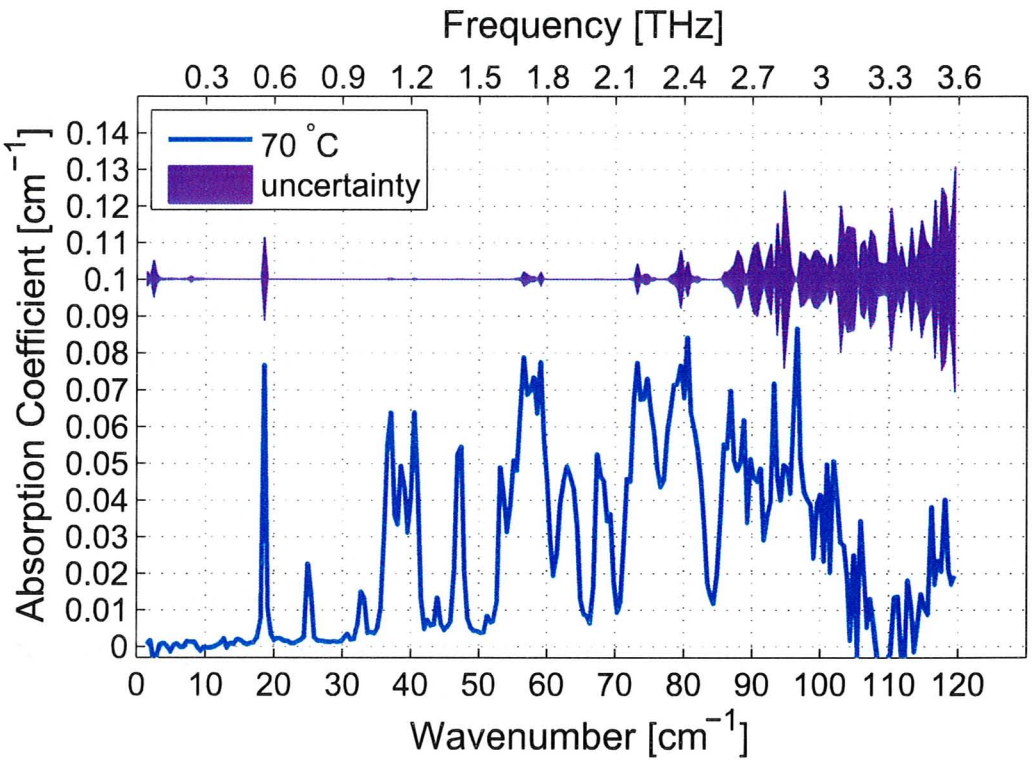

Figure 6.3: Measurement of the absorption spectra of water with the cold cell at 70°C and the estimated uncertainty in the absorption coefficient, offset by 0.1 cm^{-1}. The uncertainty of the measurement at each frequency bin is dependent on the reference measurement power and noise spectrum, as well as the sample measurement power and noise spectrum.

bin is the amplitude of reference spectrum at that frequency. At low frequencies, the numerous spikes in the uncertainty seen in figure 6.3 are due to water absorption lines. As the THz focussing and detection system can not be completely purged of water, some absorption is present in the reference, even if the gas cell is completely purged. The reduction in reference amplitude at these frequencies results in more uncertainty in later absorption coefficient estimates.

Another important influence on the uncertainty is the presence of highly absorbing regions in the sample measurement. In these regions of the spectrum very little THz energy remains after passing through the gas cell. This results

in an asymmetric uncertainty, although this has not be shown in figure 6.3.

These two factors, the power in the reference measurement and the remaining power in the sample spectrum, should be kept in mind when considering the absorption spectra in the following sections. Individual uncertainty estimates are not shown for every spectrum, as it would be very difficult to fit on the individual graphs. The absorption coefficient where the THz energy has been absorbed to such an extent that the sample measurement signal to noise is 0 dB is shown as the upper "detection limit" on numerous graphs.

6.2.3 Water

The significant spectral absorption features of water vapour at THz frequencies are one of roadblocks that make THz-TDS challenging. The large variety of rotational and rotational-vibrational modes in water vapour also make it an interesting case for study. THz studies of water vapour in a flame (Cheville and Grischkowsky, 1998), in various ambient atmospheres (Gasster *et al.*, 1988), and at various pressures (Podobedov *et al.*, 2004) have provided insight into details of these modes. As water vapour is an important constituent of the atmosphere, its spectral properties are of interest to climate scientists, radio astronomers and engineers developing the next generation of wireless communication systems.

Water vapour provides a good test case for a gas spectroscopy system as it is readily available, has a high vapour pressure and is spectrally rich. Experiments were conducted using steam distilled water obtained from regular CCEM supplies. Approximately 2 mL of water was loaded into the cold cell while it was isolated from the hot cell, which was preheated to 110°C and purged first with room temperature helium, followed by room temperature nitrogen. After loading the sample and sealing the cold cell, a valve between the hot and cold cells was opened and the water vapour was allowed to diffuse into the chamber.

While a naïve view of the kinetic theory of gases would seem to suggest the diffusion of H_2O vapour into N_2 would occur quite quickly, experimental results indicate otherwise. When the valve between cells is opened, the vapour

pressure of H_2O in the cell remains quite low for upwards of several hours. This can be seen in figure 6.4 where the absorption remains almost negligible even as the cold cell is raised 62°C. The source of this slow diffusion is a combination of the relatively narrow pathway between the hot and cold cell and the density difference between the H_2O vapour and N_2 gas. The pipe leading between the two cells has a cross section of $9mm^2$ and so the density difference can allow a slow moving plug to form within the gas. During experiments, the rate of diffusion into the hot cell was significantly affected by rotating the cold cell to a slight incline, allowing the density difference to be exploited to increase the rate of diffusion.

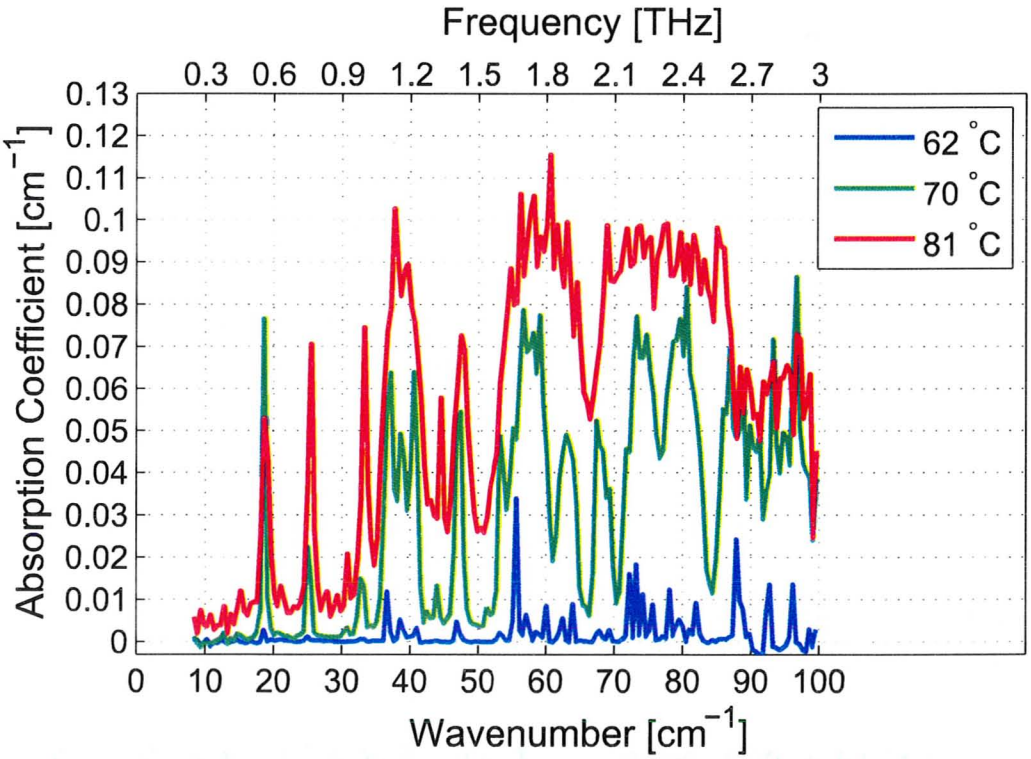

Figure 6.4: Spectral absorption lines of water vapour at THz frequencies when added into an N_2 environment. Initial N_2 pressure was 1 atm and the gas cell temperature was 110°C. The vapour pressure of water in the hot cell was increased until absorption saturation occurred by increasing the temperature of the cold cell.

In order to gain an estimate on the change in the density of water molecules in the hot-cell as the cold-cell temperature is varied, individual absorption bands must be considered. The strong absorption bands in figure 6.4 around 1.10 THz, 1.68 THz and 2.63 THz are good choices for monitoring. When using the absorption strength of bands to estimate the density, N, based on the Beer-Lambert law, several systematic problems must be noted. First, N should ideally be extracted from measurements using monochromatic radiation to excite a single transition. In the case of THz-TDS, what appears to be a narrow absorption feature is likely a composition of tens or hundreds of different molecular transitions. Second, as the density increases, these absorption bands merge together to form even wider bands. When this occurs, N can no longer be extracted reliably.

Numerous models of varying accuracy exist to describe the vapor pressure of a gas above a liquid. The most widely used model in engineering is the Antoine Equation and its variants. The Antoine equation, shown as equation 6.6, is an simple logarithmic relation that is derived from the Clausius-Clapeyron relation assuming a temperature independent heat of vaporization (Thomsone, 1946). The coefficients for a specific material can be obtained from a wide variety of handbooks and the vapour pressure estimated. Significant deviations from the Antoine equation are known to occur near the critical temperature, although it gives sufficient accuracy for most engineering purposes (Thomsone, 1946; Calingaert and Davis., 1925).

$$\log_{10} P = A - \frac{B}{C + T}. \tag{6.6}$$

Figure 6.5 shows the result of using the Beer-Lambert Law to calculate the change in N and the Antoine equation to calculate the theoretical relationship. At temperatures below 65°C, experimental measurements and the theoretical relationship agree well. Above 65°C, however, there is significant disagreement in different directions depending on the frequency range chosen.

As the upper detection limit for α is reached, the estimated value of N is expected to level off, as there is insufficient energy left within those frequency bins to gain an estimate. This effect can be seen in the absorption features at

1.68 THz and 2.63 THz when used to estimate N above 80°C.

Another effect than can occur at higher densities is the merging together of several absorption bands resulting in significantly greater absorption within the frequency bin and an overestimate of N. At the 1.10 THz bin we see this overestimate effect clearly taking place as the estimated N shows a five-fold increase over a 10°C range. Around the 1.10 THz bin several bands of absorption are actually present, spanning the region from 1.05 THz to 1.25 THz. The large overestimate of N is likely due to the merging of these bands as the density is increased.

The effects of pressure, temperature (Podobedov *et al.*, 2004) and collision (Gasster *et al.*, 1988) broadening have been studied at THz frequencies. While the results of these studies could be combined to form a model to confirm the experimental measurements of figure 6.4, a non-trivial amount of simulation work would be required to effectively model the THz-TDS experiment.

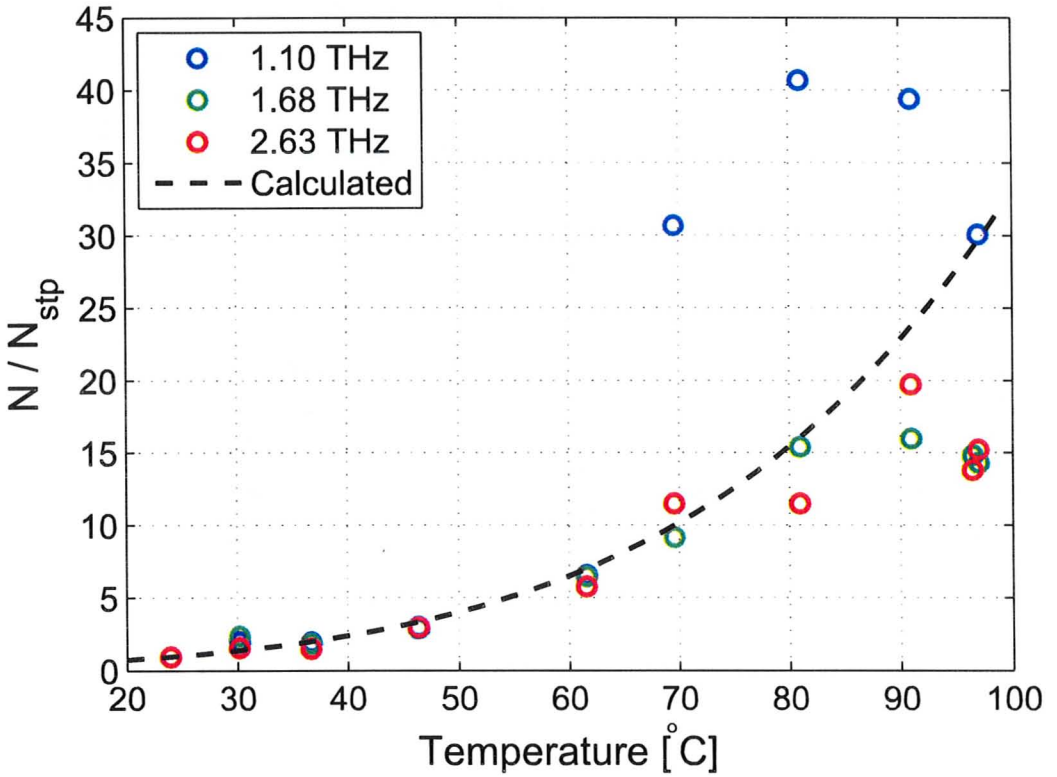

Figure 6.5: Estimated density of water molecules from THz measurements assuming linear dependence on absorption and calculated dependence based on the Antoine equation at various cold cell temperatures. Significant deviations from the calculated dependence occur as the density increases due to the combined effects of spectral broadening, merging of transition bands, and the upper detection limit.

One method to get around the slow diffusion rate between different vapours is to eliminate the problem entirely by pumping the hot cell down to a rough vacuum level. Using a mechanical roughing pump, the N_2 was pumped out of the hot cell after following the same purging procedure outlined above. After loading a 2 mL distilled water sample, the valve between the hot and cold cells was opened. As shown in figure 6.6, the absorption spectra with the cold cell at room temperature when the cell is initially under vacuum shows significantly stronger absorption than when 1 atm of N_2 is in the hot cell.

The stronger absorption is clearly due to the much higher partial pressure

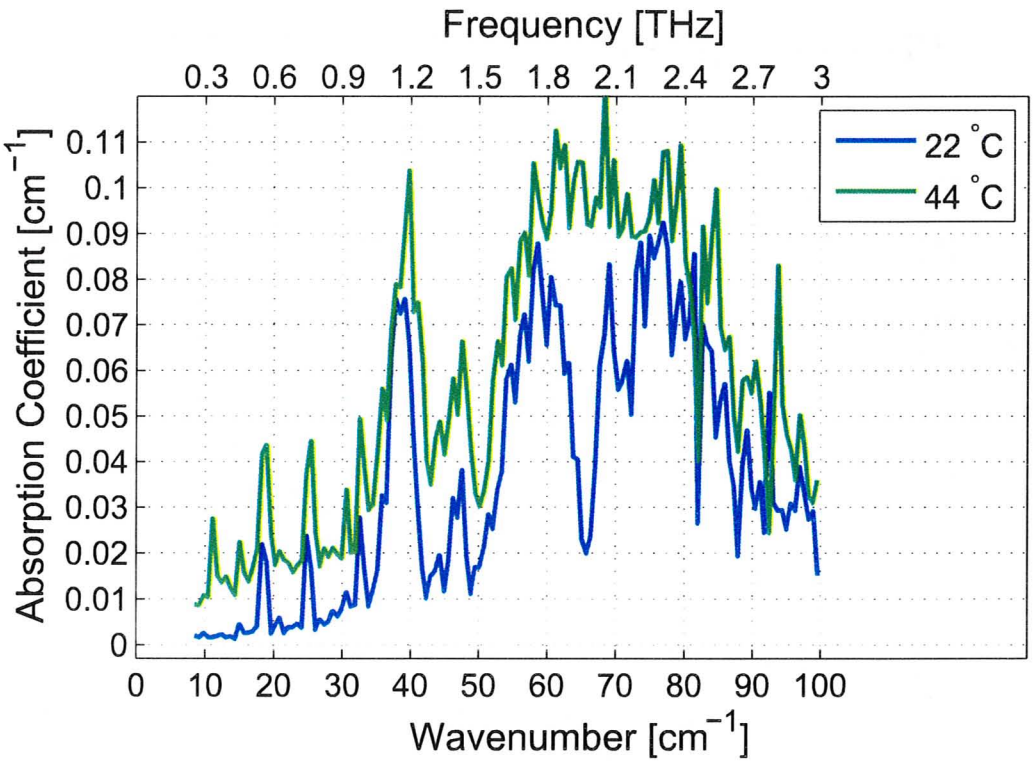

Figure 6.6: Spectral absorption lines of water vapour at THz frequencies with hot cell initially at a rough vacuum. The vapour pressure of water in the hot cell was increased by raising the temperature of the cold cell until the THz energy in several regions of the spectrum was completely absorbed, resulting in a saturation of measurable absorption coefficient.

of water vapour in the hot cell. Independent pressure data is not available for this particular experiment. Comparison with the previous results of water vapour in an nitrogen atmosphere indicate that the absorption in vacuum with the cold cell at 22°is comparable to the absorption in nitrogen with the cold cell at 70°. Directly comparing these two data sets, as shown in figure 6.7, shows some very marked differences. While the absorption peaks below 1.5 THz are similar in character, the differences in absorption around 1.85 THz and 2.0 THz are particularly striking.

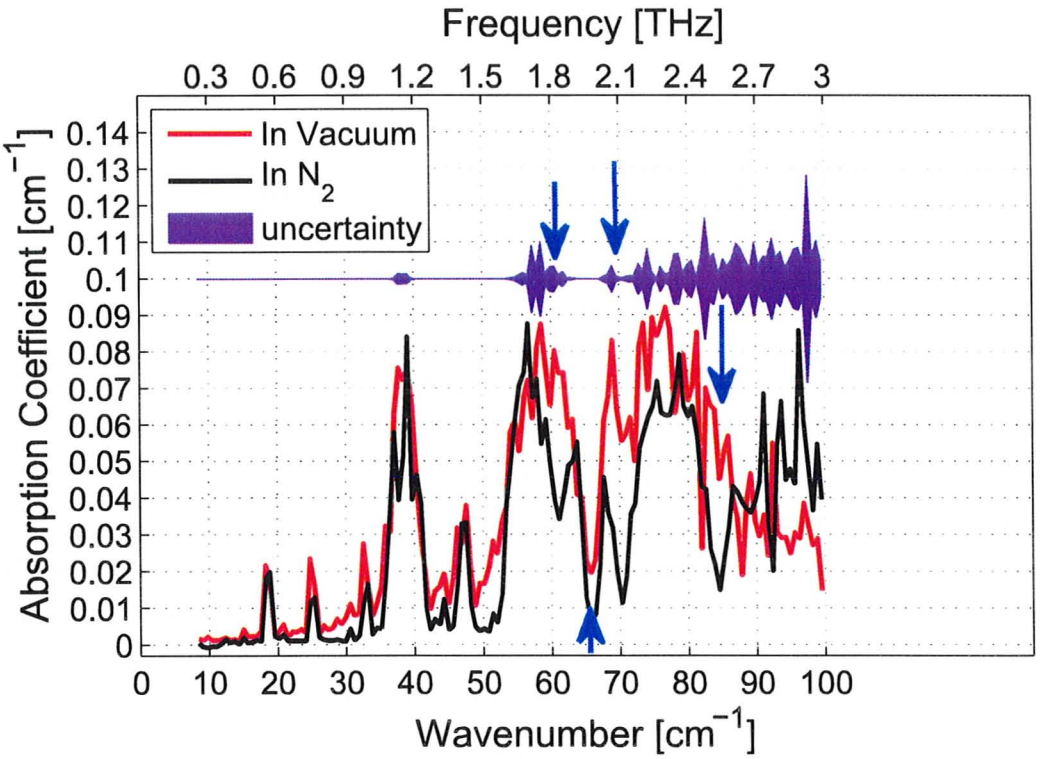

Figure 6.7: Comparison of the absorption spectra of water vapour in an nitrogen ambient and in vacuum. In vacuum, absorption bands are present at 1.85 THz and 2.05 THz that are not present in the nitrogen ambient. The anomalous absorption at 2.05 THz corresponds to an absorption feature of the water tetramer seen in previous studies (Cruzan *et al.*, 1997). The uncertainty shown has been calculated for the measurement in vacuum. The uncertainty estimate for the measurement in nitrogen is similar.

Within the entire absorption spectra, the data set in vacuum also shows a general trend of absorption coefficient increasing in a quadratic like trend with frequency. This type of trend is indicative of liquid water and indicates a possible explanation for the large differences in the spectra. As the density of water molecules in the tube increases, the formation of clusters of increasing size becomes possible. Previous literature reports that both the trimer, $(H_2O)_3$, and tetrameter of water, $(H_2O)_4$, have a vibration-rotation modes at approximately 68 cm^{-1} or 2.05 THz (Cruzan *et al.*, 1997). The data of figure 6.7 supports the existence of the tetramer state in an experiment conducted

with the cold cell initially in rough vacuum. The other outstanding absorption feature at 1.85 THz (61 cm^{-1}) could be due to an even larger cluster of water molecules. The trend for the absorption feature around 2 THz is for its resonant frequency to decrease with increasing cluster size (Cruzan *et al.*, 1997), so the 1.85 THz feature may be due to the pentamer, hexamer or even higher order clusters of water molecules.

The apparent lack of clustering in the experiments conducted in an nitrogen ambient has a simple explanation. Even in a rough vacuum, the nearest neighbour for every water molecule should almost exclusively be another water molecule or cluster of molecules. Thus the probability of several molecules reducing their potential energy by organizing into a cluster is not impeded by other molecules. Within the nitrogen environment, the non-polar N_2 molecules are of higher density than the water molecules and pose an impediment to clustering. An N_2 molecule which approaches a water tetramer has the opportunity to disrupt the delicate balance of fields which allows the cluster to exist.

This particular data set demonstrates how a seemingly simple interaction of H_2O can become interesting to study using THz radiation due to the ability to probe collective vibrational modes. While THz-TDS does not provide the spectral resolution necessary for in-depth verification of *ab initio* calculations, it does provide the opportunity to study the formation, evolution and destruction of these states. While this work primarily focusses on static THz-TDS experiments, the possibilities for studies of molecular and cluster dynamics using pump-probe techniques make THz-TDS an intriguing tool for chemists (Schmuttenmaer, 2004).

6.2.4 Acetone

Acetone is a widely used laboratory solvent that is miscible in water. As a test subject for gas phase spectroscopy, it is of interest due to its extremely strong absorption at low THz frequencies. Literature indicates that at room temperature the absorption of acetone across a broad-band of THz frequencies is greater than 0.5 cm^{-1}.

The level of expected absorption should result in the THz energy in several regions of the spectrum being completely absorbed, resulting in a saturation of measurable absorption coefficient. The complete absorption of energy in certain spectral regions results in an effective upper detection limit for the gas-cell apparatus. Throughout this chapter, this upper "detection limit" is often referenced and acetone provides the opportunity to verify the procedure for the estimation of this limit from SNR measurements.

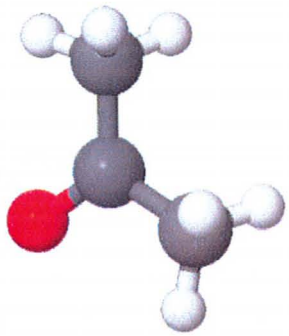

Figure 6.8: Equilibrium structure of the acetone molecule rendered using Jmol (Herraez, 2007). Hydrogen atoms are in white, oxygen atoms in red, and carbon atoms in dark grey.

Table 6.2: Physical properties of acetone from (David R. Lide, 2010)

Property	Value
Boiling Point	56.5 °C
Dipole Moment	2.91 D
Autoignition Temperature	465 °C

Using the same experimental methodology as the experiments conducted with water, 2 mL of acetone was loaded into the cold-cell with the hot-cell at a uniform 104 °C. Special care must be taken when working with acetone as its flash point is -17 °C, so any potential spark or flame may ignite the vapours.

The measured absorption spectra for acetone is shown in figure 6.9. The absorption clearly reaches the detection saturation limit for the spectrometer setup, at frequencies below 1 THz. Some of the sharp features at 1.9 and 2.25 THz may be due to water contamination.

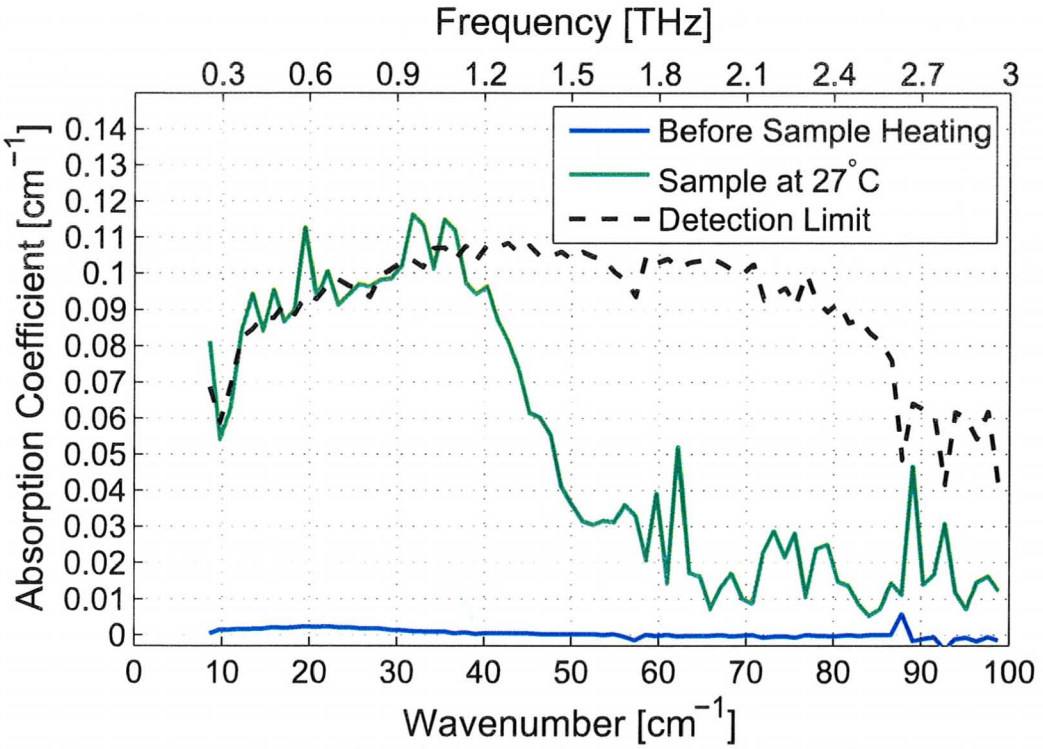

Figure 6.9: Absorption coefficient for acetone at THz frequencies. The absorption coefficient is above the detection saturation limit.

6.2.5 Alcohols

In earlier sections, the THz absorption spectra of both water and acetone provided interesting cases for analysis. The source of these spectra were the large dipole moments of these molecules, which allowed the THz radiation to couple into various rotational, torsional and collective modes. Another useful target class of molecules are alcohols. The three smallest alcohols, methanol, ethanol and isopropanol (2-Propanol) have relatively large dipole moments and vastly different THz absorption spectra. These three alcohols also have relatively high vapour pressures and low boiling points, making them ideal candidates for the temperature limited system.

Methanol

Methanol is widely used for calibration of gas spectrometers due to its abundant absorption spectra over a large wavelength regime (D. Teyssier, 2004). With only a single carbon atom, methanol is the simplest possible alcohol and its rich absorption spectrum comes from the numerous rotational and torsional transitions possible. Calculation of the methanol spectra is complicated by the phenomena of internal rotation, which occurs as the hydrogen nuclei rotate with respect to the hydroxyl group (Belov *et al.*, 1995). The molecular structure of methanol is shown in figure 6.10.

Table 6.3: Physical properties of methanol from (David R. Lide, 2010)

Property	Value
Boiling Point	64.7 °C
Dipole Moment	1.69 D
Autoignition Temperature	470 °C

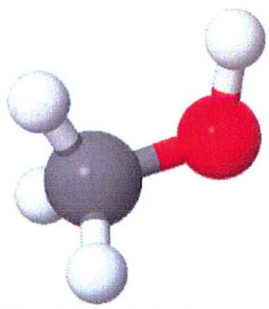

Figure 6.10: Equilibrium structure of methanol molecule rendered using Jmol (Herraez, 2007). Hydrogen atoms are in white, oxygen atoms in red, and carbon atoms in dark grey.

Initial attempts to conduct the experiment in a nitrogen environment resulted in an extremely slow diffusion rate, such that negligible absorption occurred even after several hours of waiting. As with water, pumping the chamber down to a rough vacuum resulted in high concentrations of methanol vapour even with the cold cell at the relatively low temperature of 41°C. The

measured absorption spectra over the entire THz bandwidth is shown in figure 6.11, and has been verified against a meta data base of calculated and measured methanol transitions.

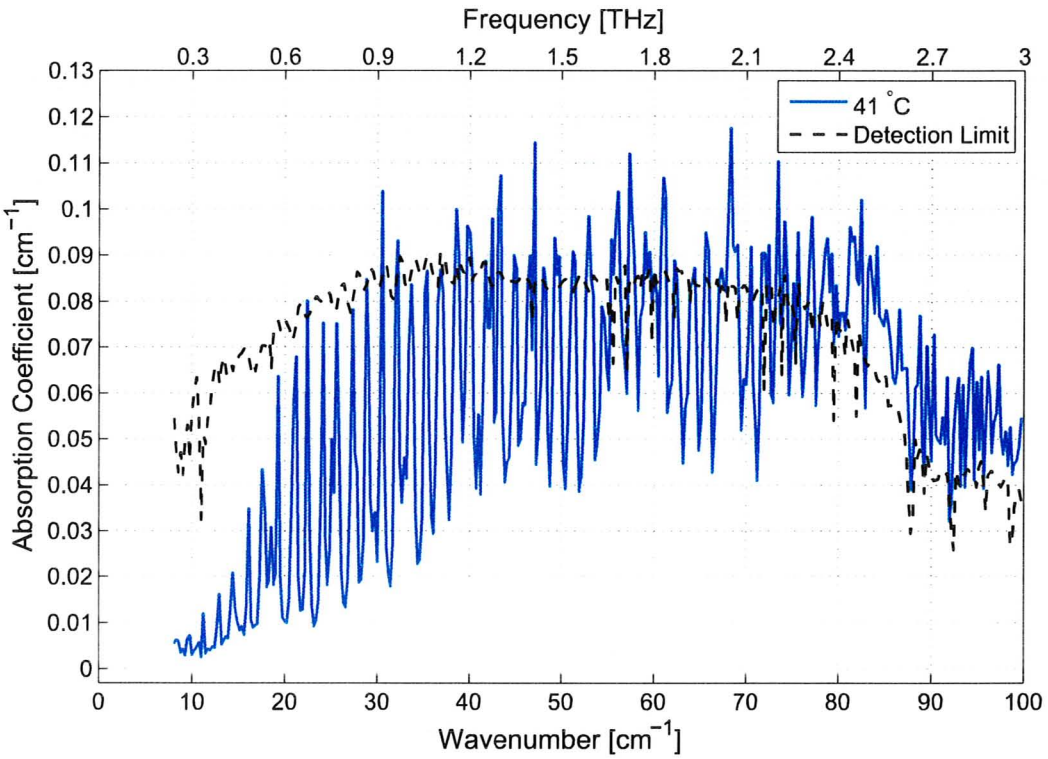

Figure 6.11: Absorption coefficient of methanol in vacuum with the cold cell at 41°C and the hot cell at 104°C.

In order to verify the measured THz absorption lines are in fact due to transitions in the methanol, various data bases of methanol transitions in the THz region were examined. A measurement of sufficient quality using THz-TDS is not known to be available; however, microwave experts have compiled large data bases of over 29,000 transitions measured using a backward wave oscillator (BWO) for THz generation and a helium cooled bolometer for detection or Fourier Transform Far Infrared Spectroscopy (FTFIR) (Xu *et al.*, 2008). As BWO's have been used for generation, the distribution of measured lines are skewed towards the region below 1 THz, with the majority of measurements being below the 250 GHz threshold for detection using the PRL

THz-TDS.

The typical uncertainty in the measurements of spectral lines is 50-250 kHz which is several orders of magnitude below the spectral resolution possible using THz-TDS. Thus the THz-TDS measurements are not measures of individual spectral lines, but ensembles of numerous lines within the frequency range of the discrete Fourier transform bin being considered. The frequency domain smearing effect of the applied or effective window, discussed in chapter 2, also serves to increase the width of the combined ensemble of spectral lines. One method to translate the spectral data base into an expected THz-TDS measurement would be to take the data base and calculate the absorption coefficient for each frequency bin by taking the appropriate integral over all the spectral lines convolved with the window function. One flaw with the readily available methanol spectral data bases is that measured line strength is not included within the data base, making calculation of the aforementioned integral impossible. Some lines may also be included multiple times from multiple different measurement sets.

As the quality of the measured data should be verified against some data base, an approximate method was used to calculate the expected THz absorption spectrum. Each line in the data base was simply assigned equal strength of one and the integral approximated by a sum over the lines within frequency bin. This method neglects the smearing effect of windowing and relative strength difference between the spectral lines. It is also prone to systematic bias due to the duplication of measured lines within data base in the low frequency regions of the spectrum and holes within the data base in the higher frequency regions. With these caveats in mind, figure 6.12 shows a closeup of the measured THz absorption spectrum of methanol with the expected absorption spectrum superimposed.

Comparing the measured spectrum with the expected spectrum reveals several observations. First, with the exception of the absorption ensembles near 0.72 THz (24 cm^{-1}) and 1.00 THz (35 cm^{-1}), there is a high degree of agreement between the measured and expected spectra. While some absorption peaks do show a blue shift, the trend is not significant and may simply

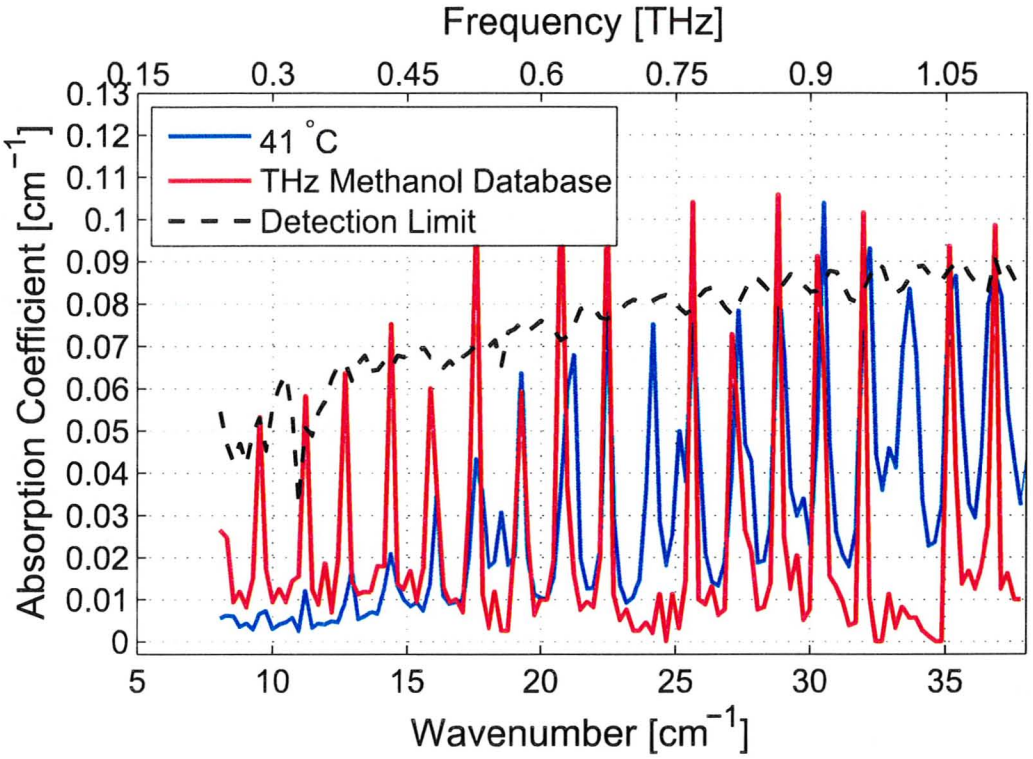

Figure 6.12: Expansion of absorption data shown in figure 6.11 to show the region 0.15 to 1.05 THz, where the net absorption goes through peaks and valleys with regular intervals of approximately 47 GHz. The measured data is superimposed on the expected absorption based on the number of spectral lines within each frequency bin.

be due to smearing due to windowing or stability issues in the apparatus. The previous measurements of water vapour in section 6.2.2 showed agreement with other measurements (Van Exter *et al.*, 1989) of the location of absorption peaks up to 1.4 THz to a single GHz. This degree of agreement in previous experiments using the same apparatus makes it highly unlikely that the disagreement shift is due to a calibration error.

The lack of absorption ensembles at 0.72 THz and 1.00 THz is likely due to deficiencies in the data base and the aforementioned systematic errors introduced by the spectrum estimation method. Other measurements do indicate a large ensemble of transitions at 0.72 THz and 1.00 THz (Belov *et al.*, 1995)

and the absence of these measurements in the data base may be something to note.

Ethanol

The second simplest alcohol possible, after methanol, is ethanol. Ethanol has a backbone of two carbon atoms with a hydroxyl group on one of the carbon atoms figure 6.13. The ethanol sample was obtained from regular PRL supplies and may have been exposed to ambient atmosphere for a significant amount of time. As water is completely miscible in ethanol (and vice-versa), the sample may have been contaminated.

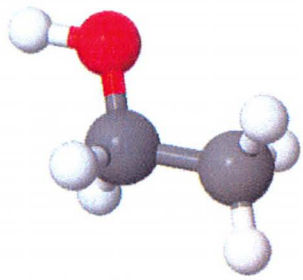

Figure 6.13: Equilibrium structure of the ethanol molecule rendered using Jmol (Herraez, 2007).

Table 6.4: Physical properties of ethanol from (David R. Lide, 2010)

Property	Value
Boiling Point	78.4 °C
Dipole Moment	1.69 D
Autoignition Temperature	422 °C

The absorption measurements for ethanol are shown in figure 6.14. The expected absorption profile is generally smooth broad absorption; however several sharp features are present in the spectrum around 1.0 THz, 1.4 THz and 2.25 THz. A quick inspection of the water spectrum in figure 6.4 shows that these locations correlate with known water vapour absorption bands. Thus, the sample is likely contaminated by a small amount of water.

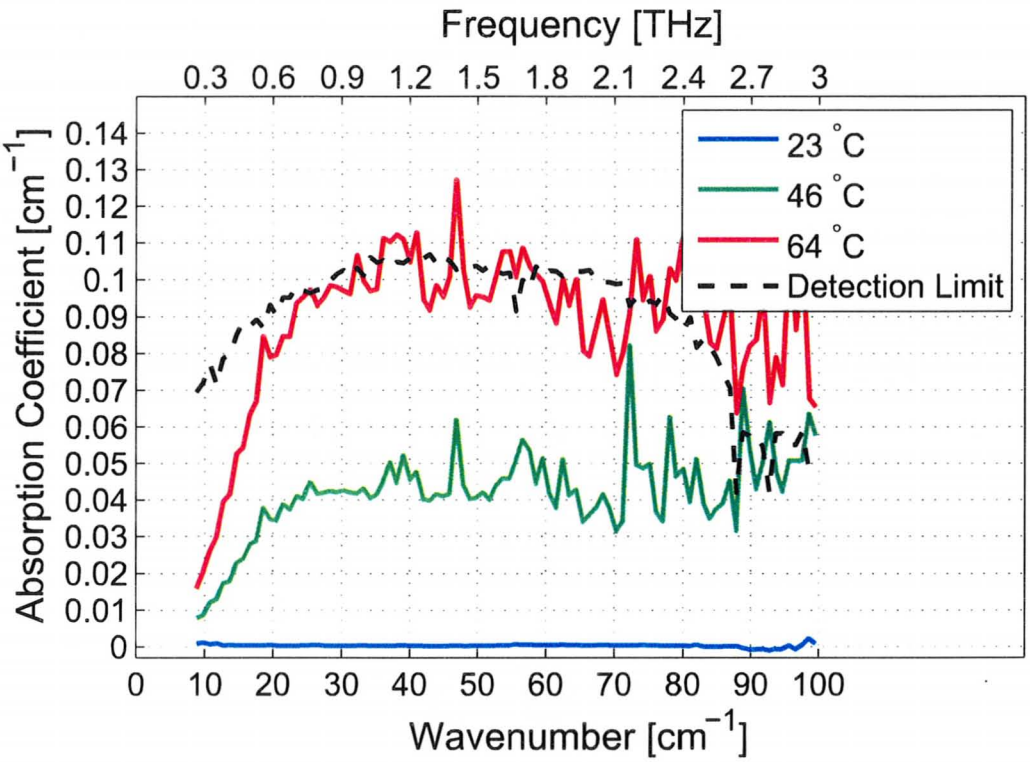

Figure 6.14: Absorption coefficient of ethanol in nitrogen ambient with the hot cell at 104°C.

While the measurement could be repeated using a better sample, there is no particular feature of interest that would compel such a measurement. The contaminated spectra of figure 6.14, serves to show the general trend of absorption features in the first three alcohols, which is our interest at this point.

Isopropanol

Also known as isopropyl alcohol or 2-propanol, isopropanol is one of several isomers of propanol. In isopropanol the hydroxyl group is attached to the middle carbon, which also attached to two methyl groups, as seen in figure 6.15. Commonly referred to as rubbing alcohol, isopropanol is a commonly used and readily available solvent. The isopropanol use in these experiments was obtained of topical grade and from a commercial vendor with stated purity

of at least 99 %.

Table 6.5: Physical properties of isopropanol from (David R. Lide, 2010)

Property	Value
Boiling Point	82.5 °C
Dipole Moment	1.66 D
Autoignition Temperature	399 °C

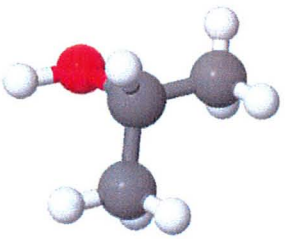

Figure 6.15: Equilibrium structure of isopropanol molecule rendered using Jmol (Herraez, 2007).

The behaviour of isopropanol in experiments, shown in figure 6.16, differs from the other gases as the absorption increases almost linearly as the cold-cell temperature is increased. While the high temperature and low temperature absorption ratio agrees with the Antoine Equation, intermediate temperature points do not. The intermediate points show concentrations significantly above the expected concentration with the overall shape of the concentration versus temperature plot being almost linear.

This behaviour is most likely an indication of a poor equilibrium within the cold-cell, and not some significant deviation from the well-established Antoine equation. This behaviour is quite different from the deviations in expected behaviour seen in water and cannot be attributed to broadening of absorption modes.

One feature of the isopropanol absorption spectrum that is the significant difference between it and the ethanol spectrum. The isopropanol absorption spectrum features a strong but broad absorption band centered around 0.65 THz and then an almost liquid like absorption feature that increases proportional to the frequency. These features of isopropanol are distinct from all of

the other gas species measured.

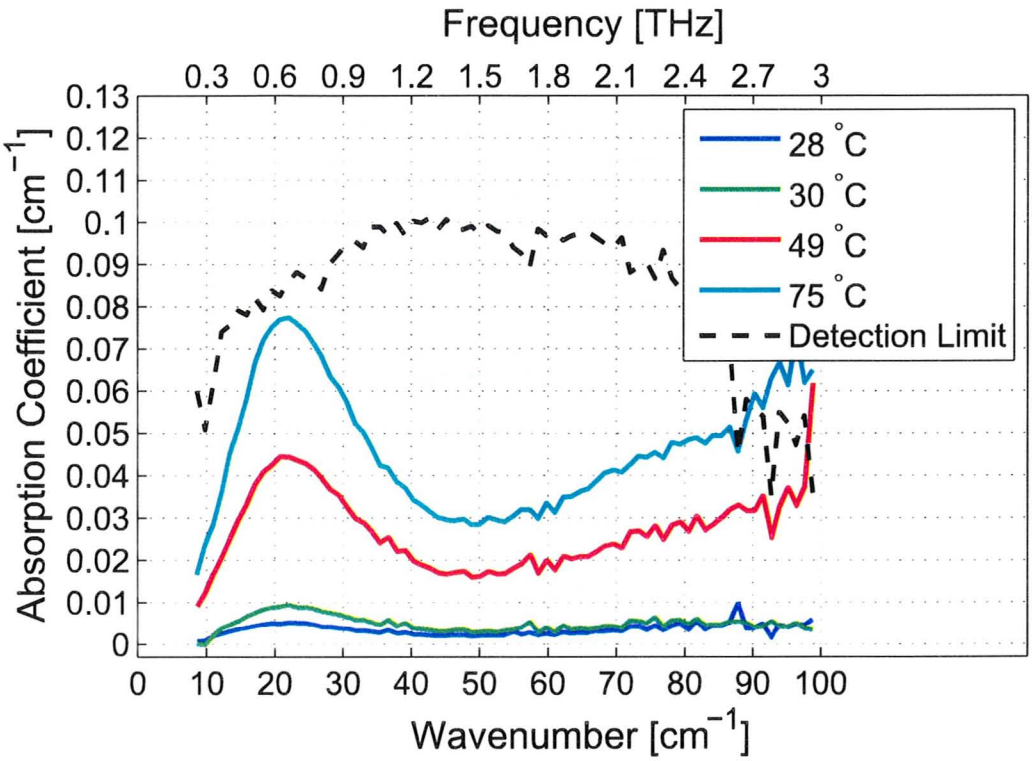

Figure 6.16: Absorption spectra of isopropanol measured using THz-TDS. Two main absorption bands are present, a strong band centered at 650 GHz with a width of 400 GHz and an extremely broad feature that increases almost directly proportional to the frequency of the radiation.

6.3 Conclusion

Several isotropic gas species have been measured to verify the operational characteristics of the gas-cell. The apparent absorption feature corresponding to the water tetramer exemplifies the utility of THz-TDS in spectroscopic applications. The ultra-broadband nature of THz-TDS allows for quick determination if features are present. Using long-baseband THz-TDS, where scans several hundred picoseconds in duration are taken, could allow for more precise investigation of individual molecular transitions, rather than the ensembles seen

with scans of tens of picosecond duration.

While measuring collective vibrations of gases is interesting, it is not the true motivation of this work. As mentioned previously, this cell was designed with the intent of measuring circular dichroism at THz frequencies. The work in this chapter shows that even very small absorption coefficients of 10^{-4} cm^{-1} can be seen and distinguished using this system. Resolution on this order of magnitude is necessary to see the predicted levels of dichroism for molecules of interest.

Chapter 7

Future Work and Conclusion

7.1 Future Work

As with many theses, the result of this work poses many possibilities for future work. A selection of these possibilities are discussed in the following sections with a final discussion being reserved for the issue of circular dichroism spectroscopy at THz frequencies.

7.1.1 Improving Frequency Resolution for Spectroscopic Measurements

In most many spectroscopy experiments, the frequency resolution is set either by the line width of a monochromatic source, or the spatial resolution of a sensor. In a THz-TDS measurement the frequency resolution is constrained by completely by the duration of the time scan. While increasing the duration of a scan may introduce additional complications, such as Fabry-Perot reflections off the generator and detector crystals, these can be overcome through appropriate data analysis. The separation between frequency bins in a THz experiment, where N data points are taken at a sampling time of T_s, is:

$$\Delta f = \frac{1}{NT_s}. \tag{7.1}$$

The product NT_s is the total scan duration and in the most high resolution

scans in this thesis was 40 - 50 ps, yielding a frequency resolution of 25 - 20 GHz. With a single retro reflector, this scan duration requires a delay in optical path length of 6.0 - 7.5 mm respectively. The upper limit on the movement of the optical delay stage is 100 mm, so a factor of 10 improvement, down to single GHz resolution, should be possible with the current optical setup.

In order to use the maximum length of the delay stage the retro reflector must be aligned extremely well. A slight mismatch in either the entire retro reflector angle or either of the mirrors in the reflector results in a path length change that varies with the optical delay. This would introduce an effect similar to run out in optical masks, where the expected time of measurement at later optical delays would be biased significantly. To increase frequency resolution to the single GHz range, which should be possible, the retro-reflector should be realigned over a pathlength exceeding the 2 m currently used to align it.

One immediate benefit of improving the frequency resolution would be the ability to more accurately correlate known physical phenomena to features seen in various spectra. The absorption feature which has been attributed to the water tetramer, for example, could be studied in more detail and more readily verified against other measurements.

7.1.2 Rapid Scan Methods for THz-TDS

One of the distinct disadvantages of THz-TDS is the extremely slow data acquisition rate as a result of the need to physically translate a mechanical stage. Until a few years ago, the primary method for moving the delay line was to step a translation stage, wait anywhere from 200 ms to 2 seconds for the stage to settle, and then read the measurement from the lock-in amplifier (Kübler, 2002).

One method to remove this slow acquisition rate is to keep the optical delay stage in continuous motion at a constant velocity. Data can then be acquired at set intervals and the position of the stage at that time determined. These methods are typically referred to in the literature as rapid scan methods. Scan rates of 1 Hz for amplified laser systems are typical (Planken *et al.*, 2001) and

can reach into the kHz regime for non-amplified laser systems. The highest repetition rate THz measurements are due to a different procedure, known as ASOPS, where two femtosecond lasers with slightly different frequencies are used for detection and generation respectively. The difference in frequency essentially causes one pulse to be scanned in time across the other, with an effective repetition rate corresponding to the difference in frequencies (Bartels *et al.*, 2006).

While ASOPS requires new lasers, the method of rapid scan can be enabled with a software rewrite for the facilities in the PRL. This work has already been started, and completion of it, combined with significant testing could enable significant faster THz acquisition rates and improve the resilience of the system to long time scale noise sources.

7.1.3 Improved Achromatic Waveplates

The achromatic quarter waveplate that was developed in Chapter 5 showed the significant potential of using stacked layers of birefringent materials for THz optics. The transmission ratio of the current waveplate could be significantly improved through use of other materials, or more simply, by finding materials with a larger birefringence. The conditions which induced the birefringence in Teflon sheets can be recreated in the lab with other materials. As was shown in Chapter 4, a birefringence of Δn=0.10 can be readily induced in HDPE, which has comparable absorption to Teflon. This level of birefringence makes the fabrication of a waveplate that is 1/10 the thickness of the Teflon waveplate possible. Through further exploration of polymer materials, and also by considering natural oriented materials such as paper and wood, it should be possible to significantly improve upon the proof of concept shown in this work.

7.1.4 Circular Dichroism THz Spectroscopy

The initial motivation behind this work was not the study of birefringence or linear dichroism, rather it was the potential for the study of circular dichroism.

Beginning in 2003, a series of papers was published which showed the theoretical possibility of circular dichroism at THz frequencies in certain biological molecules that could be of significant interest Xu *et al.* (2003, 2004).

Circular dichroism is the analogue to linear dichroism, in other words the two circular polarization states of light end up having different absorption coefficients. Circular dichorism is also often referred to as optical activity. One source of circular dichroism is the chirality of molecules. A chiral molecule is a molecule which cannot be superimposed upon its mirror image. One obvious example of chirality is the human hand; no set of linear transformations exists which can manipulate a right hand to look idential to a left hand. Therefore the human hand exhibits chirality. The two different forms of chiral molecules, the left and right handed, are referred to as enantiomers, a mix of the two enantiomers with equal percentages of each is referred to as a racemic mixture.

The effect of a mixture of optically active molecules on the polarization state of incident light is different than the effect of a mixture of linearly birefringent or linearly dichroic molecules. If a large number of randomly oriented molecules with intrinsic linear birefringence or linear dichroism interact with light, no change in polarization state should occur as the random orientations result in an average of zero rotation. In a randomly oriented mixture of optically active (circularly dichroic) molecules, it can be shown that a rotation of the polarization state does occur. Thus circular dichroism is a potentially more versatile mechanism for identification of molecular species as an effect can be seen even in a randomly oriented mixture.

In biological systems, chirality is of interest because chiral monomers make up all biological macromolecules, proteins, and nucleic acids. In other words, the essential building blocks of life are all chiral, and they also exhibit what is known as the chirality consensus (Jaakkola *et al.*, 2008). Essentially, life on the planet earth exhibits a distinct preference for one handedness of molecule over another. In addition to being of interest to biologists, the chirality of a drug can significantly change its behaviour in the body (Henderson Jr *et al.*, 2005). The difference between racemic mixtures of drugs and individual enantiomers have also been detected due to different THz absorption spectra (Kishi *et al.*,

2005).

The human sense of smell happens to be highly chiral specific, with one of the common demonstrations of this being the aromatic molecule carvone. One enantiomer of carvone is found highly concentrated in spearmint leaves, and predictably, smells very minty. The other other enantiomer is found in caraway and its smell is best described as "herby".

The goal of detecting circular dichroism at THz frequencies is what drove the construction of a THz polarimeter with an extremely high extinction ratio. As liquid materials typically yield bland THz responses, and finding an appropriate solid material to work with is difficult, the natural choice for detecting circular dichroism was in the gas phase. This choice drove the construction of the gas-cell described in Chapter 6.

After an unsuccessful attempt to detect a THz response from the enantiomers of carvone, chiral alcohols were chosen as the next potential test case. In a chiral alcohol, a hydroxyl group is attached to the chiral carbon. As was shown in Chapter 6, alcohols are highly active at THz frequencies due to the hydroxyl group. It was hypothesized that the chirality of the molecule surrounding the absorption centre could impart a strong chiral response. Due to the expense of these alcohols, the only test molecules were (S)-butanol and (R)-butanol, the structure of which is shown in figure 7.1. Both of these molecules exhibit circular dichroism in the liquid phase at optical frequencies.

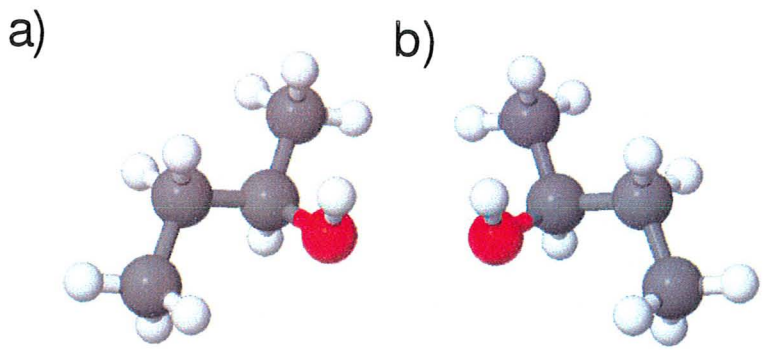

Figure 7.1: The two enantiomers of butanol: a) (R)-butanol b) (S)-butanol

No detectable chiral signature at THz frequencies was noted from either of

these molecules despite several trials and raising the temperature of the gas-cell to above 100°C. It is still possible that these molecules do exhibit circular dichroism at THz frequencies, and the apparatus was not sensitive enough to detect it. In any case, the question of circular dichroism at THz frequencies is still open, and the work in this thesis demonstrates one approach which may, in the future, yield a measurement of THz circular dichroism of biomolecules.

7.2 Conclusion

As has been demonstrated throughout this work, THz-TDS holds potential for experimental uses in many different fields. The ability to probe such a wide portion of the electromagnetic spectrum while also having access to study picosecond dynamics through pump-probe experiments is an extremely potent combination.

The focus of this work has been towards the goal of detecting circular dichroism at THz frequencies. While this goal was not achieved, many of the efforts made towards this goal have proved to be very fruitful. The alignment method described in Chapter 3 improved the extinction ratio of a THz-TDS setup using ZnTe by 2 orders of magnitude over any previous result. The birefringence and dichroism measurements of Chapter 4 set the stage for the development of the achromatic waveplate of Chapter 4. While a higher order achromatic waveplate has previously been developed out of quartz, this is the first known THz achromatic zero-order waveplate and it is made out of a commercially viable material. The gas phase spectroscopy measurements of Chapter 6 also provided interesting observations when a suspected collective vibrational mode of the water tetramer was noticed.

This work opens many new doors for experiments within the PRL, and with tenacity and a bit of serendipity, may provide the foundation for future observations of the sought after THz circular dichroism.

Appendix A

THz System Equipment Listing

A.1 Non-Linear Crystals

Table A.1: Thickness and orientation of ZnTe crystals determined using THz-TDS echo measurements.

Crystal	Size	Orientation	Thickness [mm]
Generator	1cm x 1cm	(110)	1.0mm
Detector	1cm x 1cm	(110)	1.3mm

Appendix B

Fabry-Perot Effect and Echoes in THz-TDS

One of the interesting aspects one comes across when conducting data analysis for THz-TDS is the interesting role that echoes off various interfaces play in the measured THz spectrum. While the total effect of these echoes can be succintly described mathematically by the Fabry-Perot effect, a simple derivation can also show why these echoes are so problematic for data anlaysis. The following derivation follows the notation of section 2.4 very closely and the key digram from that chapter describing the situation is reproduced below in figure B.1.

For the purposes of this example, it is assumed that $\tilde{n}$ is purely real, although a similar derivation be performed without this assumption. The measured output THz field, assuming a long enough time window is measured for a single echo, is $E_{out} = E_{s1} + E_{s2}$, where the individual pulses are related to the input electric field, E_i, by:

$$E_{s1} = t_{as}t_{sa}\exp(i\omega dn/c)E_i, \tag{B.1}$$

$$E_{s2} = t_{as}r_{sa}r_{as}t_{sa}\exp(i3\omega dn/c)E_i, \tag{B.2}$$

$$E_{ref} = \exp(i\omega dn/c)E_i. \tag{B.3}$$

Substituting E_{s1} and E_{s2} into E_{out}, and simplifiying a bit results in:

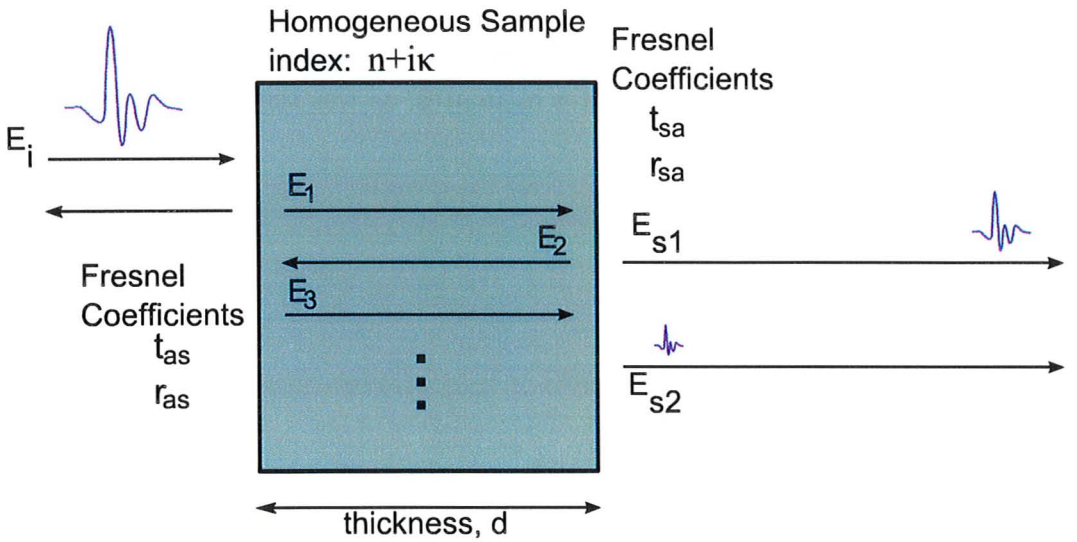

Figure B.1: Diagram of THz pulse propagation through a homogeneous sample of thickness d. The pulses are offset vertically each time they reflect from or transmit through an interface.

$$E_{out} = t_{as}t_{sa}\left(\exp\left(i\omega dn/c\right) + r_{sa}r_{as}\exp\left(i3\omega dn/c\right)\right)E_i. \tag{B.4}$$

Factoring out the common exponential term, then leaves:

$$E_{out} = t_{as}t_{sa}\exp\left(i2\omega dn/c\right)\left(\exp\left(-i\omega dn/c\right) + r_{sa}r_{as}\exp\left(i\omega dn/c\right)\right)E_i. \tag{B.5}$$

The term within the brackets then resembles a cosine term, rearranging and dividing by the measured THz signal without the echo gives the desired result:

$$\frac{E_{out}}{E_{s1}} = \left(1 - r_{sa}r_{as}\right) + 2r_{sa}r_{as}\cos\left(\omega dn/c\right)\exp\left(i\omega dn/c\right). \tag{B.6}$$

While further simplification could be performed, the critical result is the term: $r_{sa}r_{as}\cos\left(\omega dn/c\right)$, in E_{tot}. This term represents a sinusoidal variation with frequency in the amplitude of spectrum that is proportional to the magnitude of the spectrum. THz measurements which include an echo often confuse

a scientist who has only recently started with THz-TDS. The sinusoidal variation is only very significant in amplitude and plays a singificant role when attempting to obtain good parameter estimates, as was seen in Chapter 4.

Bibliography

Auston, D. H. (1993). *Ultrashort Light Pulses: Generation and Applications.* Springer-Verlag, Berlin, second edition.

Baker, C., Gregory, I., Tribe, W., Bradley, I., Evans, M., Withers, M., Taday, P., Wallace, V., Linfield, E., Davies, A., *et al.* (2003). Terahertz pulsed imaging with 1.06 μm laser excitation. *Applied Physics Letters*, **83**, 4113.

Bakker, H. J., Cho, G. C., Kurz, H., Wu, Q., and Zhang, X.-C. (1998). Distortion of terahertz pulses in electro-optic sampling. *J. Opt. Soc. Am. B*, **15**(6), 1795–1801.

Bartels, A., Thoma, A., Janke, C., Dekorsy, T., Dreyhaupt, A., Winnerl, S., and Helm, M. (2006). High-resolution THz spectrometer with kHz scan rates. *Opt. Express*, **14**, 430–437.

Beard, C., Turner, G., and Schmuttenmaer, C. (2002). Terahertz spectroscopy. *Journal of Physical Chemistry B*, **106**, 7146 – 7159.

Belov, S. P., Winnewisser, G., and Herbst, E. (1995). The high-resolution rotational-torsional spectrum of methanol from 0.55 to 1.2 thz. *Journal of Molecular Spectroscopy*, **174**(1), 253 – 269.

Bonvalet, A. and Joffre, M. (2005). *Femtosecond Laser Pulses*, chapter 10, pages 309–331. Springer New York, second edition.

Boyd, R. W. (1992). *Nonlinear Optics.* Academic, New York, NY.

Calingaert, G. and Davis., D. S. (1925). Pressure-temperature charts-extended ranges. *Industrial and Engineering Chemistry*, **17:12**, 1287 – 1288.

Castro-Camus, E., Lloyd-Hughes, J., Johnston, M. B., Fraser, M. D., Tan, H. H., and Jagadish, C. (2005). Polarization-sensitive terahertz detection by multicontact photoconductive receivers. *Applied Physics Letters*, **86**(25), 254102.

Chang, G., Divin, C., Liu, C., Williamson, S., Galvanauskas, A., and Norris, T. (2004). Power scalable compact THz system based on an ultrafast Yb-doped fiber amplifier. *Phys. Lett*, **85**, 3974.

Chen, Q., Tani, M., Jiang, Z., and Zhang, X.-C. (2001). Electro-optic transceivers for terahertz-wave applications. *J. Opt. Soc. Am. B*, **18**(6), 823–831.

Cheville, R. A. and Grischkowsky, D. (1998). Observation of pure rotational absorption spectra in the $\nu 2$ band of hot h2o in flames. *Opt. Lett.*, **23**(7), 531–533.

Clough, R. L. (2001). High-energy radiation and polymers: A review of commercial processes and emerging applications. *Nuclear Instruments and Methods in Physics Research Section B: Beam Interactions with Materials and Atoms*, **185**(1-4), 8 – 33.

Cruzan, J., Viant, M., Brown, M., and Saykally, R. (1997). Terahertz laser vibration-rotation tunneling spectroscopy of the water tetramer. *Journal of Physical Chemistry*, **101:48**, 9022 – 9031.

D. Teyssier, E. Dartois, D. D. J.-P. C. Y. L. F. B. M. P. (2004). A multi-path far-infrared and sub-millimetre gas cell for spectral tests of herschel/hifi.

David R. Lide, e. (2010). *CRC Handbook of Chemistry and Physics, 90th Edition (Internet Version 2010)*. CRC Press/Taylor and Francis, Boca Raton, FL.

Dorney, T., Baraniuk, R., and Mittleman, D. (2001). Material parameter estimation with terahertz time-domain spectroscopy. *Journal of the Optical Society of America A*, **18**(7), 1562–1571.

Ducasse, A., Rulliére, C., and Couillaud, B. (2005). *Femtosecond Laser Pulses*, chapter 3, pages 57–87. Springer New York, second edition.

Duvillaret, L., Garet, F., and Coutaz, J. (1999). Highly precise determination of optical constants and sample thickness in terahertz time-domain spectroscopy. *Applied Optics*, **38**(2).

Duvillaret, L., Garet, F., Roux, J.-F., and Coutaz, J.-L. (2001). Analytical modeling and optimization of terahertz time-domain spectroscopy experiments, using photoswitches as antennas. *Selected Topics in Quantum Electronics, IEEE Journal of*, **7**(4), 615 –623.

Fattinger, C. and Grischkowsky, D. (1989). Terahertz beams. *Applied Physics Letters*, **54**(6), 490–492.

Fowles, G. R. (1989). *Introduction to Modern Optics*. Dover Publications Ltd., New York, NY, second edition.

Gallot, G. and Grischkowsky, D. (1999). Electro-optic detection of terahertz radiation. *Journal of the Optical Society of America B*, **16**(8), 1204–1212.

Gallot, G., Zhang, J., McGowan, R. W., Jeon, T.-I., and Grischkowsky, D. (1999). Measurements of the thz absorption and dispersion of znte and their relevance to the electro-optic detection of thz radiation. *Applied Physics Letters*, **74**(23), 3450–3452.

Gasster, S. D., Townes, C. H., Goorvitch, D., and Valero, F. P. J. (1988). Foreign-gas collision broadening of the far-infrared spectrum of water vapor. *J. Opt. Soc. Am. B*, **5**(3), 593–601.

Gil, J. (2007). Polarimetric characterization of light and media. *Eur. Phys. J. App. Phys*, **40**(40), 1–47.

Griffiths, D. (1999). *Introduction to Electrodynamics*. Prentice Hall, Inc., Upper Saddle River, NJ, 3rd edition.

Grischkowsky, D., Keiding, S., van Exter, M., and Fattinger, C. (1990). Far-infrared time-domain spectroscopy with terahertz beams of dielectrics and semiconductors. *J. Opt. Soc. Am. B*, **7**(10), 2006–2015.

Harmon, S. A. and Cheville, R. A. (2004). Part-per-million gas detection from long-baseline thz spectroscopy. *Applied Physics Letters*, **85**(11), 2128–2130.

Hecht, E. (2001). *Optics*. Addision-Wesley, 4th edition.

Henderson Jr, W., Banerjee, E., and Chi, E. (2005). Differential effects of (S)-and (R)-enantiomers of albuterol in a mouse asthma model. *Journal of Allergy and Clinical Immunology*, **116**(2), 332–340.

Herraez, A. (2007). *How to use Jmol to study and present molecular structures, Vol.1*. Lulu Enterprises.

Hirlimann, C. (2005). *Femtosecond Laser Pulses*, chapter 2, pages 25–56. Springer New York, second edition.

Jaakkola, S., Sharma, V., and Annila, A. (2008). Cause of chirality consensus. *Current Chemical Biology*, **2**(2), 153–158.

Jones, R. (1941). A new calculus for the treatment of optical systems. *J. Opt. Soc. Am.*, (31), 488–493.

Jördens, C., Scheller, M., Wichmann, M., Mikulics, M., Wiesauer, K., and Koch, M. (2009). Terahertz birefringence for orientation analysis. *Appl. Opt.*, **48**(11), 2037–2044.

Kamal, S., Kim, D., Eom, C., and Dodge, J. (2006). Terahertz-frequency carrier dynamics and spectral weight redistribution in the nearly magnetic metal CaRuO_ {3}. *Physical Review B*, **74**(16), 165115.

Kanda, N., Konishi, K., and Kuwata-Gonokami, M. (2007). Terahertz wave polarization rotation with double layered metal grating of complimentary chiral patterns. *Opt. Express*, **15**(18), 11117–11125.

Kishi, T., Kanamori, T., Tsujikawa, K., Iwata, Y., Inoue, H., Ohtsuru, O., Hoshina, H., Otani, C., and Kawase, K. (2005). Differentiation of optical active form and racemic form of amphetamine-type stimulants by terahertz spectroscopy. In *Infrared and Millimeter Waves and 13th International Conference on Terahertz Electronics, 2005. IRMMW-THz 2005. The Joint 30th International Conference on*, volume 1.

Koch, M. (2007). Terahertz technology: A land to be discovered. *Optics and Photonics News*, **18:3**, 20 – 25.

Kübler, C. P. (2002). *Creation and Characterization of a Terahertz Time Domain Spectrometer*. Master's thesis, Simon Fraser Univ., Burnaby, BC.

Masson, J.-B. and Gallot, G. (2006). Terahertz achromatic quarter-wave plate. *Opt. Lett.*, **31**(2), 265–267.

McDaniel, E. B. and Hsu, J. W. P. (1996). Nanometer scale optical studies of twin domains and defects in lanthanum aluminate crystals. *Journal of Applied Physics*, **80**(2), 1085–1093.

Nahata, A., Weling, A. S., and Heinz, T. F. (1996). A wideband coherent terahertz spectroscopy system using optical rectification and electro-optic sampling. *Applied Physics Letters*, **69**(16), 2321–2323.

Naydenova, I., Nikolova, L., Todorov, T., Andruzzi, F., Hvilsted, S., and Ramanujam, P. (1997). Polarimetric investigation of materials with both linear and circular anisotropy. *Journal of Modern Optics*, **44**, 1643–1650.

Nuss, M. C. and Orenstein, J. (1998). *Terahertz Time Domain Spectroscopy*, volume 74 of *Topics in Applied Physics*, pages 6–43. Springer-Verlag, New York: NY.

Ohring, M. (2002). *The Materials Science of Thin Films*. Academic Press, San Diego, CA, second edition.

Peterlin, A. (1971). Molecular model of drawing polyethylene and polypropylene. *Journal of Materials Science*, **6:6**, 490–508.

Planken, P. C. M., Nienhuys, H.-K., Bakker, H. J., and Wenckebach, T. (2001). Measurement and calculation of the orientation dependence of terahertz pulse detection in znte. *J. Opt. Soc. Am. B*, **18**(3), 313–317.

Podobedov, V. B., Plusquellic, D. F., and Fraser, G. T. (2004). Thz laser study of self-pressure and temperature broadening and shifts of water vapor lines for pressures up to 1.4 kpa. *Journal of Quantitative Spectroscopy and Radiative Transfer*, **87**(3-4), 377 – 385.

Pupeza, I., Wilk, R., and Koch, M. (2007). Highly accurate optical material parameter determination with THz time-domain spectroscopy. *Opt. Express*, **15**(7), 4335–4350.

Reid, M. and Fedosejevs, R. (2006). Terahertz birefringence and attenuation properties of wood and paper. *Appl. Opt.*, **45**(12), 2766–2772.

Schmuttenmaer, C. A. (2004). Exploring dynamics in the far-infrared with terahertz spectroscopy. *Chemical Review*, **104:4**, 1759 – 1779.

Shimano, R., Nishimura, H., and Sato, T. (2005). Frequency tunable circular polarization control of terahertz radiation. *Japanese Journal of Applied Physics*, **44**(21), L676–L678.

Smith, P., Auston, D., and Nuss, M. (1988). Subpicosecond photoconducting dipole antennas. *Quantum Electronics, IEEE Journal of*, **24**(2), 255 –260.

Spectra-Physics Lasers Inc. (1997). *User's Manual: Millennia V - Diode-pumped, cw visible laser*. Spectra-Physics Lasers Inc., Santa Clara, CA.

Spectra-Physics Lasers Inc. (1999). *User's Manual: Evolution X - Diode-pumped, cw visible laser*. Spectra-Physics Lasers Inc., Santa Clara, CA.

Spectra-Physics Lasers Inc. (2000). *User's Manual: Tsunami Mode-locked Ti:Sapphire Laser*. Spectra-Physics Lasers Inc., Santa Clara, CA.

Spectra-Physics Lasers Inc. (2001). *User's Manual: Spitfire Multikiloherz Pulsed Ti:Sapphire Amplifier with Pulse Stretcher and Compressor*. Spectra-Physics Lasers Inc., Santa Clara, CA.

Swinehart, D. F. (1962). The beer-lambert law. *Journal of Chemical Education*, **39**(7), 337–335.

Tagaya, A., Iwata, S., Kawanami, E., Tsukahara, H., and Koike, Y. (2001). Anisotropic molecule dopant method for synthesizing a zero-birefringence polymer. *Japanese Journal of Applied Physics*, **40**(Part 1, No. 10), 6117–6123.

Tarantola, A. (2004). *Inverse Problem Theory. Methods for model parameter estimation*. SIAM, Philadelpha,PA.

Thomsone, G. W. (1946). The antoine equation for vapor-pressure data. *Chemical Reviews*, **38:1**, 1–39.

Tsai, T.-R., Chen, C.-Y., Pan, C.-L., Pan, R.-P., and Zhang, X.-C. (2003). Terahertz time-domain spectroscopy studies of the optical constants of the nematic liquid crystal 5cb. *Appl. Opt.*, **42**(13), 2372–2376.

Turcsnyi, B., Puknszky, B., and Tds, F. (1987). Composition dependence of tensile yield stress in filled polymers. *Journal of Materials Science Letters*, **7:2**, 160–162.

van Exter, M. and Grischkowsky, D. (1990). Characterization of an optoelectronic terahertz beam system. *Microwave Theory and Techniques, IEEE Transactions on*, **38**(11), 1684 –1691.

Van Exter, M., Fattinger, C., and Grischkowsky, D. (1989). Terahertz time-domain spectroscopy of water vapor. *Opt. Lett*, **14**(20), 1128–1130.

Wietzke, S., Jansen, C., Jung, T., Reuter, M., Baudrit, B., Bastian, M., Chatterjee, S., and Koch, M. (2009). Terahertz time-domain spectroscopy as a tool to monitor the glass transition in polymers. *Opt. Express*, **17**(21), 19006–19014.

Winnewisser, C., Jepsen, P., Schall, M., Schyja, V., and Helm, H. (1997). Electro-optic detection of THz radiation in LiTaO, LiNbO and ZnTe. *Applied Physics Letters*, **70**, 3069.

Withayachumnankul, W., Ferguson, B., Rainsford, T., Mickan, S., and Abbott, D. (2005). Material parameter extraction for terahertz time-domain spectroscopy using fixed-point iteration. In *Proc. SPIE*, volume 5840, pages 221–231.

Wu, Q. and Zhang, X. (1996). Ultrafast electro-optic field sensors. *Applied Physics Letters*, **68**, 1604.

Xu, J., Ramian, G. J., Galan, J. F., Savvidis, P. G., Scopatz, A. M., Birge, R. R., Allen, S. J., and Plaxco, K. W. (2003). Terahertz circular dichroism spectroscopy: A potential approach to the in situ detection of life's metabolic and genetic machinery. *Astrobiology*, **3**(3), 489–504.

Xu, J., Galan, J., Ramian, G., Savvidis, P., Scopatz, A., Birge, R. R., Allen, S. J., and Plaxco, K. (2004). Terahertz circular dichroism spectroscopy of biomolecules. volume 5268, pages 19–26. SPIE.

Xu, L.-H., Fisher, J., Lees, R., Shi, H., Hougen, J., Pearson, J., Drouin, B., Blake, G., and Braakman, R. (2008). Torsion-rotation global analysis of the first three torsional states ([nu]t=0, 1, 2) and terahertz database for methanol. *Journal of Molecular Spectroscopy*, **251**(1-2), 305 – 313.

Yariv, A. (1975). *Quantum ELectronics*. Wiley, New York, NY, 2nd edition.